

Numerical Investigation of Lattice Boltzmann-Immersed Boundary Method for Fluid-Structure Interaction Problems

Alessia Abbati

James Weir Fluids Laboratory
Department of Mechanical and Aerospace Engineering
University of Strathclyde, Glasgow

February 8, 2026

This thesis is the result of the author's original research. It has been composed by the author and has not been previously submitted for examination which has led to the award of a degree.

The copyright of this thesis belongs to the author under the terms of the United Kingdom Copyright Acts as qualified by University of Strathclyde Regulation 3.50. Due acknowledgement must always be made of the use of any material contained in, or derived from, this thesis.

Abstract

The prominence of fluid-solid interactions problems in industrial applications and natural processes determines a necessity for accurate and efficient simulation strategies. Because such problems are challenging to model with conventional methods and require extensive computational resources, the immersed boundary-lattice Boltzmann method (IB-LBM) provides a promising alternative.

Diffuse-interface IB-LBM approaches owe their popularity to the efficient implementation and the ability to suppress numerical oscillations in moving boundary problems. However, the diffuse interface alters the representation of the fluid-solid boundary and affects the accuracy of the flow field calculation. The present work investigates the diffusive effects of IBM for surface-confined particulate flows by comparing results with sharp-interface methods and explores mitigation strategies.

It is found that increasing confinement and close particle–particle interactions, particularly when interfaces overlap, accentuate interface diffusion and decrease simulation accuracy. To minimise diffusive effects, a boundary retraction scheme is implemented and its effectiveness is examined. It is shown that this strategy reduces interface diffusion errors and increases accuracy while limiting computational costs.

The fluid-solid coupling strategy is a critical aspect of IB-LBM formulations, as it influences numerical stability. It is demonstrated that weakly coupled schemes impose a limitation on the fluid-solid density ratio to achieve stable simulations. To address this problem, a strongly coupled formulation is implemented. The internal-mass effect is analysed, coupling strategies are compared, and the stability limits are identified.

The simulations of falling and rising particles capture the dynamics of light structures and provide insight into the influence of structural properties, geometrical con-

finement, and local flow field. The study of vortex-induced vibrations investigates the synchronisation regime, the oscillation amplitudes, and the influence of the critical mass ratio on the structural response. These results advance the understanding of physical and numerical mechanisms and demonstrate the potential of IB–LBM for studying particle-laden flows and flow-induced vibrations.

Contents

Abstract i

List of Figures vii

List of Tables xi

List of Symbols xiii

List of Abbreviations xviii

1 Introduction 1

1.1 Motivation and Significance 1

1.2 Challenges and Complexities 3

1.3 Scope and Objectives 5

1.4 Structure 7

2 Theoretical Framework and Physical Model 10

2.1 Mathematical Description 11

2.1.1 Characteristic Scales 11

2.1.2 Governing Equations 13

2.2 Continuum Theory 14

2.3 Kinetic Theory 15

2.3.1 Distribution Function 16

2.3.2 Boltzmann Equation 17

2.3.3 Boundary Conditions 19

2.4 Fluid-Structure Interaction . . . 22
2.4.1 Equations of Motion . . . 23
2.4.2 Momentum Balance Equations . . . 23
2.4.3 Contact Model . . . 25
2.5 Vortex-Induced Vibrations . . . 26
2.5.1 Vortex Shedding Mechanisms . . . 27
2.5.2 Structural Response Regimes . . . 27
2.6 Summary . . . 30

3 Numerical Methods **31**
3.1 Numerical Framework . . . 32
3.1.1 Overview of Numerical Methods . . . 32
3.1.2 Coupled Fluid–Structure Problems . . . 34
3.1.3 Interface Representation . . . 35
3.2 Lattice Boltzmann Method . . . 36
3.2.1 Lattice Boltzmann Equation . . . 36
3.2.2 Algorithm . . . 39
3.2.3 Collision Operators . . . 40
3.2.4 Boundary Conditions . . . 48
3.2.5 Forcing Schemes . . . 52
3.2.6 Moving Bounce-Back Method . . . 54
3.2.7 Interpolated Bounce-Back Method . . . 56
3.2.8 Partially Saturated Method . . . 57
3.3 Immersed Boundary Methods . . . 59
3.3.1 Mathematical Formulation . . . 60
3.3.2 Force Evaluation Strategies . . . 64
3.3.3 Multi-Direct-Forcing IBM . . . 66
3.3.4 Relaxed MDF-IBM . . . 69
3.3.5 Internal Mass Effect . . . 70
3.3.6 Numerical Stability . . . 73
3.3.7 Strongly Coupled IBM . . . 74

3.4 Discrete Element Method . . . 78
3.5 Algorithm . . . 80
3.6 Summary . . . 81

4 Validation and Verification of the LBM Solver 82
4.1 Introduction . . . 82
4.2 Problem Statement . . . 83
4.3 Numerical Simulations . . . 84
4.3.1 Simulation Parameters . . . 84
4.3.2 Methodology . . . 85
4.4 Effect of the Reynolds Number . . . 85
4.5 Effect of the Relaxation Time . . . 87
4.6 Effect of the Boundary Conditions . . . 89
4.7 Effect of the Collision Operator . . . 91
4.7.1 TRT Model . . . 91
4.7.2 MRT Model . . . 94
4.8 Conclusions . . . 94

5 Numerical Diffusion in Confined Flow Problems 96
5.1 Introduction . . . 96
5.2 Problem Statement . . . 97
5.3 Boundary Retraction Scheme . . . 99
5.4 Numerical Simulations . . . 100
5.4.1 Flow Past a Cylinder . . . 101
5.4.2 Sedimentation of a Single Particle Under Gravity . . . 107
5.4.3 Flow Around Two Impacting Particles . . . 110
5.4.4 Drafting-Kissing-Tumbling Process of Two Particles Settling . . . 114
5.5 Conclusions . . . 117

6 Numerical Stability in the Dynamics of Light Structures 119
6.1 Introduction . . . 119
6.2 Problem Statement . . . 120

6.3 Numerical Simulations . . . 121
6.3.1 Falling and Rising Particles . . . 122
6.3.2 Single Particle Released Off-Centre . . . 131
6.3.3 Multiple Particles Rising . . . 135
6.4 Conclusions . . . 138

7 Critical Mass Effects in Vortex-Induced Vibration **139**
7.1 Introduction . . . 139
7.2 Problem Statement . . . 140
7.3 Numerical Simulations . . . 141
7.3.1 Flow Past a Stationary Circular Cylinder . . . 141
7.3.2 Vortex-induced Vibrations of a Circular Cylinder . . . 145
7.4 Conclusions . . . 151

8 Conclusions and Future Work **152**
8.1 Concluding Remarks and Contributions . . . 152
8.2 Future work . . . 156

A Boundary Retraction Scheme Implementation **159**

Bibliography **160**

List of Figures

2.1 Schematic representation of a generic FSI domain. 23
2.2 Schematic representation of the contact between two particles and the particle interaction model. 26
2.3 Schematic representation of the main vortex shedding modes. 28
2.4 Schematic representation of the amplitude response as a function of the reduced velocity for flow past a freely vibrating cylinder. 29

3.1 Schematics of D2Q9 and D3Q19 velocity sets. 37
3.2 Schematics of bounce-back boundary conditions. 50
3.3 Schematics of the moving bounce-back method. 55
3.4 Schematics of the interpolated bounce-back method. 57
3.5 Classification of lattice nodes in the partially saturated method. 59
3.6 Schematics of the Eulerian grid and the Lagrangian nodes in the IBM. . 61
3.7 Interpolation stencils for different discrete delta functions. 63
3.8 Schematics of the interpolation and spreading procedures in the IBM. . 64

4.1 Schematics of the lid-driven cavity problem configuration. 85
4.2 Streamlines for the lid-driven cavity flow at increasing Reynolds numbers. 86
4.3 U-velocity profile for the lid-driven cavity flow at increasing Reynolds numbers. 87
4.4 V-velocity profile for the lid-driven cavity flow at increasing Reynolds numbers. 88
4.5 U-velocity profile for the lid-driven cavity flow at increasing relaxation times. 89

4.6 U-velocity profile for the lid-driven cavity flow at increasing relaxation times using halfway bounce-back. 90
4.7 U-velocity profile for the lid-driven cavity flow at increasing Reynolds numbers using different collision operators. 92
4.8 V-velocity profile for the lid-driven cavity flow at increasing Reynolds numbers using different collision operators. 93

5.1 Representation of the fluid-solid boundary. 100
5.2 Unconfined flow past a cylinder: contours of the dimensionless horizontal velocity at $Re = 40$. 102
5.3 Drag coefficient for unconfined flow past a cylinder. 103
5.4 Flow past a fixed cylinder: schematics of the computational domain and contours of the dimensionless horizontal velocity. 103
5.5 Confined flow past a cylinder: wall correction factor error for $\kappa = 0.4$. . 105
5.6 Confined flow past a cylinder: wall correction factor error for $\kappa = 0.2$. . 106
5.7 Confined flow past a cylinder: wall correction factor error for $\kappa = 0.1$. . 106
5.8 Sedimentation of a particle under gravity: schematics of the computational domain and contours of the vertical velocity. 108
5.9 Sedimentation of a particle under gravity: velocity error for $\kappa = 0.2$. . . 109
5.10 Sedimentation of a particle under gravity: velocity error for $\kappa = 0.1$. . . 109
5.11 Flow around two impacting cylinders: schematics of the computational domain and contours of the horizontal velocity. 111
5.12 Drag coefficient evolution for the flow around two impacting cylinders. . 112
5.13 Flow around two impacting cylinders: effect of the diffuse-interface on the drag coefficient. 113
5.14 Two particles settling in a channel under gravity: computational domain and contours of the vertical velocity. 114
5.15 Effect of interface diffusion on the motion of two particles settling in a channel under gravity. 116

6.1 Velocity error for sedimentation of a particle under gravity. 123

6.2 Particles falling and rising: contours of the vertical velocity and vorticity. 124
6.3 Terminal velocity for sedimentation of a particle under gravity for different density ratio values. 128
6.4 Particles falling and rising: contours of vertical velocity of the particle centre. 129
6.5 Particles falling and rising: time evolution of the vertical position and velocity of the particle centre. 130
6.6 Particles falling and rising: time evolution of the vertical velocity at different density ratios. 130
6.7 Settling trajectory of a particle released off-centre. 131
6.8 Velocity contours of a settling particle released off-centre at $Re = 1.88$. . 132
6.9 Velocity contours of a settling particle released off-centre at $Re = 4.4$. . 133
6.10 Settling trajectory of a particle released off-centre at different Reynolds numbers. 134
6.11 Settling trajectory of a particle released off-centre for $\kappa = 0.125$. 134
6.12 Rising trajectory of a particle released off-centre at different Reynolds numbers. 135
6.13 Multiple particles rising: schematics of the computational domain and vorticity contours. 136
6.14 Rising trajectory of nine particles: horizontal and vertical displacement of the particle centre. 137
6.15 Vorticity contours for the case of fifty particles rising. 137

7.1 Vorticity contours for flow past a stationary cylinder at $Re = 100$. 143
7.2 Time evolution of the drag and lift coefficients for flow past a stationary cylinder at $Re = 100$ and $Re = 150$. 144
7.3 Pressure distribution on the surface of the cylinder for $Re = 100$. 144
7.4 Schematics of the model representing the transverse motion of a vibrating cylinder in crossflow. 146
7.5 Variation of the nondimensional amplitude of cylinder oscillation with mass ratio for $Re = 100$. 148

7.6 Time evolution of the cylinder vertical displacement for mass ratio $m^* = 0.1$ and $m^* = 0.08$ at $Re = 100$. 148
7.7 Variation of the nondimensional amplitude of cylinder oscillation with mass ratio for $Re = 150$. 149
7.8 Time evolution of the cylinder vertical displacement for mass ratio $m^* = 0.1$ and $m^* = 0.08$ at $Re = 150$. 149
7.9 Variation of the nondimensional amplitude of cylinder oscillation with mass ratio for different Reynolds numbers. 150

List of Tables

3.1 Overview of numerical methods. 33
3.2 D2Q9 discrete velocity set. 38
3.3 D3Q19 discrete velocity set. 39

4.1 Relaxation times and grid sizes for lid-driven cavity flow simulations. . . 89
4.2 Numerical parameters for lid-driven cavity simulations with different collision models. 91

5.1 Geometry and fluid properties for unconfined flow past a cylinder. . . . 101
5.2 Geometry and fluid properties for confined flow past a cylinder. 105
5.3 Particle and fluid properties for sedimentation of a particle under gravity. 108
5.4 Particle and fluid properties for flow around two impacting particles. . . 111
5.5 Particle and fluid properties for sedimentation of two particles. 114

6.1 Particle and fluid properties for falling and rising particles in the creeping flow regime. 123
6.2 Velocity error and stability at different density ratio values for $D = 6\Delta x$. 125
6.3 Velocity error and stability at different density ratio values for $D = 12\Delta x$. 126
6.4 Velocity error and stability at different density ratio values for $D = 18\Delta x$. 126
6.5 Particle and fluid properties for falling and rising particles at moderate Reynolds number. 128
6.6 Maximum Reynolds number value for the case of falling and rising particles at moderate Reynolds number. 129
6.7 Particle and fluid properties for a single particle released off-centre. . . . 131

6.8 Particle and fluid properties for multiple falling and rising particles. . . . 136

7.1 Geometry and fluid properties for flow past a cylinder. 143

7.2 Flow around a stationary cylinder: comparison of the drag coefficient, lift coefficient, and Strouhal number for $Re = 100$. 145

List of Symbols

A	Amplitude
c	Damping coefficient
$\mathbf{c}_i$	Discrete velocity
c_s	Speed of sound
C_d	Drag coefficient
C_l	Lift coefficient
C_p	Pressure coefficient
D	Diameter
f	Particle distribution function
f_i	Discrete-velocity distribution function
f_n	Natural frequency
f_v	Vortex shedding frequency
$\mathbf{F}$	Body force density
$\mathbf{F}_\mathrm{c}$	Contact force
$\mathbf{F}_\mathrm{d}$	Drag force
$\mathbf{F}_\mathrm{g}$	Gravitational force
$\mathbf{F}_\mathrm{ib}$	Immersed boundary force density

g	Gravitational acceleration
H	Height
I	Moment of inertia
k	Spring coefficient
L	Length
m	Mass
m^*	Mass ratio
m_c^*	Critical mass ratio
$\mathbf{n}$	Normal vector
p	Pressure
r	Position vector
r_d	Retraction distance
R	Gas constant
t	Time
$\mathbf{t}$	Tangential vector
T	Temperature
$\mathbf{T}$	Torque
$\mathbf{u}$	Macroscopic mean velocity
U^*	Reduced velocity
$\mathbf{v}$	Relative velocity
V_t	Terminal velocity
w_i	Weighting coefficient

W	Width
$\mathbf{x}$	Position
$\mathbf{X}$	Particle centre coordinates

Greek Letters

Γ	Relaxation parameter
δ	Dirac delta distribution
Δs	Lagrangian points spacing
Δt	Time step
Δx	Lattice spacing
ϵ	Solid fraction
ε_{c}	Critical distance
η	Friction coefficient
θ	Angular displacement
Θ	Angular velocity
κ	Confinement ratio
λ	Wall correction factor
μ	Dynamic shear viscosity
μ_B	Dynamic bulk viscosity
ν	Kinematic shear viscosity
ν_B	Kinematic bulk viscosity
$\boldsymbol{\xi}$	Particle velocity

ρ	Density
$\boldsymbol{\sigma}$	Viscous stress tensor
τ	Relaxation time
$\boldsymbol{\tau}$	Hydrodynamic stress tensor
Φ	Discrete delta function
ω	Relaxation rate
Ω_i	Collision operator

Subscripts

b	Boundary
f	Fluid
h	Hydrodynamic
i	Internal
ℓ	Lagrangian
n	Normal
p	Particle
s	Solid
t	Tangential
w	Wall

Superscripts

eq	Equilibrium

$\star$	After collision

Dimensionless numbers

Kn	Knudsen number
Ma	Mach number
Re	Reynolds number
St	Strouhal number

List of abbreviations

BBGKY	Bogoliubov, Born, Green, Kirkwood and Yvon equations
BGK	Bhatnakar-Gross-Krook
CFD	Computational fluid dynamics
CLBM	Cascaded lattice Boltzmann method
CPU	Central processing unit
DEM	Discrete element method
DKT	Drafting-kissing-tumbling
DPD	Dissipative particle dynamics
DSMC	Direct simulation Monte Carlo
DUGKS	Discrete unified gas kinetic scheme
DVM	Discrete velocity method
FDM	Finite difference method
FEM	Finite element method
FSI	Fluid-structure interaction
FVM	Finite volume method
GPU	Graphics processing unit

IB-LBM	Immersed boundary-lattice Boltzmann method
IBB	Interpolated bounce-back
IBM	Immersed boundary method
LBE	Lattice Boltzmann equation
LBM	Lattice Boltzmann method
LGCA	Lattice gas cellular automata
MD	Molecular dynamics
MDF	Multi-direct-forcing
MDF-IBM	Multi-direct-forcing immersed boundary method
MES	Momentum exchange algorithm
MRT	Multiple-relaxation-time
NSE	Navier-Stokes equations
PSM	Partially saturated method
SEM	Spectral element method
TRT	Two-relaxation-time
UGKS	Unified gas kinetic scheme
VIV	Vortex-induced vibrations

Chapter 1

Introduction

This introductory chapter establishes the foundations of the research conducted in the present work. The fundamental concepts and significance of fluid-structure interaction (FSI) problems are discussed in Section 1.1 by exploring their occurrence in different engineering disciplines along with relevant industrial applications and natural phenomena. Attention is drawn to the importance of a correct understanding of FSI behaviour. In Section 1.2, the complexity of FSI problems is examined, and the different approaches available to study such systems are considered. This review establishes the advantages offered by numerical simulations and provides an argument for the method chosen in the present work. The central themes and the main research objectives are outlined in Section 1.3 to determine the contributions of this work.

1.1 Motivation and Significance

FSI is an interdisciplinary field of study that investigates the dynamic interaction between fluids and solid structures. In FSI problems, the motion of the fluid influences the response of the structure, and at the same time, the behaviour of the solid directly affects the fluid flow. FSI problems are prominent in nature and technology, encompassing a broad range of disciplines. The study of FSI plays a crucial role in various engineering and scientific applications [1]. The most prominent FSI problems that have been explored in the literature include particulate flows, flow-induced vibrations, biomechanics,

microfluidics, aeroelasticity and acoustics [2–9]. This work focuses on particulate flows and flow-induced vibrations due to their relevance.

Particulate flows are systems consisting of solid particles interacting within a fluid medium. These problems involve a wide range of particle sizes and shapes which can be suspended or dispersed in a liquid or gas. The study of particulate flows investigates different mechanisms of particle-fluid and particle-particle interactions, including collision, sedimentation, aggregation, dispersion and pattern formation [10]. Particulate flows characterise various environmental phenomena such as the dispersion of pollutants in the atmosphere, sedimentation processes, mechanisms of erosion and deposition, rain formation and pyroclastic flows [11–18]. They are prominent in chemical and pharmaceutical technology including aerosol deposition, drug delivery and powder processing [19–22]. Other industrial applications involve fluidised beds for chemical reactors and energy production, particle-laden combustion, slurry transportation and separator technology [23–26, 40].

Flow-induced vibrations are complex mechanisms of FSI associated with the movement of a structure due to the force exerted by a surrounding or internal fluid. A correct understanding of such phenomena is of critical importance because oscillations and vibrations occurring in structures can severely affect their integrity and stability [4,27,28]. This problem is especially prevalent in civil engineering applications susceptible to wind loads, such as bridges, dams, buildings and tall structures [1, 29, 30]. Flow-induced vibrations are also of significant importance in marine and ocean engineering systems affected by waves and currents such as offshore structures, wind farms, pipelines, risers and mooring systems [31–33]. Additional applications include turbomachines, heat exchangers and piping systems [34–36].

A thorough understanding of the complex interplay between fluids and solids contributes to analysing and explaining complex phenomena occurring in nature. Additionally, the study of FSI problems provides critical insights into a multitude of industrial applications [10, 27]. This knowledge is essential for the design of various processes and products. It allows to optimise the design in order to improve the efficiency and assess the capability of the design modifications [37]. A correct understanding of the

interaction between fluid and solids is important to evaluate the performance under service conditions, estimate the response under different operating conditions and avoid undesirable outcomes [38]. Therefore, accurate prediction of FSI behaviour enables design improvements and innovative solutions that increase efficiency, ensure operational reliability and enhance safety.

1.2 Challenges and Complexities

The mutual influence between fluid and solid in FSI determines complex interdisciplinary problems whose solution requires elaborate approaches. For cases involving simple geometries and boundary conditions, analytical models can be derived from the constitutive equations describing fluid and solid mechanics. However, these formulations are limited to simplified cases because their solution is not achievable for more difficult problems [39]. Experimental studies can provide insights into more complex FSI systems, but they are generally associated with higher costs and limited in scope and scale [40]. Numerical simulations have become an increasingly popular alternative to understand the behaviour of FSI systems owing to the continuous growth of computational performance. The employment of numerical techniques allows to reduce costs compared to experimental approaches while expanding the complexity of problems that limit analytical formulations. Therefore, developing accurate and reliable numerical tools is of critical importance to investigate the underlying mechanisms of FSI problems [10].

Despite the progress achieved in recent years, modelling FSI problems by means of numerical methods remains a challenging endeavour [41]. Fluid and solid systems cannot be analysed separately due to the significance of their interactions [42]. Therefore, the numerical formulation of FSI problems is governed by coupled equations connecting the fluid and solid domain [1]. To correctly predict FSI behaviour, coupling strategies require advanced numerical tools that are capable of establishing information exchange at the fluid-solid interface while ensuring consistency. The non-linear nature of the systems and the representation of the fluid-solid boundary add further complexity to the formulation. Additionally, particulate-flow configurations involve particle–particle

interactions and collisions, which require dedicated modelling strategies. Because of these challenges, the numerical solution of FSI problems is usually associated with significant computational costs [43]. Therefore, the development of scalable and efficient algorithms is of crucial importance.

Conventional macroscale computational fluid dynamics (CFD) methods often fail to accurately represent the underlying mechanisms of these interactions, resulting in substantial drawbacks [41].

In recent years, several numerical schemes have emerged as efficient alternatives to Navier-Stokes-based solvers. One of the most promising approaches is the lattice Boltzmann method (LBM), owing to the simplicity of its formulation and its computational efficiency [2]. Furthermore, the kinetic nature of the LBM allows to capture the physics of microscale and mesoscale phenomena while correctly representing macroscopic behaviour [44]. LBM algorithms are characterised by local operations which facilitate the implementation on parallel processors and ensure high-performance computing [2, 45]. Additionally, LBM schemes are particularly suitable for implementation on graphics processing units (GPU). In comparison to central processing unit (CPU) architectures, GPU significantly improve the execution of parallel computations and increase the overall efficiency of the algorithm [46].

One of the crucial challenges faced by LBM schemes in FSI problems is modelling complex arbitrary-shaped boundaries and moving solid objects. Conventional methods generally require grid generation at each timestep to handle solid body motion and local refinements to match irregular geometries, resulting in computationally demanding algorithms. In the LBM framework, the immersed boundary method (IBM) emerges as a promising solution to model fluid-solid boundary conditions [41]. IBM schemes decouple fluid and solid computational systems, eliminating the need to update the grid for moving geometries and accommodating complex interface shapes [47]. This solution enables simulations of demanding FSI problems while reducing the computational cost associated with complex and moving geometries [1].

The challenges inherent to modelling interactions between fluids and solids highlight the need for advanced computational methods. In this context, the immersed

boundary-lattice Boltzmann method (IB-LBM) provides a versatile framework to simulate complex FSI problems with enhanced accuracy and computational efficiency. Particle–particle interaction and collision dynamics are resolved using the discrete element method (DEM), as its formulation allows particle motion and contact force models to be consistently integrated within the IB-LBM framework.

Although significant efforts have been made to advance the knowledge and implementation of IB-LBM approaches for FSI problems, several aspects still require further investigation. The behaviour of IB-LBM schemes depends strongly on numerical implementation choices such as collision operator, forcing scheme and fluid–structure coupling strategy. As a consequence, important uncertainties remain regarding the accuracy of fluid-solid boundary representation, the stability of the coupling procedure, and the extent to which implementation details influence the calculation of macroscopic quantities of interest. A clear understanding of these limitations is essential for the development of reliable and efficient computational tools and therefore motivates a closer and more systematic investigation.

1.3 Scope and Objectives

This work builds on the current knowledge surrounding IB-LBM and aims to improve its fundamental understanding. In particular, the motivation for the research presented in the following chapters stems from the insufficient understanding of specific implementation-related issues that hinder the capabilities of IB-LBM schemes. To achieve this aim, the research is structured around the following objectives.

The initial objective of this work is to address the main challenges of LBM algorithms, focusing on the verification and validation of the current implementation. The numerical accuracy and stability of LBM schemes are closely connected to the choice of relaxation parameter and collision model. The most straightforward approaches to model the complex LBM collision operator exhibit viscosity-dependent characteristics due to the interconnection between relaxation time and fluid viscosity. This behaviour has important implications for the reliability of the numerical method, as the solution

differs based on the choice of viscosity. Additionally, when boundary conditions are implemented, the location of the boundary is viscosity-dependent, and an unphysical velocity slip occurs. This analysis aims to evaluate the limitations of different LBM collision models and establish the necessity for advanced collision operators and forcing schemes. Accordingly, a systematic evaluation is conducted to assess the numerical accuracy and stability of different collision models. The investigation addresses viscosity-dependent behaviour, the occurrence of a velocity slip at the boundary, and the role of boundary-condition implementation strategies in shaping these effects. Further consideration is given to the computational efficiency and the effort associated with selecting appropriate relaxation parameters.

The second objective of this work is to investigate increasingly complex FSI problems in order to assess and improve the accuracy, stability, and efficiency of the current IB-LBM approach. In particular, the implementation of IB-LBM considered in this work exhibits a crucial drawback related to the representation of the fluid-solid interface. This work aims to investigate the numerical accuracy of diffuse-interface IBM compared to sharp-interface methods for increasingly complex cases. Problems involving significant geometrical confinement, particle-particle interactions and collision require further investigation due to the challenging representation of overlapping interfaces and are therefore examined in detail in this work. In addition to this assessment, another important objective of the research is to devise an error mitigation strategy to improve the accuracy of the interface representation and the related velocity calculation. The proposed strategy is developed and implemented within the IB-LBM framework, and its effectiveness is assessed through a series of benchmark problems, with particular emphasis on its ability to reduce interface diffusion and improve the calculation of hydrodynamic quantities.

A further research objective is to improve the understanding of the different strategies for coupling fluid and structure equations. An important challenge faced by IB-LBM algorithms is related to the coupling of governing equations because it imposes a limitation on numerical stability. To address this issue, the capabilities of strongly coupled and weakly coupled IBM schemes are systematically compared. The aim is to

investigate the parameters that affect numerical stability and establish the density ratio limitation for stable simulations. Particular attention is given to problems involving light structures, in order to determine the conditions under which the IB-LBM approach remains stable and accurate in these challenging cases.

The final objective of this work is to evaluate the capability of the improved IB-LBM framework in simulating complex flow–structure interaction phenomena, with particular emphasis on vortex-induced vibrations (VIV). Such configurations represent a challenging class of problems, as they couple unsteady wake dynamics with structural motion and therefore place stringent requirements on numerical stability. In this context, the IB-LBM approach is applied to different configurations in order to analyse its stability and accuracy. The results are analysed to evaluate the ability of the IB-LBM code to reproduce the characteristic behaviour associated with VIV over a range of regimes.

In conclusion, this research aims to contribute to the advancement of IBM knowledge within the LBM framework and establish its potential pertaining to complex fluid-solid interaction problems. Building on the obtained results, targeted improvements are proposed, implemented and systematically evaluated to enhance the accuracy and stability of the IB-LBM approach.

1.4 Structure

This thesis consists of eight chapters. The topics introduced in the remaining chapters are organised as follows.

Chapter 2 establishes the theoretical framework and physical model used throughout the thesis. The mathematical description of fluid dynamics at different length scales is introduced, with focus on continuum theory and conservation laws. Important concepts of kinetic theory are established and the Boltzmann equation is derived. The formulation of fluid–structure interaction is presented, including the equations of motion for rigid bodies and the contact model for solid interactions. Finally, vortex-induced vibrations are introduced together with the associated flow mechanisms and structural response regimes.

Chapter 3 introduces the numerical methods used in this work to model FSI prob-

lems and discusses their advantages over traditional approaches. The numerical implementation of LBM is extensively covered and discussed, highlighting the overall advantages and challenges. Special attention is dedicated to the different collision operators, focusing on the central moment method and the corresponding forcing scheme. An overview of the most common boundary conditions in the LBM framework is also provided, including techniques for treating moving geometries and complex fluid–solid interfaces. An in-depth review of the fundamental concepts of IBM is provided, focusing on the IB-LBM implementation. The multi-direct-forcing method (MDF) is introduced as a prominent approach to enhance the accuracy and efficiency of the general IBM scheme. The procedure to enforce the no-slip boundary condition is discussed, including the relaxation scheme used to accelerate the convergence rate. Common limitations of IBM are explored along with different mitigation strategies. The extension to a strongly coupled formulation is also presented to address stability issues related to the fluid–solid coupling. The description of the numerical method considered in this work is completed by a brief introduction to the DEM and the combined DEM-IB-CLMB approach.

Chapter 4 is dedicated to the validation and analysis of different numerical schemes in the LBM framework. The lid-driven cavity flow is considered an effective test case owing to the relatively simple geometry and boundary conditions. Because the flow exhibits progressively complex features as the Reynolds number increases, the ability of LBM to capture the correct flow behaviour in different regimes is examined. The effect of the relaxation time is thoroughly investigated due to its significant contribution to the overall numerical accuracy and stability. Fullway and halfway bounce-back schemes are compared as boundary conditions strategies along with a discussion on important limitations. Finally, three common collision operators are investigated and reviewed.

Chapter 5 addresses the diffuse-interface effects associated with the present IBM implementation. Four benchmark problems are considered: flow past a cylinder, settling of a particle under gravity, flow around two impacting particles, and the drafting-kissing-tumbling process of two particles settling in a channel. These test cases highlight the significant impact of the diffuse interface on problems involving confined geometries and

interactions between solid particles. To provide a comprehensive analysis, the results are compared to available analytical formulations, experimental data and the results of sharp-interface methods. A boundary retraction scheme is considered as an approach to limit the diffusive boundary effect and improve accuracy. The optimal implementation strategies for different problems are tested and examined.

Chapter 6 investigates the numerical stability of IBM schemes for problems involving solid particles whose density is comparable to or smaller than the density of the surrounding fluid. The focus is placed on assessing the performance of the strongly coupled IB–LBM in this configuration and on clarifying the role of the internal-mass effect. Test cases involving particles falling and rising at different Reynolds numbers are considered to compare the performance and stability properties of weakly coupled and strongly coupled schemes, and investigate the dynamics of light particles.

Chapter 7 considers vortex-induced vibration problems to evaluate the ability of the strongly coupled IB-LBM to accurately capture complex phenomena associated with light structures. Particular attention is given to the critical-mass effect and the emergence of distinct response branches, as well as to the stability of the method when approaching very low density ratios. The analysis includes simulations of flow past a stationary cylinder and of a freely oscillating cylinder over a range of Reynolds numbers and mass ratios.

Finally, Chapter 8 consolidates the contribution of the research conducted in this thesis and outlines insights into future scopes and challenges.

Chapter 2

Theoretical Framework and Physical Model

This chapter aims to establish a theoretical foundation for the following work by introducing the fundamental concepts and models that describe the relevant physical phenomena. Starting from the mathematical description of fluid dynamics at different length and time scales, the main governing equation and characteristic parameters are introduced in Section 2.1. In Section 2.2, the macroscopic description of fluids is introduced within the framework of continuum theory, showing how conservation laws and constitutive relations define the governing equations. Focusing on the mesoscopic scale, Section 2.3 discusses the most important concepts of kinetic theory and presents the Boltzmann equation alongside its assumptions. After establishing the fluid description, the physical model is completed by introducing the fluid–structure interaction formulation in Section 2.4. The mathematical description of coupled fluid–solid systems is outlined, including the equations of motion for rigid bodies, the balances of force and torque, and the contact model used to describe collisions and interactions between solids. Finally, Section 2.5 focuses on vortex-induced vibrations as characteristic fluid–structure interaction phenomena, discussing the mechanisms of vortex shedding and the resulting structural response regimes.

2.1 Mathematical Description

The mathematical description of fluid dynamics is based on the fundamental assumption that the observed *macroscopic* phenomena arise from the dynamics of *microscopic* particles [7]. The microscopic description of fluids focuses on individual atoms and molecular systems that are governed by Newton's equations of motion. At the macroscopic scale, the continuum assumption states that the observed fluid properties are based on average measures of the atomistic behaviour. Macroscopic systems are governed by the Navier-Stokes equations (NSE) that predict macroscopic properties such as density, velocity and temperature. The *mesoscopic* description of fluids operates between the microscopic and macroscopic scales and it is based on the kinetic theory. At the mesoscopic scale, the Boltzmann equation tracks the distribution of particles in a fluid rather than individual molecules [48].

2.1.1 Characteristic Scales

Each description of fluid dynamics is connected to a representative length scale. Microscopic systems are described by the length scale ℓ_{a} associated with the size of a fluid atom or molecule. The mesoscopic scale is characterised by the mean free path ℓ_{mfp}, defined as the average distance travelled by a particle between two successive collision events. In macroscopic systems, the characteristic length ℓ is defined by the scale for gradients of macroscopic properties. The hierarchy of length scale from small to large is defined as $\ell_{\mathrm{a}} \ll \ell_{\mathrm{mfp}} \ll \ell$.

The mathematical description of fluid systems is also defined by a hierarchy of time scales based on the different length scales. At the atomistic scale, particles are constantly moving with an average thermal velocity v_T and they participate in collisions that move them out of the equilibrium state. Thus, microscopic systems are characterised by collision events whose duration defines the collision time $t_{\mathrm{c}} \sim \ell_{\mathrm{a}}/v_{\mathrm{T}}$. At the mesoscopic scale, the system relaxes to local equilibrium through collision events and the representative time scale is defined by the mean flight time between two successive collisions $t_{\mathrm{mfp}} = \ell_{\mathrm{mfp}}/v_{\mathrm{T}}$. The macroscopic description operates at time scales suffi-

ciently large to allow averaging over microscopic time scale disturbances. Furthermore, a significant microscopic change that relaxes over a macroscopic time scale can be detected and represented by macroscopic average properties. In a macroscopic system, the hydrodynamic time scale can be defined for both the inertial $t_{\text{adv}} \sim \ell/u$ and the viscous $t_{\text{diff}} \sim \ell^2/\nu$ regime. The ratio between the diffusive and advective time scales defines the *Reynolds number*

$$Re = \frac{t_{\text{diff}}}{t_{\text{adv}}} = \frac{u\,\ell}{\nu}\,, \tag{2.1}$$

where u is the macroscopic fluid velocity and ν is the *kinematic viscosity*. The acoustic time scale $t_{\text{sound}} \sim \ell/c_{\text{s}}$ can be defined as the characteristic time associated with compression waves propagating through a fluid medium. The ratio between the acoustic and advective time scales defines the *Mach number*

$$Ma = \frac{t_{\text{sound}}}{t_{\text{adv}}} = \frac{u}{c_{\text{s}}}\,, \tag{2.2}$$

where c_{s} is the *speed of sound* in the fluid. When the fluid velocity u approaches the speed of sound c_{s}, *compressibility* effects become relevant. It is usually assumed that a steady flow with $Ma \leq 0.3$ is *incompressible* [42, 49].

Another important nondimensional parameter is the *Knudsen number*, which is defined as the ratio of the mean free path ℓ_{mfp} over a representative length scale ℓ

$$Kn = \frac{\ell_{\text{mfp}}}{\ell}\,. \tag{2.3}$$

This dimensionless number quantifies the rarefaction effects and it is particularly important for *rarefied gas dynamics* and *microfluidics*. The Knudsen number can be considered as the dimensionless parameter that characterizes the relative number of intermolecular and molecule surface collision [50].

When the representative length scale of the fluid system ℓ is significantly larger than the mean free path ℓ_{mfp}, the Knudsen number is small, and the fluid can be considered as a continuum. When the *continuum hypothesis* is valid, the fluid can be represented by fluid elements that are small with respect to the system size, but large in comparison

to the size of individual molecules. The flow regime for $Kn \leq 10^{-2}$ is classified as *continuum regime* and the Navier–Stokes equations govern the flow [7, 51–53]. The conventional no-slip boundary condition for the fluid velocity at the wall is valid, and the main mechanism of transport is bulk diffusion [54].

The Knudsen number is correlated to the Mach and Reynolds numbers according to

$$Kn = \alpha \frac{Ma}{Re}, \tag{2.4}$$

where α is a numerical constant. These nondimensional parameters play an important role in defining the *law of similarity*. This fundamental principle states that fluid flows which share the same dimensionless numbers provide the same physics when they are scaled by the characteristic scales of the problem [48].

2.1.2 Governing Equations

The most fundamental description of a fluid system is given by the Hamiltonian dynamics for $N \sim \mathcal{O}(10^{23})$ identical point particles [39]. An alternative to this complex deterministic description can be derived by shifting the focus to the dynamics of a group of molecules. This requires a statistical description based on probabilistic concepts, such as the *probability density function*. The evolution of the probability density function for an N particle system is described using the Liouville equation [39, 55]. This probabilistic approach is still a complex description based on a function of $\sim \mathcal{O}(10^{23})$ variables. The Liouville equation can be simplified by limiting the description to the interactions between $n\,(< N)$ particles and adding a correction term to account for the remaining particles outside of this group. This results in a set of $N \sim \mathcal{O}(10^{23})$ coupled equations known as the BBGKY (Bogoliubov, Born, Green, Kirkwood and Yvon) hierarchy of equations [56]. The main advantage of this formulation compared to the Liouville equation is that it can be approximated by truncating the hierarchy. Further simplification is achieved by introducing the *molecular chaos* assumption, which states that the velocities of the molecules participating in a collision are uncorrelated. This argument leads to the formulation of the Boltzmann equation, which is described in

detail in Section 2.3.

The Boltzmann equation can be approximated using the *Chapman-Enskog analysis* [57]. The analysis procedure expands the distribution function using an appropriate expression and then isolates the important terms while neglecting the others [39]. The zeroth–order solution of the Chapman-Enskog expansion defines the equilibrium solution, which corresponds to the Euler equations. The first-order solution yields the compressible Navier–Stokes equations, while the second-order and third-order solutions lead respectively to the Burnett and super-Burnett equations [39].

2.2 Continuum Theory

At the macroscopic level, fluid behaviour is governed by the fundamental conservation laws of mass, momentum, and energy, which form the basis of the continuum description of fluid mechanics. Conservation laws are derived by applying a balance principle to a control volume, where the rate of change of a property inside the volume is determined by the flux across its boundary and any sources within [42, 58].

The conservation of mass is expressed by the *continuity equation* in the following form

$$\frac{\partial \rho}{\partial t} + \nabla \cdot (\rho \mathbf{u}) = 0, \tag{2.5}$$

where ρ denotes the mass density and $\mathbf{u}$ the fluid velocity.

The conservation of momentum can be written in the general form of the Cauchy momentum equation

$$\frac{\partial (\rho\, \mathbf{u})}{\partial t} + \nabla \cdot (\rho\, \mathbf{u}\, \mathbf{u}) = \nabla \cdot \boldsymbol{\tau} + \mathbf{F}, \tag{2.6}$$

where $\boldsymbol{\tau}$ is the stress tensor and $\mathbf{F}$ represents body forces acting on the fluid. The stress tensor accounts for both the pressure p and viscous stress $\boldsymbol{\sigma}$ contributions [42, 59]

$$\boldsymbol{\tau} = -p\, \mathbf{I} + \boldsymbol{\sigma}\,, \tag{2.7}$$

where $\mathbf{I}$ is the identity tensor. In the simplest case of an inviscid fluid, momentum transfer occurs only through reversible mechanisms, and the stress tensor reduces to

the isotropic pressure contribution $\boldsymbol{\tau} = -p\,\mathbf{I}$. The corresponding momentum balance takes the form of the *Euler equation*

$$\frac{\partial\,(\rho\,\mathbf{u})}{\partial t} + \nabla\cdot(\rho\,\mathbf{u}\,\mathbf{u}) = -\nabla p + \mathbf{F}\,. \tag{2.8}$$

In real fluids, momentum is also transferred irreversibly due to viscosity, arising from internal friction between adjacent parts of the fluid moving at different speeds. At the continuum scale, this effect is represented through the following constitutive relation for the viscous stress tensor [42, 49]

$$\boldsymbol{\sigma} = \mu\big[\nabla\mathbf{u} + (\nabla\mathbf{u})^T - \tfrac{2}{3}(\nabla\cdot\mathbf{u})\,\mathbf{I}\big] + \mu_B\,(\nabla\cdot\mathbf{u})\,\mathbf{I}\,, \tag{2.9}$$

where μ is the dynamic shear viscosity and μ_B the dynamic bulk viscosity. Substituting this constitutive relation into the momentum equation recovers the *Navier–Stokes equation* in the following form

$$\frac{\partial\,(\rho\,\mathbf{u})}{\partial t} + \nabla\cdot(\rho\,\mathbf{u}\,\mathbf{u}) = -\nabla p + \nabla\cdot\boldsymbol{\sigma} + \mathbf{F}\,. \tag{2.10}$$

To complete the mathematical description, appropriate initial and boundary conditions must be specified. At solid walls, the no-slip condition is typically imposed, requiring that the fluid velocity matches the velocity of the boundary [59].

2.3 Kinetic Theory

Kinetic theory is a mesoscopic scale fluid description that tracks the distribution of particles in a gas. The representative length scale is the mean free path ℓ_{mfp} and the characteristic time scales is the mean collision time t_{mfp}.

Kinetic theory is most commonly applied to the simplest case of *dilute* gases [39]. Given the *ideal gas* law, it is assumed that all the molecules are packed uniformly so that the relationship between the mean molecular spacing δ_{m} and the number density of the gas n_{m} is defined as $\delta_{\mathrm{m}} \propto n_{\mathrm{m}}^{-1/3}$. It is useful to compare the mean molecular spacing δ_{m} to the typical molecular diameter d to define the characteristic of the flow.

When the molecular spacing is an order of magnitude larger than the molecular diameter $\delta_\mathrm{m}/d \gg 1$ the gas is *dilute*. For dilute gases, it can be assumed that the characteristic time scale of intermolecular collisions t_c is significantly shorter than the mean flight time between two successive collisions t_mfp, so that $t_\mathrm{c} \ll t_\mathrm{mfp}$. This approximation indicates that binary intermolecular collisions are more common than simultaneous multiple collisions. Thus, the events involving three or more particles colliding simultaneously can be neglected [55].

When the mean molecular spacing δ_m approaches the characteristic scale of the molecular diameter d, the gas is defined as *dense*. In dense gases, molecules are closer together and therefore simultaneous multiple collisions are more frequent. This assumption complicates the treatment of intermolecular collision, and more complex models are required [39].

The kinetic theory description is limited to monatomic gases undergoing elastic collisions, so that all translational energy is conserved. Molecules consisting of several atoms require models that include rotational and vibrational energy [7].

2.3.1 Distribution Function

The kinetic theory description is based on the *particle distribution function* $f(\mathbf{x}, \boldsymbol{\xi}, t)$, which represents the density of particles with velocity $\boldsymbol{\xi} = (\xi_x, \xi_y, \xi_z)$ at position $\mathbf{x}$ and time t. The distribution function f can be connected to macroscopic variables by integrating it over the velocity space with appropriate weight functions. Those integrals are referred to as *moments of the distribution function* and they recover the following macroscopic quantities

- Mass density

$$\rho(\mathbf{x}, t) = \int f(\mathbf{x}, \boldsymbol{\xi}, t)\, d^3\boldsymbol{\xi}\,. \tag{2.11}$$

- Momentum density

$$\rho(\mathbf{x}, t)\, \mathbf{u}(\mathbf{x}, t) = \int \boldsymbol{\xi}\, f(\mathbf{x}, \boldsymbol{\xi}, t)\, d^3\boldsymbol{\xi}\,. \tag{2.12}$$

- Total energy density

$$\rho(\mathbf{x},t)\,E(\mathbf{x},t) = \frac{1}{2}\int |\xi^2|\, f(\mathbf{x},\boldsymbol{\xi},t)\, d^3\boldsymbol{\xi}\,. \tag{2.13}$$

Generally, intermolecular collisions and surface interactions tend to balance the angular distribution of particle velocities around the macroscopic mean velocity $\mathbf{u}$. Therefore, it is useful to assume that after a sufficiently long time the particle distribution function $f(\mathbf{x},\boldsymbol{\xi},t)$ relaxes to an *equilibrium distribution function* $f^{\mathrm{eq}}(\mathbf{x},\boldsymbol{\xi},t)$. The equilibrium distribution function is isotropic in velocity space around $\boldsymbol{\xi} = \mathbf{u}$. The deviation of the particle velocity $\boldsymbol{\xi}$ from the local mean velocity $\mathbf{u}$ defines the relative velocity $\mathbf{v}$

$$\mathbf{v}(\mathbf{x},t) = \boldsymbol{\xi}(\mathbf{x},t) - \mathbf{u}(\mathbf{x},t)\,. \tag{2.14}$$

In a reference frame moving with speed $\mathbf{u}$, the equilibrium distribution function can be expressed as

$$f^{\mathrm{eq}}(\mathbf{x},|\mathbf{v}|,t) = e^{3\mathrm{a}}\, e^{\mathrm{b}|\mathbf{v}|^2}\,, \tag{2.15}$$

where a and b are constants. Their value can be determined by constructing f^{eq} such that its moments are the same as those of the distribution function f due to the conservation of mass, momentum, and energy in monatomic collisions. In the original derivation proposed by Maxwell, the equilibrium distribution function f^{eq} is of the form

$$f^{\mathrm{eq}}(\mathbf{x},|\mathbf{v}|,t) = f\left(\frac{1}{2\pi RT}\right)^{3/2} e^{-|\mathbf{v}|^2/(2RT)}\,, \tag{2.16}$$

where R is the specific gas constant and T is the temperature. This form of the equilibrium distribution function is called the *Maxwell-Boltzmann distribution* and it represents an equilibrium state of the gas [7, 48, 56].

2.3.2 Boltzmann Equation

While the distribution function for a gas in an equilibrium state is given by the Maxwell-Boltzmann distribution, the evolution of the distribution function for a non-equilibrium

state is determined by the Boltzmann equation. The Boltzmann equation can be derived from the Liouville equation, but some important assumptions are required to complete its formulation [39, 57, 60, 61]

i. Only *binary collisions* are considered. Intermolecular collision events between three or more particles are neglected.

ii. It is assumed *molecular chaos*, so that the velocities of colliding particles are uncorrelated.

iii. Particles participate in *localised collisions* both in space and time.

Those assumptions can be fulfilled by considering a statistical distribution of particles and assuming that the time of intermolecular interaction is significantly shorter than the time between two successive collisions. This formulation of the Boltzmann equation is limited to dilute systems of monatomic gases undergoing elastic collisions. Then, the Boltzmann equation can be expressed in the form

$$\frac{\partial f}{\partial t} + \boldsymbol{\xi} \cdot \nabla f + \mathbf{F} \cdot \nabla_{\xi} f = \Omega(f)\,, \tag{2.17}$$

where $\mathbf{F}$ is an external body force. The first two terms of the Boltzmann equation represent the advection of the distribution function with velocity $\boldsymbol{\xi}$. The third term incorporates the external body force $\mathbf{F}$ affecting the distribution function. The source term $\Omega(f)$ represents the local redistribution of the distribution function due to collisional interactions and it is known as the *collision operator*. This term accounts for all the possible outcomes of binary collisions and encompasses any selection of intermolecular forces. The Boltzmann equation describes the evolution of a distribution function $f(\mathbf{x}, \boldsymbol{\xi}, t)$ participating in molecular transport and binary intermolecular collisions.

Since monatomic elastic collisions conserve the quantities of mass, momentum, and translational energy, they can be expressed as constraints for the moments of the collision operator Ω in the following way

- Mass conservation

$$\int \Omega(\mathbf{x}, \boldsymbol{\xi}, t)\, d^3\boldsymbol{\xi} = 0\,. \tag{2.18}$$

- Momentum conservation

$$\int \boldsymbol{\xi}\, \Omega(\mathbf{x}, \boldsymbol{\xi}, t)\, d^3\boldsymbol{\xi} = 0\,. \tag{2.19}$$

- Total energy conservation

$$\int |\xi|^2\, \Omega(\mathbf{x}, \boldsymbol{\xi}, t)\, d^3\boldsymbol{\xi} = 0\,. \tag{2.20}$$

The kinetic Boltzmann equation can be connected to the classical continuum description through the Chapman-Enskog analysis [7, 55, 56, 62]. The distribution function f is expressed as a perturbation expansion about f^{eq} to find the non-equilibrium contributions connected to phenomena such as viscous dissipation and heat diffusivity [7, 39, 48]. The distribution function f can be formally expanded in powers of a smallness parameter ϵ identified with the Knudsen number Kn

$$f = \sum_{n=0}^{\infty} \epsilon^n\, f^n = f^{(0)} + \epsilon\, f^{(1)} + \epsilon^2\, f^{(2)} + ... \tag{2.21}$$

Based on the assumption of a weak departure from local equilibrium, hydrodynamic equations can be recovered as the macroscopic limit of kinetic theory [39]. The zeroth order expansion in Kn corresponds to the Maxwell-Boltzmann distribution f^{eq}, leading to the inviscid Euler equations [39]. The first-order approximation recovers the Navier–Stokes equations with explicit expressions for the transport coefficients [7, 39]. It should be noted that the Navier–Stokes equations derived via the Chapman–Enskog expansion are not the most general form, as this derivation is limited to the context of binary collision mechanics and ideal gases [63].

2.3.3 Boundary Conditions

At the mesoscopic scale, solid walls affect the distribution function $f(\mathbf{x}, \boldsymbol{\xi}, t)$ [56]. Therefore, the Boltzmann equation should be solved alongside boundary conditions that take into account the influence of the gas–surface interaction [60]. On the surface of the boundary, the distribution function of incident particles moving with velocity $\boldsymbol{\xi}'$ is re-

lated to that of reflected molecules with velocity $\boldsymbol{\xi}$. The number of particles having the velocity in $d^3\boldsymbol{\xi}$ near $\boldsymbol{\xi'}$ and impinging the wall surface per area unit and per time unit is given by

$$-\,\xi'_{\mathrm{n}}\, f(\mathbf{x}, \boldsymbol{\xi'}, t)\, d^3\boldsymbol{\xi'} \qquad \xi'_{\mathrm{n}} = \boldsymbol{\xi'} \cdot \mathbf{n}\,, \tag{2.22}$$

where $\mathbf{n}$ is the unit vector normal to the surface and directed towards the bulk flow. Correspondingly, the wall surface reflects the number of particles having the velocity in $d^3\boldsymbol{\xi}$ near $\boldsymbol{\xi'}$ can be expressed as

$$\xi_{\mathrm{n}}\, f(\mathbf{x}, \boldsymbol{\xi}, t)\, d^3\boldsymbol{\xi} \qquad \xi_{\mathrm{n}} = \boldsymbol{\xi} \cdot \mathbf{n}\,. \tag{2.23}$$

Then, the probability density that molecules hitting the wall with velocity between $\boldsymbol{\xi'}$ and $\boldsymbol{\xi'} + d^3\boldsymbol{\xi'}$ at location $\mathbf{x}$ at time t are reflected with velocity between $\boldsymbol{\xi}$ and $\boldsymbol{\xi} + d^3\boldsymbol{\xi}$ is given by

$$R\left(\boldsymbol{\xi'} \to \boldsymbol{\xi};\, \mathbf{x}, t\right)\,, \tag{2.24}$$

where R is the non-negative *scattering kernel*. Thus, the boundary condition for the distribution function $f(\mathbf{x}, \boldsymbol{\xi}, t)$ can be expressed as

$$f(\mathbf{x}, \boldsymbol{\xi}, t)\, \xi_{\mathrm{n}} = \int H\left(-\xi_{\mathrm{n}}\right) \left|\xi_{\mathrm{n}'}\right|\, R\left(\boldsymbol{\xi'} \to \boldsymbol{\xi};\, \mathbf{x}, t\right)\, f(\mathbf{x}, \boldsymbol{\xi'}, t)\, d^3\boldsymbol{\xi'}\,, \tag{2.25}$$

where H is the Heaviside step function. If there is no adsorption on the wall surface, then

$$\int H\left(\xi_{\mathrm{n}}\right)\, R\left(\boldsymbol{\xi'} \to \boldsymbol{\xi};\, \mathbf{x}, t\right)\, d^3\boldsymbol{\xi'} = 1\,. \tag{2.26}$$

There are several models of scattering kernels that express the different interactions between the gas molecules and the wall surface [55]. Scattering kernels express complex interactions and therefore obtaining their complete form is usually challenging [60]. However, to describe gas–surface interactions at the macroscopic level it is sufficient to know some integral characteristics of the scattering kernels [7]. Those average parameters are called *accommodation coefficients* and they describe momentum and energy transfer between the molecules and the wall. The thermal accommodation coefficient is

given by

$$\sigma_{\mathrm{T}} = \frac{dE_{\mathrm{i}} - dE_{\mathrm{r}}}{dE_{\mathrm{i}} - dE_{\mathrm{w}}}\,, \tag{2.27}$$

where dE_{i} and dE_{r} are the energy fluxes of incoming and reflected molecules per unit time, respectively. The term dE_{w} denotes the energy flux corresponding to incoming molecules reflected with the energy flux equivalent to the surface temperature T_{w}. The condition $\sigma_{\mathrm{T}} = 1$ corresponds to the perfect energy exchange.

The tangential momentum accommodation coefficient defines the tangential momentum exchange between the gas molecules and the wall surface

$$\sigma_{\xi} = \frac{\tau_{\mathrm{i}} - \tau_{\mathrm{r}}}{\tau_{\mathrm{i}} - \tau_{\mathrm{w}}}\,, \tag{2.28}$$

where τ_{i} and τ_{r} are respectively the tangential momentum of incoming and reflected molecules, and τ_{w} is the tangential momentum of reflected molecules corresponding to that of the wall surface. The most important limits for the accommodation coefficient values correspond to the following cases [56]

- $\sigma_{\xi} = 0$ corresponds to *specular reflection*. In this case, the tangential velocity of the reflected molecules is unchanged, but the normal velocity is reversed due to the normal momentum transfer to the surface. The fluid does not exchange tangential momentum with the wall, resulting in the limit of *inviscid flow*.

- $\sigma_{\xi} = 1$ corresponds to *diffuse reflection*. In this case, the molecules are reflected with zero average tangential velocity. Therefore, the fluid exchanges tangential momentum with the walls. This corresponds to the so-called *perfect accommodation*, because the molecules are reflected with a Maxwellian distribution function despite their initial tangential momentum.

The original model proposed by Maxwell for the scattering kernel is of the form

$$R\left(\boldsymbol{\xi}' \to \boldsymbol{\xi};\, \mathbf{x}\right) = (1 - \sigma_{\xi})\,\delta\,\left(\boldsymbol{\xi}' - \boldsymbol{\xi} + 2\,\mathbf{n}\,\xi_{\mathrm{n}}\right) + \frac{2\,\sigma_{\xi}\,\beta_{\mathrm{w}}^{4}}{\pi}\,e^{\left(-\beta_{\mathrm{w}}^{2}\,\xi^{2}\right)}\,. \tag{2.29}$$

The most popular scattering kernel is the *Cercignani–Lampis model*, which includes Brownian motion [7, 55]. It introduces the tangential accommodation coefficient, $0 \leq$

$\sigma_t \leq 2$, and the normal accommodation coefficient, $0 \leq \sigma_n \leq 1$. It can be formulated as

$$R\left(\boldsymbol{\xi}' \rightarrow \boldsymbol{\xi}; \mathbf{x}\right) = \frac{2\,\sigma_t\,\sigma_n\,(2-\sigma_t)\,\beta_w^4}{\pi} \exp\left(-\beta_w^2\,\frac{\xi_n^2 + (1-\sigma_n)\,(\xi_n')^2}{\sigma_n} - \beta_w^2\,\frac{(\xi_t - (1-\sigma_t)\,\xi_t')^2}{\sigma_t\,(2-\sigma_t)}\right) I_0\left(\beta_w^2\,\frac{2\sqrt{1-\sigma_t}\,\xi_n\,\xi_n'}{\sigma_t}\right), \tag{2.30}$$

where I_0 is the zeroth-order modified Bessel function of the first kind.

2.4 Fluid-Structure Interaction

A fluid–structure interaction problem is characterised by a set of governing equations that must be satisfied in the fluid domain and corresponding equations for solid motion, together with coupling conditions that enforce physically consistent behaviour at the interface. In general, the domain of a fluid-structure interaction problem can be schematically represented by a solid domain Ω_s, a fluid domain Ω_f and a boundary $\Gamma_s = \Omega_s \cap \Omega_f$, as shown in Figure 2.1. The flow behaviour depends on the instantaneous position and motion of the solid, while the solid responds to the hydrodynamic forces exerted by the surrounding fluid. At the interface, the kinematic compatibility condition requires continuity of velocity, which in the case of a rigid body is equivalent to the no-slip condition.

Within this framework, the solid dynamics are described by the equations of motion and by the associated balances of linear and angular momentum, while interactions between different bodies are represented through a contact model. These elements provide the physical basis on which the numerical formulation presented in the following chapters is built.

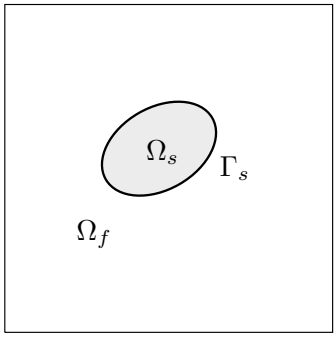


Figure 2.1: Schematic representation of a generic FSI domain, with the solid domain Ω_s, the fluid domain Ω_f, and the interface Γ_s.

2.4.1 Equations of Motion

The motion of a rigid particle immersed in a fluid is governed by Newton's second law. For the translational motion, this can be expressed in the form

$$m_\mathrm{p} \frac{\mathrm{d}^2 \mathbf{X}_\mathrm{p}}{\mathrm{d}t^2} = \mathbf{F}_\mathrm{p}\,, \tag{2.31}$$

where m_p is the mass of the particle, $\mathbf{X}_\mathrm{p}$ are the coordinates of the particle centre, and $\mathbf{F}_\mathrm{p}$ is the force acting on the particle. The equations of motion for the rotational degree of freedom are given by

$$I_\mathrm{p} \frac{\mathrm{d}^2 \boldsymbol{\theta}_\mathrm{p}}{\mathrm{d}t^2} = \mathbf{T}_\mathrm{p}\,, \tag{2.32}$$

where I_p is the moment of inertia, $\boldsymbol{\theta}_\mathrm{p}$ is the angular displacement of the particle centre and $\mathbf{T}_\mathrm{p}$ is the total torque.

2.4.2 Momentum Balance Equations

The dynamics of a coupled fluid–solid system can be described by applying the momentum balance to the solid domain Ω_s bounded by the interface Γ_s. The conservation of linear momentum requires that the total external force acting on the solid domain equals the rate of change of the total momentum of the system. The external forces consist of contributions of volume forces $\mathbf{f}_\mathrm{v}$ arising from fields acting on the whole domain, and

surface forces. The momentum balance equation can be expressed as

$$\frac{\mathrm{d}}{\mathrm{d}t}\int_{\Omega_\mathrm{s}} \rho_\mathrm{f}\,\mathbf{u}\,dV = \int_{\Omega_\mathrm{s}} \rho_\mathrm{f}\,\mathbf{f}_\mathrm{v}\,dV + \int_{\Gamma_\mathrm{s}} \boldsymbol{\tau}\cdot\mathbf{n}\,dS\,, \tag{2.33}$$

where ρ_f is the fluid density, $\boldsymbol{\tau}$ is the hydrodynamic stress tensor and $\mathbf{n}$ is the unit normal vector. In the following discussion, the hydrodynamic force is considered the only body force source $\mathbf{F}_\mathrm{p}$ applied on the immersed structure by the surrounding fluid. Therefore, the equations of motion for a structure immersed in a fluid can be determined from the conservation of linear momentum

$$\mathbf{F}_\mathrm{p} = \int_{\Gamma_\mathrm{s}} \boldsymbol{\tau}\cdot\mathbf{n}\,dS\,. \tag{2.34}$$

Considering Equation 2.33, the equation of motion given by Equation 2.34 can be modified as follows

$$\mathbf{F}_\mathrm{p} = \frac{\mathrm{d}}{\mathrm{d}t}\int_{\Omega_\mathrm{s}} \rho_\mathrm{f}\,\mathbf{u}\,dV - \int_{\Omega_\mathrm{s}} \rho_\mathrm{f}\,\mathbf{f}_\mathrm{v}\,dV\,, \tag{2.35}$$

An analogous relation follows from the balance of angular momentum

$$\frac{\mathrm{d}}{\mathrm{d}t}\int_{\Omega_\mathrm{s}} \rho_\mathrm{f}\,\mathbf{r}\times\mathbf{u}\,dV = \int_{\Omega_\mathrm{s}} \rho_\mathrm{f}\,\mathbf{r}\times\mathbf{f}_\mathrm{v}\,dV + \int_{\Gamma_\mathrm{s}} \mathbf{r}\times(\boldsymbol{\tau}\cdot\mathbf{n})\,dS\,, \tag{2.36}$$

where $\mathbf{r}$ is the position vector of the surface point with respect to the centre of the immersed structure. The angular equation of motion is given by

$$\mathbf{T}_\mathrm{p} = \int_{\Gamma_\mathrm{s}} \mathbf{r}\times(\boldsymbol{\tau}\cdot\mathbf{n})\,dS\,. \tag{2.37}$$

The surface force in Equation 2.36 can be formulated using the corresponding expression determined by Equation 2.37

$$\mathbf{T}_\mathrm{p} = \frac{\mathrm{d}}{\mathrm{d}t}\int_{\Omega_\mathrm{s}} \rho_\mathrm{f}\,\mathbf{r}\times\mathbf{u}\,dV - \int_{\Omega_\mathrm{s}} \rho_\mathrm{f}\,\mathbf{r}\times\mathbf{f}_\mathrm{v}\,dV\,. \tag{2.38}$$

2.4.3 Contact Model

In fluid–structure interaction problems, solid bodies may come into contact with each other or with boundaries, generating additional forces. These interactions are described using a contact model that relates the interaction force to the relative motion and local deformation at the contact point.

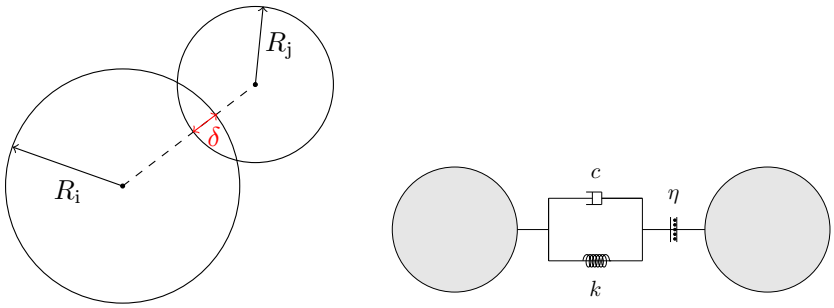
In the *soft-sphere* formulation [64], particles are treated as deformable bodies that undergo small, reversible deformations during contact and recover their original shape once the contact is released [65]. Interactions are modelled by allowing a small overlap between the contacting particles, which represents local elastic deformations at the points of contact [66, 67]. The contact forces are then evaluated as functions of the overlap between particles and the relative velocity at the contact point [68]. Considering a pair of particles of radii R_i and R_j, as shown in Figure 2.2, their normal overlap distance δ_n is given by

$$\delta_\mathrm{n} = (R_\mathrm{i} + R_\mathrm{j} + \varepsilon_\mathrm{c}) - |\mathbf{X}_\mathrm{i} - \mathbf{X}_\mathrm{j}| \ , \tag{2.39}$$

where $\mathbf{X}_\mathrm{i}$ and $\mathbf{X}_\mathrm{j}$ are the centre coordinates and ε_c is a user defined critical distance. The unit normal vector is $\mathbf{n} = (\mathbf{X}_\mathrm{i} + \mathbf{X}_\mathrm{j}) \,/\, |\mathbf{X}_\mathrm{i} - \mathbf{X}_\mathrm{j}|$. The relative particle velocity at contact point $\mathbf{V}_\mathrm{ij}$ is defined as

$$\mathbf{V}_\mathrm{ij} = (\mathbf{U}_\mathrm{i} + \mathbf{U}_\mathrm{j}) + R_\mathrm{i}\, \mathbf{n} \times \boldsymbol{\Theta}_\mathrm{i} + R_\mathrm{j}\, \mathbf{n} \times \boldsymbol{\Theta}_\mathrm{j} \, , \tag{2.40}$$

where $\mathbf{U}$ and $\boldsymbol{\Theta}$ are respectively the translational and the angular velocities of the particles' centre of mass. A linear spring-dashpot model is applied to both particle-particle and particle-wall interactions when the distance is less than the critical value ε_c [69]. This model represents contact interactions through a combination of linear mechanical elements, where the spring accounts for the elastic response of the material and the dashpot introduces energy dissipation associated with plastic deformations [70]. The contact force $\mathbf{F}_\mathrm{c}$ can be decomposed into normal F_cn and tangential F_ct terms that



(a) *Particle interaction.* (b) *Contact model.*

Figure 2.2: Schematic representation of the contact between two particles: (a) particle interaction and (b) contact model.

are respectively calculated as follows

$$F_{cn} = k_n \, \delta_n + c_n \, v_n \,, \tag{2.41a}$$

$$F_{ct} = \begin{cases} k_t \, \Delta \, \delta_t + c_t \, v_t & F_{ct} < \eta \, F_{cn} \,, \\ \eta \, F_{cn} & F_{ct} \geq \eta \, F_{cn} \,, \end{cases} \tag{2.41b}$$

where k_n, k_t are the normal and tangential spring coefficients, c_n, c_t are the normal and tangential damping coefficients, $\Delta \, \delta_t$ is the relative tangential displacement, and η is the friction coefficient. The relative normal velocity at contact point is $v_n = -\mathbf{V}_{ij} \cdot \mathbf{n}$ and the relative tangential velocity at contact point is $v_t = -\mathbf{n} \times (\mathbf{V}_{ij} - v_n \, \mathbf{n})$. The contact force is defined as the sum of an elastic component, proportional to the overlap through the spring stiffness, and a viscous damping component, proportional to the relative velocity. The elastic force term conserves the kinetic energy of collision, while the viscous term accounts for energy dissipation during contact. In the tangential direction, a frictional slider is introduced to represent the onset of sliding according to Coulomb's friction law [65].

2.5 Vortex-Induced Vibrations

Vortex-induced vibrations (VIV) are a type of flow-induced vibrations phenomena typically occurring in steady external flow around bluff bodies. The study of VIV encompasses many disciplines and its significance and practical importance have led to

numerous research investigations [4, 71, 72]. Accurate understanding of this problem is particularly relevant for vibration suppression as well as new applications in energy harvesting [4, 73, 74].

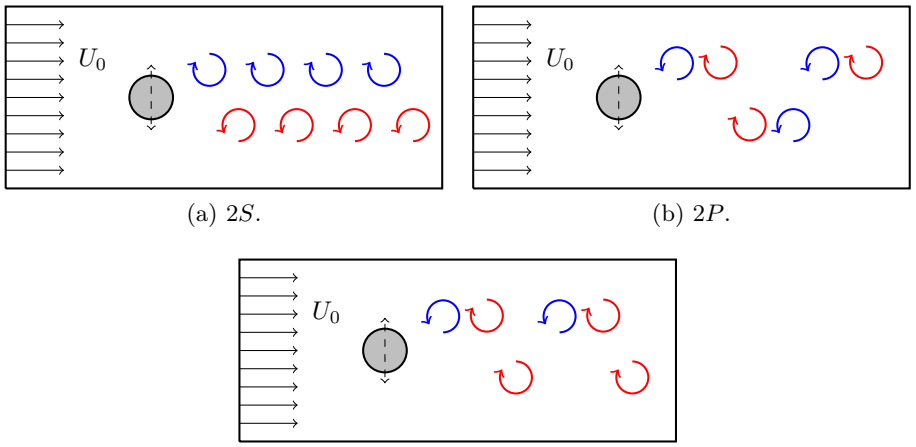
2.5.1 Vortex Shedding Mechanisms

One of the fundamental mechanisms underlying VIV is the flow instability associated with vortex shedding. Because of the mutual interaction between fluid and structure, vortex shedding exerts fluctuating forces on the solid object, resulting in a periodic pressure distribution. Vibrations in the direction transversal to the flow have a dominant excitation frequency corresponding to the vortex shedding frequency. Synchronisation occurs when the natural frequency of the structure is close to the vortex shedding frequency, resulting in a lock-in regime characterised by large amplitude oscillations. In case of unsteady problems, an additional vibration mechanism is associated to oscillating flow where velocity fluctuations cause variations of the drag and inertia forces [75].

Williamson and Roshko [76] investigated the wake patterns near the fundamental lock-in region for a transversely oscillating cylinder. They reported different modes of vortex formation and identified patterns involving single vortex (S) and vortex pair (P) combinations. VIV phenomena can result in 2S wake patterns with two single vortices shed in each cycle, similar to the classic vortex street wake. A different mode, termed 2P, involves the formation of a vortex pair in each cycle of body motion. For forced vibrations problems, additional patterns include the P+S mode comprising a pair and a single vortex shed in each cycle. The main vortex shedding modes are schematised in Figure 2.3, showing the characteristic 2S, 2P, and P+S wake patterns.

2.5.2 Structural Response Regimes

Numerous studies focused on understanding the role of different characteristic parameters associated with large amplitude vibration, such as the mass ratio m^* given by the ratio of structural mass to the mass of the fluid it displaces, the reduced velocity U^*, defined as the free-stream velocity normalised by the natural frequency and characteristic length of the system, and the structural damping ratio ζ. Khalak and Williamson [77]



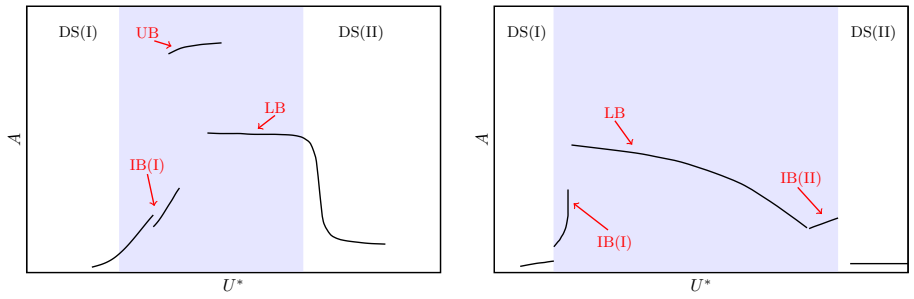
(a) $2S$. (b) $2P$.

(c) $P+S$.

Figure 2.3: Schematic representation of the main vortex shedding modes observed in VIV problems: (a) alternate shedding of two single vortices per cycle (2S), (b) shedding of two vortex pairs per cycle (2P), and (c) shedding of a vortex pair on one side and a single vortex on the opposite side per cycle (P+S). The dashed line indicates the trajectory of the cylinder centre.

studied systems characterised by low mass-damping ratios in a high Reynolds number regime and identified three different branches of response during the lock-in regime, namely the initial, upper and lower branches. The upper branch corresponds to the peak amplitude oscillations, and the system is in a desynchronised state outside the lock-in regime. Different works demonstrated that the initial branch of response is associated with the 2S mode of vortex formation, while the lower branch exhibits a 2P pattern [71, 78]. The amplitude response for the flow past a freely vibrating cylinder in the high Reynolds number regime ($4000 \leq Re \leq 3\times10^4$) and the associated sequence of branches within the lock-in regime are schematically illustrated in Figure 2.4 [74, 78].

Different investigations indicated that the range of reduced velocities over which large amplitudes occur increases as the mass ratio m^* is decreased [71, 79]. Govardhan and Williamson [80] showed that the synchronization regime extends up to infinite reduced velocity when the mass ratio m^* is less than a critical value m^*_c termed *critical mass ratio*. In such cases, the lower response branch ceases to exist, and the vortex formation mode is associated with the upper branch. The experimental study indicated that $m^*_c = 0.54$ and for $m^*_c < 0.54$ large amplitude oscillations are observed, correspond-



(a) High Re regime. (b) Low Re regime.

Figure 2.4: Schematic representation of the amplitude response as a function of the reduced velocity for the flow past a freely vibrating cylinder. The shaded region indicates the lock-in regime, within which distinct response branches are observed. Outside this range, the system is in a desynchronized state (DS(I) and DS(II)). (a) High Re regime: the response consists of the initial branch (IB(I)), upper branch (UB), and lower branch (LB). (b) Low Re regime: the response exhibits three branches IB(I), LB, and IB(II). Adapted from Navrose and Mittal [74]

ing to the *resonance forever* phenomenon. Various studies at high Reynolds number highlighted that the response amplitude exhibits a sharp increase as the mass ratio is decreased below the critical value m_c^*, corresponding to the upper branch response with a 2P vortex shedding mode. It was demonstrated that the value of the critical mass ratio increases with the Reynolds number. Conversely, mass ratio values greater than m_c^* correspond to the lower branch associated with a 2S vortex shedding pattern [74,80].

The laminar flow regime corresponding to $40 \leq Re \leq 200$ is characterised by three response branches, defined as initial branch I, lower branch and initial branch II [74]. In this case, the largest oscillation amplitude is associated with the lower branch and it is significantly lower than the high Re case [74,80]. The different branches of response in the low Reynolds number regime are schematically represented in Figure 2.4. Different studies at low Reynolds number proved that the structural response is associated with a 2S vortex shedding mode [81–83]. Shiels et al. [84] investigated the transverse oscillation of a circular cylinder at $Re = 100$ for a limiting case with mass, damping and stiffness set to zero. It was demonstrated that the cylinder vibrates sinusoidally with large amplitude oscillations at a frequency close to the vortex shedding frequency. Ryan et al. [85] studied the flow-induced vibration of a circular cylinder oscillating transversely

to the flow in the Reynolds number interval $30 \leq Re \leq 200$ for an infinite reduced velocity. The research indicated two separate regions of high amplitude oscillations: the viscous region $40 \leq Re \leq 95$ and the higher Reynolds number region $180 \leq Re \leq 200$. In the Reynolds number range $100 \leq Re \leq 170$, the cylinder response exhibits low amplitude oscillations which decrease with decreasing mass ratio values. They defined the critical mass ratio m_c^* as the mass ratio corresponding to a jump in the amplitude of the response and determined its values as a function of Reynolds number. In the viscous region m_c^* decreases as the Reynolds number increases, while no critical mass ratio could be defined in the range $100 \leq Re \leq 170$.

2.6 Summary

This chapter introduced the mathematical description supporting the modelling approach and established the theoretical framework used in the following work. Characteristic scales and parameters were first introduced to provide an overview of the mathematical description of fluid dynamics. The continuum theory was outlined, focusing on conservation laws and the definition of the stress tensor. The fundamental concepts of the mesoscopic description of fluid dynamics were introduced, and the principles of kinetic theory were discussed to derive the Boltzmann equation.

A mathematical framework for fluid–structure interaction was formulated, including the governing equations, the associated momentum balance, and the treatment of contact interactions. Finally, the main features of vortex-induced vibrations were discussed as an important application of fluid–structure interaction, illustrating the underlying physical mechanisms.

Chapter 3

Numerical Methods

This chapter presents the numerical methods considered to model fluid-solid interaction problems and discusses in detail their implementation in the lattice Boltzmann framework. Section 3.1 provides an overview of the numerical methods, including strategies for coupling the motion of the fluid and the structure and representing the fluid–solid interface.

The lattice Boltzmann method is introduced in Section 3.2 as the fluid solver adopted in this work. Based on the principles of kinetic theory, the lattice Boltzmann equation is derived, and its general numerical implementation is discussed. Different solutions to model the complex collision operator are presented with a focus on the central moment method and the corresponding forcing scheme. Additionally, an overview of the most common boundary conditions is provided, including the strategies to model fluid-solid boundary conditions for moving geometries and complex shape problems.

The fundamental concepts of the immersed boundary method are discussed in Section 3.3 as a strategy to represent moving solid bodies and their interaction with the surrounding fluid. Focusing on its implementation within the LBM framework (IB-LBM), the key ideas behind the representation of the fluid-solid domain and the enforcement of the no-slip boundary condition are presented. To improve the accuracy and efficiency of the general IBM scheme, the multi-direct-forcing method (MDF) is introduced, and its implementation is discussed in detail. In order to accelerate the convergence rate, the relaxed MDF scheme is considered, and its numerical realisation

and advantages are analysed. To provide a complete description of the challenges posed by the numerical implementation of the IBM, the internal mass effect is explained, and different mitigation strategies are systematically compared. The extension to a strongly coupled formulation is also presented to address stability issues related to the fluid-solid coupling strategy.

Section 3.4 aims to provide a brief introduction to the discrete element method for modelling particle contacts and the associated interaction forces. Finally, the combined DEM-IB-CLMB approach is presented, and its numerical implementation is summarised in Section 3.5.

3.1 Numerical Framework

The methodology developed in this work integrates different numerical approaches that interact consistently within a coupled fluid–structure setting. Before presenting the detailed formulations, the broader context in which these methods operate is outlined. First, an overview of numerical methods commonly employed in fluid and particle dynamics is provided, highlighting their characteristic scales and governing equations. The discussion then focuses on fluid–structure problems, introducing the most common approaches to couple the governing equations of the two domains. Finally, different strategies for representing moving interfaces are reviewed, with emphasis on body-non-conforming methods.

3.1.1 Overview of Numerical Methods

Covering the range from microscale to macroscale, a plethora of numerical methods have been introduced to solve fluid dynamics problems. A schematic overview of the most popular numerical methods, their reference scales and governing equations is given in Table 3.1.

At the microscopic level, one of the most powerful simulation methods is molecular dynamics (MD) [86,87]. This approach is based on the integration of Newton's equation of motion to compute the trajectories of particles that model the atoms and molecules

Table 3.1: Overview of commonly used numerical methods classified according to their characteristic reference scales and governing equations.

Description	Scale	Equation	Method
Macroscopic	$\ell\,, t$	Navier-Stokes	FDM FVM FEM
Mesoscopic	$\ell_{\mathrm{mfp}}\,, t_{\mathrm{mfp}}$	Boltzmann	LBM DVM DSMC
Microscopic	$\ell_{\mathrm{a}}\,, t_{\mathrm{c}}$	Newton	MD

of the system [7]. Particle interaction is governed by interatomic forces, which are modelled by intermolecular potentials [86, 88].

Mesoscale methods bridge the gap between atomistic and continuum models. Dissipative particle dynamics (DPD) captures larger length and time scales than MD by modelling particles that correspond to coarse-grained entities, rather than individual atoms [7, 89]. Another effective particle-based method is the discrete element method (DEM), which is discussed in detail in Section 3.4.

Mesoscopic methods based on kinetic theory can be broadly classified into deterministic and stochastic models. The most popular deterministic method is the discrete velocity method (DVM), based on a discrete approximation of the Boltzmann equation that leads to the discrete velocity Boltzmann equation [60, 90]. Other closely related methods are the unified gas kinetic scheme (UGKS) and the discrete unified gas kinetic scheme (DUGKS) [91, 92]. Another popular deterministic mesoscopic method is the LBM [93, 94]. This approach historically originated from the lattice gas cellular automata (LGCA) and it can be conceptually considered as a special form of the DVM [60, 94, 95]. A more detailed discussion of this method and its limitations is presented in Section 3.2. The most popular stochastic method for mesoscopic systems is the direct simulation Monte Carlo (DSMC) [55, 87, 88]. This approach incorporates the physical effects governed by the Boltzmann equation by using a set of statistically representative particles [7].

The most common macroscopic methods are the finite difference method (FDM),

the finite volume method (FVM) and the finite element method (FEM) [58, 96–98]. These conventional numerical methods use different approaches to discretise and solve the Navier-Stokes equations [42, 99]. Additionally, the spectral element method (SEM) stands out as a higher-order model that combines the FEM with the accuracy of spectral techniques [100].

3.1.2 Coupled Fluid–Structure Problems

FSI problems comprise a fluid and a solid domain that are governed by a coupled system of equations. Numerical methods for the solution of the coupled governing equations of fluid and structural motion are generally classified into monolithic and partitioned approaches [43, 101, 102].

Monolithic approaches solve the flow and structural equations simultaneously using a single solver [10, 103]. Since the mutual influence of the governing equations is directly taken into account, the enforcement of the coupling conditions at the interface is achieved exactly, and these approaches are unconditionally stable [1]. However, this strategy generally entails significant computational costs and does not allow the selection of suitable modular solvers with different numerical methods for fluid and solid equations [43].

Conversely, partitioned approaches treat the fluid and solid domains as distinct and solve the corresponding equations separately using different solvers [104]. This strategy requires a coupling algorithm that determines the interaction and information transfer between the solvers to ensure that the boundary conditions at the interface are accurately modelled [10].

Partitioned approaches can be further classified into weakly coupled and strongly coupled methods based on the strategy implemented for the time integration of the structural governing equations [43, 105]. In weakly coupled schemes, the solution of the fluid and structural equations is performed in a sequential manner at each time step [102, 106–108]. This approach retains the advantage of a simple implementation of the coupling strategy between the different solvers, and the computational cost per time step is fixed since no iterations are required.

Strongly coupled schemes implement a concurrent solution of the fluid and structural equations by performing an iterative process at each time step until the coupled solution converges. This strategy improves temporal accuracy, but generally the iterations required at each time step increase the computational costs significantly. Different iterative methods have been implemented to solve the coupled system of equations [109–111]. The block Gauss–Seidel method has the advantage of a simple implementation but requires an under-relaxation scheme to improve the convergence rate [43, 104, 112]. Alternatively, Newton–Raphson methods do not require free parameters and generally converge rapidly, but they involve the computation of Jacobian matrices, which increase the costs significantly [10, 113, 114].

3.1.3 Interface Representation

Analysing FSI domains with complex geometry can be a challenging task in terms of boundary treatment [10]. In this context, two general strategies can be distinguished. A body-conforming grid covers the fluid domain Ω_f and fits the shape of the boundary Γ_s, separating it from the solid domain Ω_s. Alternatively, a non-conforming computational grid is not fitted to the solid body and spans the entire geometry $\Omega_f \cup \Omega_s$.

When body-fitted computational grids are considered, increased geometrical complexity can often lead to time-consuming mesh generation procedures and deterioration of grid quality. Furthermore, problems involving moving boundaries require grid generation at every time step, which introduces additional computational costs and can negatively impact the robustness of the solution. An alternative solution to describe complex domains is to define a time-invariant non-conforming computational grid and introduce additional procedures to account for the shape of the boundary.

Numerical approaches of this type are often distinguished as *front-tracking* or *front-capturing* methods [115]. In front-capturing methods, the interface separating two different fluid regions is identified using a marker function defined on the fixed grid and advected with the fluid motion [116]. The most widely used techniques are the volume-of-fluid (VOF) method [117], which computes the local volume fraction of each fluid, and the level-set method [118, 119], where the interface is represented as the zero level

set of a smooth function [42]. In contrast, front-tracking methods represent the interface explicitly by connected marker points, as in the implementation of Tryggvason et al. [120].

In close analogy to front-tracking methods used for multiphase flows, the IBM is an effective body non-conforming technique to simulate complex solid objects and moving geometries [1, 3]. This is achieved by solving the flow field on a fixed computational grid and representing the boundary with a set of moving marker points. This approach eliminates the need to remesh the underlying grid for moving objects problems, since the marker points can be used to model the time-varying geometry. A detailed discussion of the IBM formulation is presented in Section 3.3.

3.2 Lattice Boltzmann Method

The LBM originated from the Lattice Gas Cellular Automata (LGCA), building on its simplicity of formulation and implementation [56,121,122]. The fundamental idea of the LBM is to simplify the complexity of the continuous Boltzmann equation by deriving a discrete form in space and time and reducing the velocity space to a discrete set of velocities [123].

Due to the kinetic roots of the Boltzmann equation, the LBM incorporates the physics of microscopic interactions and describes the macroscopic dynamics as the result of the collective behaviour of microscopic particles. Therefore, the LBM is capable of modelling fluid flow with a high Knudsen number. The LBM has become increasingly popular because of its high level of scalability on parallel processing systems and its efficiency in handling complex geometries [56]. Furthermore, the linear convention operator simplifies the formulation of LBM significantly compared to the macroscopic methods [44].

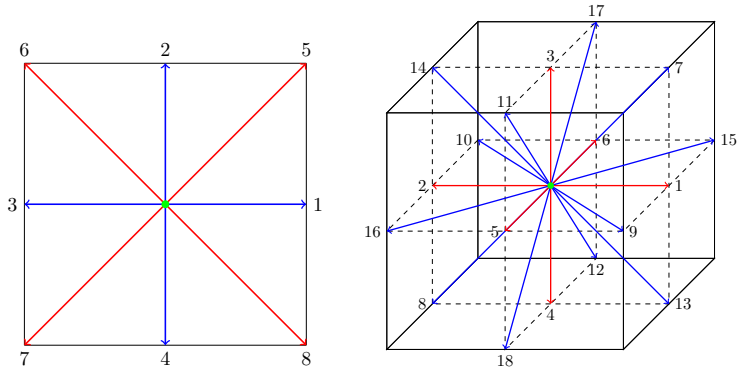
3.2.1 Lattice Boltzmann Equation

At the core of the LBM is the Lattice Boltzmann Equation (LBE), which forms the basis for its numerical framework. Rather than considering the continuous distribution func-

tions $f(\mathbf{x}, \boldsymbol{\xi}, t)$, the LBE models the evolution of discrete distribution functions based on a finite set of velocities [123]. The velocity-space discretisation of the Boltzmann equation begins with the equilibrium distribution f^{eq}, given by the Maxwell-Boltzmann distribution introduced in Equation 2.16. This function can be expressed through a Hermite series expansion, whose coefficients are directly related to the conserved moments of the distribution function. By truncating the series after the first three terms, the equilibrium distribution can be expressed in reduced form while retaining the correct mass and momentum integrals [48]. The integrals are then replaced by finite weighted sums using the Gauss–Hermite quadrature, which specifies both the discrete velocity vectors $\mathbf{c}_i$ and the corresponding weights w_i. The resulting discrete equilibrium distribution f_i^{eq} is defined as

$$f_i^{\text{eq}}(\mathbf{x}, t) = w_i \rho \left(1 + \frac{\mathbf{u} \cdot \mathbf{c}_i}{c_s^2} + \frac{(\mathbf{u} \cdot \mathbf{c}_i)^2}{2c_s^4} - \frac{\mathbf{u} \cdot \mathbf{u}}{2c_s^2} \right) , \tag{3.1}$$

where c_s represents the speed of sound. The same discretisation methodology is applied to the distribution function $f(\mathbf{x}, \boldsymbol{\xi}, t)$, resulting in the *discrete-velocity distribution function* $f_i(\mathbf{x}, t)$, which represents the density of particles with discrete velocity $\mathbf{c}_i = (c_{ix}, c_{iy}, c_{iz})$ at position $\mathbf{x}$ and time t. The discrete velocities $\mathbf{c}_i$ together with the corresponding set of weighting coefficients w_i define velocity sets $\{\mathbf{c}_i, w_i\}$. They are indicated as DdQq, where d is the size of spatial dimensions and q is the number of



(a) *D2Q9* (b) *D3Q19*

Figure 3.1: Schematics of D2Q9 and D3Q19 velocity sets.
Schematics of the discrete velocity vectors $\mathbf{c}_i$ for the D2Q9 and D3Q19 velocity sets.

discrete velocities. Figure 3.1 shows the velocity sets that are most commonly used for 2D and 3D simulations, i.e. the D2Q9 and D3Q19 sets [124]. Each velocity set defines a lattice constant c_s that represents the speed of sound and determines the relation between the macroscopic pressure and density $p = {c_s}^2\rho$. The velocity sets and their corresponding weights are listed in Table 3.2 for the D2Q9 velocity set and Table 3.3 for the D3Q19 velocity set.

After defining the discrete velocity space, the Boltzmann equation is further discretised in space and time using the method of characteristics. In this formulation, the discrete-velocity distribution function $f_i(\mathbf{x}, t)$ is defined only at the nodes of a regular lattice with spacing Δx and at times t, evolving in discrete time steps Δt. The discretisation of the Boltzmann equation in velocity space, physical space, and time results in the Lattice Boltzmann Equation, expressed in the following form

Table 3.2: Discrete velocity directions $\mathbf{c}_i$ and corresponding weights w_i for the D2Q9 velocity set.

i	w_i	c_{ix}	c_{iy}
0	4/9	0	0
1	1/9	+1	0
2	1/9	0	+1
3	1/9	-1	0
4	1/9	0	-1
5	1/36	+1	+1
6	1/36	-1	+1
7	1/36	-1	-1
8	1/36	+1	-1

$$f_i(\mathbf{x} + \mathbf{c}_i\Delta t, t + \Delta t) = f_i(\mathbf{x}, t) + \Omega_i(\mathbf{x}, t)\,. \tag{3.2}$$

This equation presents the two main processes of the method, i.e. streaming and collision. Particle populations $f_i(\mathbf{x}, t)$ stream with velocity $\mathbf{c}_i$ to a neighbouring point $(\mathbf{x} + \mathbf{c}_i\Delta t)$ at time $(t + \Delta t)$. The collision operator Ω_i models particle collisions by redistributing particles at each site. The discrete velocity vectors $\mathbf{c}_i$ are defined so that a fluid particle streams from one lattice site to a neighbouring one and collides exactly

Table 3.3: Discrete velocity directions $\mathbf{c}_i$ and corresponding weights w_i for the D3Q19 velocity set.

i	w_i	c_{ix}	c_{iy}	c_{iz}
0	1/3	0	0	0
1	1/18	+1	0	0
2	1/18	-1	0	0
3	1/18	0	+1	0
4	1/18	0	-1	0
5	1/18	0	0	+1
6	1/18	0	0	-1
7	1/36	+1	+1	0
8	1/36	-1	-1	0
9	1/36	+1	0	+1
10	1/36	-1	0	-1
11	1/36	0	+1	+1
12	1/36	0	-1	-1
13	1/36	+1	-1	0
14	1/36	-1	+1	0
15	1/36	+1	0	-1
16	1/36	-1	0	+1
17	1/36	0	+1	-1
18	1/36	0	-1	+1

at the lattice nodes. In the LBM, the macroscopic variables of interest can be derived by calculating the moments of the population distribution functions $f_i(\mathbf{x}, t)$. The density $\rho(\mathbf{x}, t)$ and velocity $\mathbf{u}(\mathbf{x}, t)$ are respectively the zeroth and first moments of the population distribution functions. Their expressions are given by

$$\rho(\mathbf{x}, t) = \sum_i f_i(\mathbf{x}, t)\,, \tag{3.3}$$

$$\rho\mathbf{u}(\mathbf{x}, t) = \sum_i \mathbf{c}_i f_i(\mathbf{x}, t)\,. \tag{3.4}$$

3.2.2 Algorithm

The general LBM algorithm is divided into two successive parts: *collision* or relaxation and *streaming* or propagation.

Collision. The first part of the algorithm is the collision step. It is a local operation performed on the lattice node that determines the post-collision distribution function

$f_i^\star$ as follows

$$f_i^\star(\mathbf{x}, t) = f_i(\mathbf{x}, t) + \Omega_i(\mathbf{x}, t)\,. \tag{3.5}$$

Streaming. After collision, the resulting post-collision distribution function $f_i^\star$ is streamed to neighbouring lattice nodes according to

$$f_i(\mathbf{x} + \mathbf{c}_i\Delta t, t + \Delta t) = f_i^\star(\mathbf{x}, t)\,. \tag{3.6}$$

A basic LBM algorithm consists of the following steps

1. Initialise the distribution functions as $f_i^{\mathrm{eq}}(\mathbf{x}, 0) = f_i^{\mathrm{eq}}(\rho(\mathbf{x}, 0), \mathbf{u}(\mathbf{x}, 0))$
2. Compute the macroscopic moments $\rho(\mathbf{x}, t)$ and $\mathbf{u}(\mathbf{x}, t)$
3. Calculate the equilibrium distribution functions $f_i^{\mathrm{eq}}(\mathbf{x}, t)$
4. Start time iterations
    - 4.1. Perform the collision step
    - 4.2. Perform the streaming step
    - 4.3. Apply the boundary conditions
5. Repeat the previous steps increasing the time step until convergence

3.2.3 Collision Operators

The most challenging part of the LBE formulation is modelling the complex collision operator Ω_i. The choice of collision model and relaxation rate directly affects the accuracy and the stability of the numerical scheme as well as the computational time [125, 126]. The most commonly used models are the Bhatnakar-Gross-Krook (BGK), the multiple-relaxation-time (MRT) and the two-relaxation-time (TRT) collision operators [48, 125].

BGK Collision Operator

The most straightforward approach to model Ω_i is the linear BGK collision operator, which can be expressed as [44, 93, 124, 127]

$$\Omega_i(f) = -\frac{f_i(\mathbf{x},t) - f_i^{\mathrm{eq}}(\mathbf{x},t)}{\tau}\Delta t\,, \tag{3.7}$$

where τ is a time constant defined as *relaxation time*. The BGK operator models the evolution of the distribution function f towards the equilibrium distribution function f^{eq}. The relaxation time τ is the parameter that controls the rate at which the distribution function relaxes towards equilibrium, and its value determines transport coefficients such as viscosity. Through the Chapman-Enskog analysis, the relaxation time τ is related to the macroscopic kinematic shear viscosity ν by

$$\nu = c_s^2\left(\tau - \frac{\Delta t}{2}\right). \tag{3.8}$$

The kinematic bulk viscosity ν_B is defined as

$$\nu_B = \frac{2\nu}{3}. \tag{3.9}$$

The simplicity and efficiency of the BGK formulation entail reduced stability for problems involving small viscosities, large velocity magnitudes and high values of the Reynolds number. Since the accuracy of the BGK operator is related to the relaxation time, the numerical solution is not viscosity-independent [125, 128].

MRT Collision Operator

Due to the inherent limitations of the BGK model, more advanced collision operators are considered to achieve better simulation results [39, 129]. The MRT collision operator addresses this requirement by performing the relaxation to equilibrium in moment space and assigning individual relaxation rates to different moments of the distribution function [48, 130]. By providing enhanced control over the relaxation rates, the MRT model improves both numerical stability and accuracy, allowing for the simulation of a

much broader range of problems [2, 131].

The MRT collision operator performs relaxation in moment space rather than in the distribution function space, as seen with the BGK model. To enable this, moments are determined from distribution functions by means of a linear transformation to moment space. The moments m_k of the distribution function f_i in a DdQq velocity set can be calculated as follows

$$m_k = \sum_{i=0}^{q-1} M_{ki} f_i \,, \qquad \text{for } k = 0, ..., q-1 \tag{3.10}$$

where M_{ki} is an element of the transformation matrix $\mathbf{M}$. Thus, the linear transformation from population space to moment space is expressed as

$$\mathbf{m} = \mathbf{M}\mathbf{f} \,, \tag{3.11}$$

where $\mathbf{m}$ is the row vector of moments m_k, and $\mathbf{f}$ is the vector of distribution functions f_i. The equilibrium distribution function f_i^{eq} can be mapped in moment space to determine the equilibrium moment vectors m_k^{eq} in the following way

$$\mathbf{m}^{\text{eq}} = \mathbf{M}\mathbf{f}^{\text{eq}} \,. \tag{3.12}$$

Then, the collision step acts in moment space by relaxing each moment towards its equilibrium value with an independent rate. This can be achieved by introducing a diagonal relaxation matrix Λ

$$\Lambda = \text{diag}\left(\omega_0, \omega_1, ..., \omega_{q-1}, \right) \,, \tag{3.13}$$

where each diagonal element corresponds to the individual relaxation rate for each moment.

In the general MRT algorithm, the conserved moments are computed from the pre-collision populations and the moments $\mathbf{m}$ and $\mathbf{m}^{\text{eq}}$ are determined using Equation 3.11 and 3.12, respectively. The collision step is performed in moment space, and the relaxed

moments are then transformed back to population space, where the streaming step is performed. The MRT algorithm can be expressed as

$$\mathbf{f}(\mathbf{x}+\mathbf{c}_i\Delta t, t+\Delta t) - \mathbf{f}(\mathbf{x},t) = -\mathbf{M}^{-1}\Lambda\mathbf{M}\left[\mathbf{f}(\mathbf{x},t) - \mathbf{f}^{\mathrm{eq}}(\mathbf{x},t)\right]\Delta t\,. \tag{3.14}$$

Considering the D2Q9 velocity set, the moments of the distribution function f_i are defined as follows

$$m_{pq} = \sum_{i=0}^{8} c_{ix}^{p} c_{iy}^{q} f_i\,, \qquad \text{for } p,q = 0,1,2 \tag{3.15}$$

where p and q are integers corresponding to the moment order. The velocity monomials c_{ix} and c_{iy} are used to determine nine linearly independent basis vectors. The moments are constructed in such a way as to satisfy the conservation laws for density and momentum. This representation allows to incorporate macroscopic physics since moments correspond to hydrodynamic quantities [131]. The moment vector $\mathbf{m}$ can be expressed as

$$\mathbf{m} = (\rho, e, \epsilon, j_x, q_x, j_y, q_y, p_{xx}, p_{xy},)\ , \tag{3.16}$$

where ρ is the density, e is the energy, ϵ is related to the energy squared, j_x and j_y are the components of the momentum flux, q_x and q_y are the components of the energy flux, and p_{xx} and p_{xy} correspond to the diagonal and off-diagonal components of the stress tensor, respectively. The moments are constructed to be mutually orthogonal, and the corresponding transformation matrix $\mathbf{M}$ is defined as

$$\mathbf{M} = \begin{pmatrix} 1 & 1 & 1 & 1 & 1 & 1 & 1 & 1 & 1 \\ -4 & -1 & -1 & -1 & -1 & 2 & 2 & 2 & 2 \\ 4 & 2 & 2 & 2 & 2 & -1 & -1 & -1 & -1 \\ 0 & 1 & 0 & -1 & 0 & 1 & -1 & -1 & 1 \\ 0 & -2 & 0 & 2 & 0 & 1 & -1 & -1 & 1 \\ 0 & 0 & 1 & 0 & -1 & 1 & -1 & -1 & 1 \\ 0 & 0 & -2 & 0 & 2 & 1 & -1 & -1 & 1 \\ 0 & 1 & -1 & 1 & -1 & 0 & 0 & 0 & 0 \\ 0 & 0 & 0 & 0 & 0 & 1 & -1 & 1 & -1 \end{pmatrix} \tag{3.17}$$

It should be noted that the rows of $\mathbf{M}$ are organised by ascending tensor order [131]. The quantities ρ, e, and ϵ are zeroth-order tensors and they represent the zeroth, second, and fourth-order moments of f_i, respectively. The first-order tensors j_x, j_y and q_x, q_y are first-order moments and third-order moments, respectively. The components p_{xx} and p_{xy} represent the second-order stress tensor, and they are second-order moments of f_i.

The orthogonality properties of the moments m_k guarantee that they are uniquely defined and they can be relaxed independently. This methodology allows the control of hydrodynamic quantities by choosing the corresponding relaxation parameters ω individually [131]. Thus, the MRT operator allows tuning shear ν and bulk ν_B viscosity independently to increase the stability of numerical simulations [56]. In the MRT model for the D2Q9 velocity set, nine collision parameters are available ω_0, ω_1, ω_2, ω_3, ω_4, ω_5, ω_6, ω_7 and ω_8. The relaxation rates for macroscopic density and momentum vector (ω_0, ω_3, ω_5) have no effect because they are associated with conserved moments. Therefore, their value can be chosen arbitrarily and it is usually set to zero. The relaxation rates ω_2, ω_4 and ω_6 are associated with higher-order kinetic moments and they can be used as adjustable parameters to increase the simulation performance. To satisfy isotropy considerations, the same value is chosen for the relaxation rates ω_4 and ω_6. The three remaining relaxation rates, ω_7, ω_8 and ω_1, are related respectively to the kinematic shear viscosity ν and the kinematic bulk viscosity ν_B by

$$\nu = c_s^2 \left(\frac{1}{\omega_7} - \frac{1}{2} \right) = c_s^2 \left(\frac{1}{\omega_8} - \frac{1}{2} \right) = c_s^2 \left(\frac{1}{\omega_\nu} - \frac{1}{2} \right) , \tag{3.18}$$

$$\nu_B = c_s^2 \left(\frac{1}{\omega_1} - \frac{1}{2} \right) - \frac{\nu}{3} = c_s^2 \left(\frac{1}{\omega_\chi} - \frac{1}{2} \right) - \frac{\nu}{3} , \tag{3.19}$$

where the relaxation time is defined as $\tau = 1/\omega_\nu$. Therefore, the relaxation matrix Λ assumes the diagonal form

$$\Lambda = \mathrm{diag}\left(0, \omega_\chi, \omega_2, 0, \omega_4, 0, \omega_4, \omega_\nu, \omega_\nu\right) . \tag{3.20}$$

TRT Collision Operator

A significant disadvantage associated with the MRT formulation is that tuning the relaxation rates of individual moments can only be achieved through a cumbersome parameter analysis. The TRT collision operator is a simplification of the MRT that requires only two relaxation parameters [2,132]. In the TRT model, populations f_i and equilibrium populations f_i^{eq} are decomposed into symmetric and antisymmetric parts. The symmetric part is then relaxed with a rate ω^+ and the antisymmetric one with a ω^- relaxation parameter [133]. The general TRT algorithm is given by the following equation

$$f_i(\mathbf{x}+\mathbf{c}_i\Delta t, t+\Delta t) = f_i(\mathbf{x},t) - \omega^+\Delta t\left(f_i^+ - f_i^{eq+}\right) - \omega^-\Delta t\left(f_i^- - f_i^{eq-}\right). \quad (3.21)$$

In the TRT model the kinematic shear viscosity ν is defined as

$$\nu = c_s^2\left(\frac{1}{\omega^+\Delta t} - \frac{1}{2}\right). \quad (3.22)$$

The stability properties of the TRT model are controlled by a combination of the relaxation rates ω^+ and ω^-, defined as the *magic parameter* Υ

$$\Upsilon = \left(\frac{1}{\omega^+\Delta t} - \frac{1}{2}\right)\left(\frac{1}{\omega^-\Delta t} - \frac{1}{2}\right). \quad (3.23)$$

Thus, while the relaxation parameter ω^+ can be used to control the shear viscosity value, the magic parameter Υ can be freely tuned to improve accuracy and stability. Unlike the MRT model, the bulk viscosity cannot be chosen independently from the shear viscosity and the accuracy error shows a dependency on the chosen relaxation time. Due to the symmetric structure of the TRT operator, the collision step can be performed just for one half of the velocity set. In such a manner, the TRT implementation is as efficient as BGK [48].

Central Moment Collision Operator

It has been demonstrated that the methodology used to construct the previous collision models violates Galilean invariance [134–137]. This property ensures that the description of physical phenomena implemented in a numerical scheme is independent of any inertial frame of reference. The cascaded lattice Boltzmann method (CLBM) formulated by Greier et al. [134] recovers Galilean invariance and improves numerical stability [134,135]. In the CLBM, collisions are performed in moment space using the central moments of the distribution function, which are obtained in a frame of reference moving with the macroscopic fluid velocity [134]. The collision operator is represented as a cascaded process in which the effect of collision influences successive moments in ascending order [135]. The CLBM collision operator can be modelled as $\Omega_i = (\mathbf{K} \cdot \mathbf{k})_i$ where $\mathbf{k}$ is the collision kernel and $\mathbf{K}$ is an orthogonal transformation matrix [138,139]. Similarly to the MRT collision operator, CLBM defines nine linearly independent moment basis vectors for the D2Q9 velocity set. The corresponding orthogonal transformation matrix $\mathbf{K}$ is expressed as follows

$$\mathbf{K} = \begin{pmatrix} 1 & 0 & 0 & -4 & 0 & 0 & 0 & 0 & 4 \\ 1 & 1 & 0 & -1 & 1 & 0 & 0 & 2 & -2 \\ 1 & 0 & 1 & -1 & -1 & 0 & 2 & 0 & -2 \\ 1 & -1 & 0 & -1 & 1 & 0 & 0 & -2 & -2 \\ 1 & 0 & -1 & -1 & -1 & 0 & -2 & 0 & -2 \\ 1 & 1 & 1 & 2 & 0 & 1 & -1 & -1 & 1 \\ 1 & -1 & 1 & 2 & 0 & -1 & -1 & 1 & 1 \\ 1 & -1 & -1 & 2 & 0 & 1 & 1 & 1 & 1 \\ 1 & 1 & -1 & 2 & 0 & -1 & 1 & -1 & 1 \end{pmatrix} \tag{3.24}$$

The discrete central moments of the distribution function can be obtained by shifting the frame of reference by the macroscopic fluid velocity. Considering Equation 3.15,

central moments $\hat{\kappa}_{pq}$ of different order pq are defined as

$$\hat{\kappa}_{pq} = \sum_{i=0}^{8} (c_{ix} - u_x)^p \, (c_{iy} - u_y)^q \, f_i \,, \qquad \text{for } p, q = 0, 1, 2 \tag{3.25}$$

where u_x and u_y are the components of the macroscopic velocity in x and y direction, respectively. The central moment vector $\hat{\kappa}$ can be expressed as

$$\hat{\kappa} = (\hat{\kappa}_0, \hat{\kappa}_x, \hat{\kappa}_y, \hat{\kappa}_{xx}, \hat{\kappa}_{yy}, \hat{\kappa}_{xy}, \hat{\kappa}_{xxy}, \hat{\kappa}_{xyy}, \hat{\kappa}_{xxyy}) \,. \tag{3.26}$$

In order to achieve Galilean invariance, the central moments of the equilibrium distribution function $\hat{\kappa}^{\mathrm{eq}}$ are constructed to be equal to the corresponding continuous moments expressed by Equation 2.11–2.13. Therefore, the central moments of different order for the equilibrium distribution functions f^{eq} are assigned the following values

$$\hat{\kappa}^{\mathrm{eq}} = \left(\rho, 0, 0, c_{\mathrm{s}}^2 \rho, c_{\mathrm{s}}^2 \rho, 0, 0, 0, c_{\mathrm{s}}^4 \rho\right) \,. \tag{3.27}$$

Central moments can be expressed as polynomials of moments in the rest frame of reference, i.e. raw moments up to the same order. The corresponding raw moments κ in the rest frame of reference are defined as follows

$$\begin{aligned}
\kappa_0 &= \rho \,, \\
\kappa_x &= \rho u_x \,, \\
\kappa_y &= \rho u_y \,, \\
\kappa_{xx} &= f_1 + f_3 + f_5 + f_6 + f_7 + f_8 \,, \\
\kappa_{yy} &= f_2 + f_4 + f_5 + f_6 + f_7 + f_8 \,, \\
\kappa_{xy} &= f_5 + f_7 - f_6 + f_8 \,, \\
\kappa_{xxy} &= f_5 + f_6 - f_7 + f_8 \,, \\
\kappa_{xyy} &= f_5 + f_8 - f_6 + f_7 \,, \\
\kappa_{xxyy} &= f_5 + f_6 + f_7 + f_8 \,.
\end{aligned} \tag{3.28}$$

Collision invariance of conserved moments yields $k_0 = k_1 = k_2 = 0$. The complete collision kernel can be obtained starting from the lowest order central moments that are not collision invariant by solving for the deviation of the raw moments from their equilibrium values. These expressions are then modified to allow for a relaxation process during collision by introducing the corresponding relaxation parameters ω_i. The final expressions of the non-conserved collision kernel vectors k_i are as follows

$$
\begin{aligned}
k_3 =& \frac{\omega_3}{12}\left[2c_s^2\rho + \rho\left(u_x^2+u_y^2\right) - \left(\kappa_{xx}+\kappa_{yy}\right)\right] ,\\
k_4 =& \frac{\omega_4}{4}\left[\rho\left(u_x^2-u_y^2\right) - \left(\kappa_{xx}-\kappa_{yy}\right)\right] ,\\
k_5 =& \frac{\omega_5}{4}\left[\rho u_x u_y - \kappa_{xy}\right] ,\\
k_6 =& \frac{\omega_6}{4}\left[2\rho u_x^2 u_y + \kappa_{xxy} - 2u_x\kappa_{xy} - u_y\kappa_{xx}\right] - \frac{1}{2}u_y\left(3k_3+k_4\right) - 2u_x k_5 ,\\
k_7 =& \frac{\omega_7}{4}\left[2\rho u_x u_y^2 + \kappa_{xyy} - 2u_y\kappa_{xy} - u_x\kappa_{yy}\right] - \frac{1}{2}u_x\left(3k_3-k_4\right) - 2u_y k_5 ,\\
k_8 =& \frac{\omega_8}{4}\left\{c_s^4\rho + 3\rho u_x^2 u_y^2 - \left[\kappa_{xxyy} - 2u_x\kappa_{xyy} - 2u_y\kappa_{xxy} + u_x^2\kappa_{yy} + u_y^2\kappa_{xx} + 4u_x u_y\kappa_{xy}\right]\right\}\\
& - 2k_3 - \frac{1}{2}u_y^2\left(3k_3+k_4\right) - \frac{1}{2}u_x^2\left(3k_3-k_4\right) - 4u_x u_y k_5 - 2u_y k_6 - 2u_x k_7 .
\end{aligned}
\tag{3.29}
$$

The central moments are relaxed in ascending order with individual relaxation rates ω_i [138–140]. To achieve an isotropic viscous stress tensor, it is required that $\omega_4 = \omega_5 = \omega_\nu$, where ω_ν determines the kinematic shear viscosity [139] as shown in Equation 3.8. The relaxation parameter ω_3 is related to the bulk viscosity ν_B as given in Equation 3.9. All the other relaxation parameters are set to unity to improve numerical stability [139]. The relaxation matrix Λ is given as follows

$$
\Lambda = \mathrm{diag}\left(1,1,1,\omega_\chi,\omega_\nu,\omega_\nu,1,1,1\right) . \tag{3.30}
$$

3.2.4 Boundary Conditions

In the LBM, boundary conditions are applied to the distribution functions f_i rather then to macroscopic quantities [56]. Since the system of mesoscopic variables has more degrees of freedom than the corresponding macroscopic formulation, the implementation of boundary conditions generally proves to be a challenging aspect.

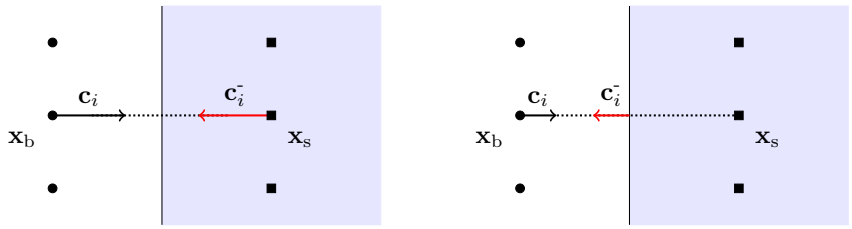
The boundary conditions are prescribed at boundary nodes $\mathbf{x}_\mathrm{b}$, which indicate lattice sites at the interface between the fluid and solid domain connected to at least one solid and one fluid node. The different LBM boundary schemes can be broadly classified as *link-wise* and *wet-nodes* approaches [48]. Link-wise boundary conditions set the boundary location on lattice links approximately midway between lattice nodes. The most commonly used link-wise scheme is the *bounce-back* method. Wet-node boundary schemes place the boundary exactly on a boundary node. In this case, the distribution functions f_i at boundary nodes can be reconstructed using information from the macroscopic conditions. The most popular wet-node approach is the *equilibrium scheme*.

In case of a rarefied gas, a *diffuse* boundary condition can be defined. However, a low-order scheme is not able to capture the flow field accurately for a high or moderate Knudsen number [56]. The most common boundary condition implementations for the LBE are addressed in the following.

Bounce-Back Boundary Conditions

In the LBM, the most popular way to model the no-slip velocity boundary condition at stationary walls is the bounce-back scheme [2, 44, 141, 142]. This strategy assumes that all the populations hitting a wall during propagation are immediately reflected in the opposite direction. This condition ensures that there is no flux across the boundary and that there is no relative transverse motion between fluid and boundary. The bounce-back scheme can be implemented using two different strategies, namely the fullway and halfway schemes [48, 56, 143].

Fullway Bounce-Back. Populations propagate from the boundary to the solid node, where their velocity is inverted in the following collision step. Therefore, this scheme only changes the collision step and implements the usual streaming step. The fullway bounce-back method requires additional solid nodes to store the population before the collision step. This method is a first-order approximation of the boundary condition, so the error is proportional to the lattice spacing. Since the fullway bounce-back only uses distribution functions at the wall lattice node, this scheme is completely local.



(a) *Fullway Bounce-Back* (b) *Halfway Bounce-Back*

Figure 3.2: Schematics of bounce-back boundary conditions. (a) Fullway: populations propagate to the solid node $\mathbf{x}_\mathrm{s}$ and are reflected after collision. (b) Halfway: reflection occurs at the midpoint between the boundary node $\mathbf{x}_\mathrm{b}$ and the solid node $\mathbf{x}_\mathrm{s}$ during propagation. The arrows indicate the direction $\mathbf{c}_i$ and the shaded region represents the solid domain.

Halfway Bounce-Back. Populations propagate only through half of the distance between the boundary and the solid node. In this case, the velocity of the particles is inverted during the streaming step, so that the collision step remains unchanged. In the case of a stationary wall, the streaming step is changed to

$$f_i^-(\mathbf{x}_\mathrm{b}, t + \Delta t) = f_i^\star(\mathbf{x}_\mathrm{b}, t)\,. \tag{3.31}$$

According to this implementation, populations leaving the boundary node $\mathbf{x}_\mathrm{b}$ at time t are reflected back at the wall at time $t + \Delta t/2$ with an opposite velocity and then at time $t + \Delta t$ they arrive again at the node $\mathbf{x}_\mathrm{b}$. The halfway bounce-back method is a second-order approximation of the boundary condition, but it is weakly non-local since it uses distribution functions from neighbouring nodes [128].

The implementation of the fullway and halfway bounce-back boundary conditions is schematised in Figure 3.2. The bounce-back scheme owes its popularity to the simplicity of implementation and the exact conservation of mass at stationary boundaries [141]. A drawback to the bounce-back rule is that second-order accuracy can only be achieved if the wall is aligned with the lattice and cuts halfway through the lattice links [2, 128]. Therefore, the implementation of this scheme for complex geometries generally leads to different sources of error. Arbitrary surfaces are modelled by implementing a *staircase* approximation of the boundary [39]. This approximation results in a geometrical

discretisation error that reduces the numerical accuracy.

Furthermore, when the bounce-back scheme is used in combination with the BGK model, the exact location of the no-slip boundary depends on the specific choice of the relaxation rate τ. This effect is often called *numerical boundary slip* and it leads to an unphysical viscosity-dependent slip velocity [128, 144]. The related error decreases as a function of grid resolution and relaxation times [39]. The slip velocity is anisotropic with respect to the underlying lattice structure because it depends on the inclination of the boundary. Thus, the effective shape and location of the wall do not correspond to the expected boundary [48].

Periodic Boundary Conditions

Periodic boundary conditions can be used when the flow is described by a symmetrical pattern and the flow solution is periodic [39, 141]. They are defined as a boundary connected to another boundary on the opposite side, so that particles leaving the domain instantaneously re-enter at the connected boundary to ensure mass and momentum conservation.

The periodic boundary conditions are implemented by assigning the value of the post-collision populations leaving on one side to the post-streaming populations entering the domain on the opposite side

$$f_i(\mathbf{x}, t + \Delta t) = f_i^\star(\mathbf{x} + \mathbf{L} - \mathbf{c}_i \Delta t, t)\,, \tag{3.32}$$

where $\mathbf{L}$ represents the direction and length of the periodic system. Periodic boundary conditions can also be implemented during the streaming step by setting the value of the unknown incoming populations $f_i^\star$ equal to the one of those leaving the domain at the opposite side

$$f_i^\star(\mathbf{x}, t) = f_i^\star(\mathbf{x} + \mathbf{L}, t)\,. \tag{3.33}$$

Velocity and Pressure Boundary Conditions

The most common boundary condition for velocity and pressure at planar boundaries is given by Zou and He [145]. The unknown discrete velocity is determined by applying the bounce-back rule to the non-equilibrium distribution functions. Considering the D2Q9 velocity set and a top edge with velocity $\mathbf{u}_\mathrm{w} = (u_\mathrm{w}, v_\mathrm{w})$, the wall density ρ_w and distribution functions for the boundary node $\mathbf{x}_\mathrm{b}$ are calculated as follows

$$\rho_\mathrm{w} = \frac{f_0 + f_2 + f_6 + 2(f_1 + f_7 + f_8)}{1 + v_\mathrm{w}}\,, \tag{3.34a}$$

$$f_4 = f_8 - \frac{2\,\rho_\mathrm{w}\,v_\mathrm{w}}{3}\,, \tag{3.34b}$$

$$f_3 = f_7 + \frac{1}{2}\,(f_6 - f_2) - \frac{1}{2}\rho_\mathrm{w}\,u_\mathrm{w} - \frac{1}{6}\rho_\mathrm{w}\,v_\mathrm{w}\,, \tag{3.34c}$$

$$f_5 = f_1 + \frac{1}{2}\,(f_6 - f_2) - \frac{1}{2}\rho_\mathrm{w}\,u_\mathrm{w} - \frac{1}{6}\rho_\mathrm{w}\,v_\mathrm{w}\,. \tag{3.34d}$$

This method cannot be applied to concave corners because the system of equations is underdetermined. In that case, this approach requires both density and velocity to be specified to remove an unknown. If the velocity boundary condition is constant, the density value can be set equal to that of a neighbouring fluid node, while the velocity is set to zero for constant density boundaries. For a moving wall, the bounce-back scheme can be used with an additional source term [39].

3.2.5 Forcing Schemes

To incorporate the effect of an external force field $\mathbf{F} = (F_x, F_y)$, the general LBE given by Equation 3.2 is modified as follows

$$f_i(\mathbf{x} + \mathbf{c}_i\,\Delta t, t + \Delta t) = f_i(\mathbf{x}, t) + \Omega_i(\mathbf{x}, t)\Delta t + S_i(\mathbf{x}, t)\Delta t\,, \tag{3.35}$$

where the discrete source term S_i represents the influence of the force field in the velocity space. The macroscopic body force is implemented using a split-forcing approach [46,

146]. The expression of the fluid velocity given by Equation 3.4 is redefined as follows

$$\rho \mathbf{u}(\mathbf{x}, t) = \sum_i \mathbf{c}_i f_i(\mathbf{x}, t) + \frac{\mathbf{F}\Delta t}{2\rho} \,. \tag{3.36}$$

Considering the CLBM approach [134], the central moments of the source term $\hat{\sigma}$ can be defined as

$$\hat{\sigma}_{pq} = \sum_{i=0}^{8} (c_{ix} - u_x)^p \, (c_{iy} - u_y)^q \, S_i \,, \qquad \text{for } p, q = 0, 1, 2 \,. \tag{3.37}$$

The central moment vector $\hat{\sigma}$ can be expressed as

$$\hat{\sigma} = (\hat{\sigma}_0, \hat{\sigma}_x, \hat{\sigma}_y, \hat{\sigma}_{xx}, \hat{\sigma}_{yy}, \hat{\sigma}_{xy}, \hat{\sigma}_{xxy}, \hat{\sigma}_{xyy}, \hat{\sigma}_{xxyy}) \,. \tag{3.38}$$

The discrete central moments of the source term are constructed to coincide with their corresponding continuous central moments, ensuring Galilean invariance [139,147]. Their explicit expressions are then given by

$$\hat{\sigma} = \left(0, F_x, F_y, 0, 0, 0, c_s^2 F_y, c_s^2 F_x, 0\right) \,. \tag{3.39}$$

The raw moments of the source term σ, defined in the rest frame of reference, are computed from the central moments and subsequently expressed in velocity space as

$$\begin{aligned}
\sigma_0 &= 0\,, \\
\sigma_1 &= F_x\,, \\
\sigma_2 &= F_y\,, \\
\sigma_3 &= 6\left(F_x u_x + F_y u_y\right)\,, \\
\sigma_4 &= 4\left(F_x u_x + F_y u_y\right)\,, \\
\sigma_5 &= \left(F_x u_y + F_y u_x\right)\,, \\
\sigma_6 &= \left(2 - 3{u_x}^2\right) F_y - 6 F_x u_x u_y\,, \\
\sigma_7 &= \left(2 - 3{u_y}^2\right) F_x - 6 F_y u_y u_x\,, \\
\sigma_8 &= 6\left[\left(3{u_y}^2 - 2\right) F_x u_x + \left(3{u_x}^2 - 2\right) F_y u_y\right]\,.
\end{aligned} \tag{3.40}$$

Finally, the explicit expressions for the source terms S_i are obtained from the raw moments in velocity space σ by inverting the orthogonal transformation matrix $\mathbf{K}$ given by Equation 3.24.

3.2.6 Moving Bounce-Back Method

One of the most effective implementations of the bounce-back method for moving geometries was first proposed by Ladd to study rigid moving particles [143]. In this algorithm, particles are filled with fluid in order to avoid the destruction and recreation of fluid nodes for moving geometries. This numerical method can be schematised as

1. Identify lattice nodes located inside of a particle $\mathbf{x}_\mathrm{s}$, the exterior fluid nodes and the boundary nodes $\mathbf{x}_\mathrm{b}$.

2. Identify all lattice links $\mathbf{c}_i$ connecting boundary and solid nodes, intersecting the boundary at the wall location $\mathbf{x}_\mathrm{w}$

3. Compute the wall velocity $\mathbf{u}_\mathrm{w}$ at each link $\mathbf{x}_\mathrm{w}$ considering rigid translation and rotation

$$\mathbf{u}_\mathrm{w} = \mathbf{U} + \boldsymbol{\Theta} \times \left(\mathbf{x}_\mathrm{w} - \mathbf{X}\right)\,, \tag{3.41}$$

where $\mathbf{U}$, $\boldsymbol{\Theta}$ and $\mathbf{X}$ are respectively the particle's linear velocity, angular velocity and centre of mass.

4. Perform collision on all nodes.

5. Perform propagation.

   5.1. Populations streaming on a boundary link from a boundary node $\mathbf{x}_\mathrm{b}$ to a solid node $\mathbf{x}_\mathrm{s}$ are bounced back halfway to the solid node at the wall $\mathbf{x}_\mathrm{w}$

$$f_i^-(\mathbf{x}_\mathrm{b}, t+\Delta t) = f_i^\star(\mathbf{x}_\mathrm{b}, t) - 2\, w_i\, \rho\, \frac{\mathbf{u}_\mathrm{w}\cdot\mathbf{c}_i}{c_s^2}\,. \tag{3.42}$$

   5.2. Populations moving from a solid node $\mathbf{x}_\mathrm{s}$ to a boundary node $\mathbf{x}_\mathrm{b}$ are reflected according to

$$f_i(\mathbf{x}_\mathrm{s}, t+\Delta t) = f_{i^-}^\star(\mathbf{x}_\mathrm{s}, t) + 2\, w_i\, \rho\, \frac{\mathbf{u}_\mathrm{w}\cdot\mathbf{c}_i}{c_s^2}\,. \tag{3.43}$$

6. Calculate the total momentum and angular momentum exchange between the fluid and the solid.

7. Update the population properties.

8. Update the list of lattice nodes and links for the next time step.

The principle of the moving bounce-back method is illustrated in Figure 3.3, showing the classification of lattice nodes and the treatment of cut links at the particle boundary.

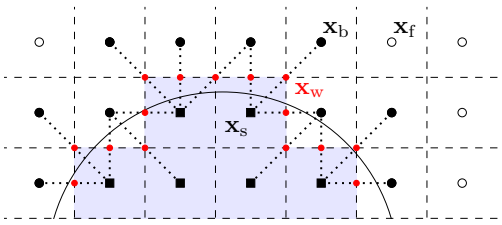


Figure 3.3: Schematics of the moving bounce-back method. Fluid nodes $\mathbf{x}_\mathrm{f}$ (open circles), boundary nodes $\mathbf{x}_\mathrm{b}$ (black circles), wall nodes $\mathbf{x}_\mathrm{w}$ (red circles), and solid nodes $\mathbf{x}_\mathrm{s}$ (black squares) are identified. Wall nodes are located at the midpoint of lattice links $\mathbf{c}_i$ connecting a boundary node to a solid node.

3.2.7 Interpolated Bounce-Back Method

The interpolated bounce-back (IBB) method implements an interpolation scheme to reduce the modelling error for curved and inclined boundaries [148]. One of the most popular IBB approaches for curved boundaries was proposed by Bouzidi [149]. This method considers three different types of lattice nodes: boundary nodes $\mathbf{x}_\mathrm{b}$, solid nodes $\mathbf{x}_\mathrm{s} = \mathbf{x}_\mathrm{b} + \mathbf{c}_i\,\Delta t$ and fluid nodes $\mathbf{x}_\mathrm{f} = \mathbf{x}_\mathrm{b} - \mathbf{c}_i\,\Delta t$. Boundary links intersects the wall at a distance $d_\mathrm{b} \in [0, |\mathbf{c}_i|\,\Delta t]$ from the boundary node $\mathbf{x}_\mathrm{b}$. This method introduces additional information about the wall location by defining the *reduced wall location* as

$$q = \frac{d_\mathrm{b}}{\mathbf{c}_i\,\Delta t} \quad \in [0, 1]\ . \tag{3.44}$$

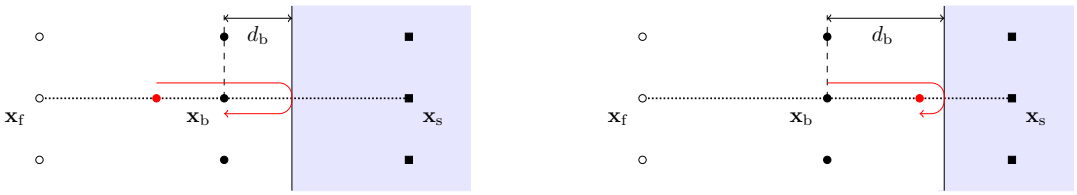
Assuming that any population f_i moves a distance $\mathbf{c}_i\,\Delta t$ during propagation from the boundary node $\mathbf{x}_\mathrm{b}$, there are two different cases

a. If the wall is located halfway between lattice nodes, then $q = 1/2$, and the scheme corresponds to the simple bounce-back method. The population f_i propagates a distance $\mathbf{c}_i\,\Delta t/2$ from the original boundary node to the wall and then it is reflected another distance $\mathbf{c}_i\,\Delta t/2$ to the boundary node.

b. If the wall is not located halfway between lattice nodes $q \neq 1/2$, the population f_i cannot reach another lattice node. In this case, the post-collision distribution function is constructed such that f_i reaches a lattice node by implementing an interpolation scheme. The unknown bounced back population $f_i^-(\mathbf{x}_\mathrm{b}, t + \Delta t)$ can be interpolated from the values of the known populations $\mathbf{x}_\mathrm{b}$ and $\mathbf{x}_\mathrm{f}$ in the following way

$$f_i^-(\mathbf{x}_\mathrm{b}, t + \Delta t) = \begin{cases} 2\,q\,f_i^\star(\mathbf{x}_\mathrm{b}, t) + (1 - 2\,q)\,f_i^\star(\mathbf{x}_\mathrm{f}, t) & q < \frac{1}{2}\,, \\ \frac{1}{2\,q}\,f_i^\star(\mathbf{x}_\mathrm{b}, t) + \frac{2\,q-1}{2\,q}\,f_i^\star(\mathbf{x}_\mathrm{b}, t) & q \geq \frac{1}{2}\,. \end{cases} \tag{3.45}$$

Figure 3.4 illustrates how the IBB method accounts for different wall positions relative to the midpoint of a lattice link. The IBB is second-order accurate for arbitrary boundary shapes, and because of its simple implementation, it is an efficient alternative to the



(a) $0 < q < 1/2$ (b) $1/2 \leq q < 1$

Figure 3.4: Schematics of the interpolated bounce-back method: (a) For $q < 1/2$, the bounce-back is performed from an interpolated value (red circle) obtained using the nearest distribution $\mathbf{x}_f$. (b) For $q \geq 1/2$, the population is bounced to an intermediate location (red circle) and then interpolated to the nearest boundary node $\mathbf{x}_b$.

general bounce-back scheme [56]. However, it introduces a viscosity-dependent boundary slip that cannot be easily controlled even with advanced collision operators [93]. Furthermore, due to its non-local implementation and the interpolation, this method is not exactly mass conserving [2].

The IBB algorithm steps can be implemented as

1. Identify boundary nodes $\mathbf{x}_b$, their neighbouring fluid nodes $\mathbf{x}_f$ and solid nodes $\mathbf{x}_s$.
2. Identify boundary links $\mathbf{c}_i$ and their distance d_b from the boundary node $\mathbf{x}_b$.
3. Compute the reduced wall location q for every lattice link.
4. Perform collision on fluid and boundary nodes to calculate $f_i^\star(\mathbf{x}_b, t)$, $f_{i^-}^\star(\mathbf{x}_b, t)$ and $f_i^\star(\mathbf{x}_f, t)$.
5. Perform linear interpolation to construct the unknown populations $f_i^-(\mathbf{x}_b, t+\Delta t)$.
6. Perform propagation.
7. Update the list of lattice links for the next time step.

3.2.8 Partially Saturated Method

The partially saturated method (PSM) presented by Noble and Torczynski [150] is a modified bounce-back approach that provides an alternative strategy to represent complex boundaries. As shown in Figure 3.5, PSM identifies lattice nodes as pure fluid,

pure solid, and partially saturated according to the solid fraction ε of the corresponding lattice cell [150, 151]. The lattice nodes are classified as

- Fluid node $\varepsilon = 0$.
- Mixed node $0 < \varepsilon < 1$.
- Solid node $\varepsilon = 1$.

In this method, the boundary condition is not expressed as an approximation of the wall shape, but rather as an interface condition that separates lattice nodes with different properties. In the PSM algorithm, the standard LBE is modified in the following way

$$f_i(\mathbf{x} + \mathbf{c}_i\,\Delta t,\, t + \Delta t) = f_i(\mathbf{x}, t) + (1 - B)\,\Omega_i^{\mathrm{f}} + B\,\Omega_i^{\mathrm{s}}\,. \tag{3.46}$$

This method features a separate collision operator for fluid nodes Ω_i^{f} and nodes covered partially or fully by a solid Ω_i^{s}. Their expression are respectively

$$\Omega_i^{\mathrm{f}} = \frac{f_i(\mathbf{x}, t) - f_i^{\mathrm{eq}}(\mathbf{x}, t)}{\tau}\,, \tag{3.47a}$$

$$\Omega_i^{\mathrm{s}} = f_i^{-}(\mathbf{x}, t) - f_{i^-}^{\mathrm{eq}}(\rho, \mathbf{u}) - \left(f_i(\mathbf{x}, t) - f_i^{\mathrm{eq}}(\rho, \mathbf{u}_{\mathrm{s}})\right)\,. \tag{3.47b}$$

where $\mathbf{u}$ is the local fluid velocity and $\mathbf{u}_{\mathrm{s}}$ is the velocity of the boundary at point $\mathbf{x}$. It should be noted that Ω_i^{f} is in the same form as the standard BGK collision operator. Collision operators are weighted using a numerical parameter B, defined by

$$B(\varepsilon, \tau) = \frac{\varepsilon\left(\tau - \frac{1}{2}\right)}{(1 - \varepsilon) + \left(\tau - \frac{1}{2}\right)}\,, \tag{3.48}$$

where $B = 0$ for a pure fluid node ($\varepsilon = 0$) and $B = 1$ for a pure solid node ($\varepsilon = 1$). It should be emphasised that $B = 0$ corresponds to the standard BGK equation, $B = 1$ performs a bounce-back of the non-equilibrium part, and $0 < B < 1$ describes a mixed BGK and bounce-back algorithm.

One of the challenges of the PSM is finding correct values for the solid fraction ε, which has to be updated at every time step for moving boundary problems. Since

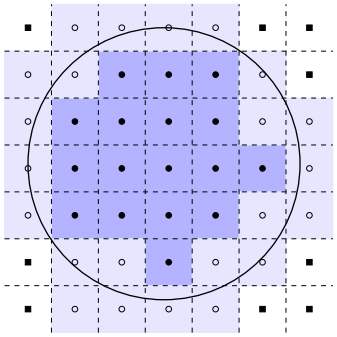


Figure 3.5: Classification of lattice nodes in the partially saturated method: fluid $\varepsilon = 0$ (▪), solid $\varepsilon = 1$ (•) and partially saturated $0 < \varepsilon < 1$ (○).

the PSM fails to capture the exact boundary shape, the no-slip condition is not correctly satisfied at the boundary. The main advantages of the PSM are the absence of interpolations and the exact conservation of mass and momentum.

Within the PSM framework, Tsigginos et al. [152] model solid objects and the surrounding fluid as a two-phase mixture by introducing a virtual fluid with infinite viscosity in place of solid bodies. A momentum exchange algorithm (MES-I) is used to account for the presence of the fluid-solid interface in order to enforce the no-slip condition on the virtual fluid phase velocity. Since the velocity of partially saturated nodes is also dependent on the fluid phase velocity, to improve MES-I, another momentum exchange algorithm (MES-II) is implemented by directly enforcing the solid object velocity on both the virtual fluid phase and partially saturated nodes. This work also derives a second-order accurate scheme for the calculation of the body force, which resolves inaccuracy caused by the weighting parameter B formulation in the original PSM [152].

3.3 Immersed Boundary Methods

The IBM was first introduced by Peskin to study blood flow inside the heart [153–155]. This approach features a non-conforming Eulerian grid and a set of Lagrangian points that represent the solid boundary. The marker points affect the fluid only through an appropriate force field that enforces the no-slip boundary condition. The additional

force term mimics a boundary condition to achieve the desired effects on the fluid. In the original formulation of the IBM [153], the boundary force is introduced to the continuous NSE, which are subsequently appropriately discretised to ensure the no-slip boundary condition. The additional force is evaluated with a *feedback* process based on the deformation of the boundary marker points, which are modelled as elastic springs. However, this method is incapable of modelling perfectly rigid boundaries and it introduces a free parameter that affects the stability and restricts the computational time step [48, 156].

The main advantage provided by the IBM is that the boundary does not have to be reconstructed, and it is not required to compute intersection points. Other important features are the simple implementation and the ability to handle moving boundaries without remeshing procedures.

3.3.1 Mathematical Formulation

Although the original IBM was devised as a numerical method to solve the Navier-Stokes equations, it was later applied to the LBM framework. The IB-LBM was first proposed by Feng and Michaelides [41] and then extended to the MDF method by Suzuki and Inamuro [157]. Boundary conditions in the LBM are usually treated on the population level, and the desired macroscopic properties at the boundary are obtained by appropriate manipulations of the populations $f_i(\mathbf{x}, t)$. However, the original IBM formulation does not take into account the kinetic nature of the LBM, since the boundary condition operates at the macroscopic level.

The IB-LBM features two different node systems that are illustrated in Figure 3.6.

a. The LBM lattice nodes $\mathbf{x}$ define the *Eulerian grid* in the whole domain $\Omega_f \cup \Omega_s$. This is a regular and stationary mesh on which the fluid equations are solved.

b. The marker points $\mathbf{x}_\ell(t)$ represent the surface points of the boundary Γ_s. They are *Lagrangian nodes* that are allowed to move in space.

The main advantage of the IBM formulation is that the arbitrarily complex shape of the boundary is not related to the underlying lattice nodes, and no intersection points

have to be computed. Since the domain is decomposed into two different node systems, it is required to connect the information between them by coupling the dynamics of the boundary and the surrounding fluid.

The no-slip boundary condition ensures that the fluid velocity $\mathbf{u}$ matches the boundary velocity $\mathbf{u}_\ell$ at the Lagrangian marker positions $\mathbf{x}_\ell$, i.e.

$$\mathbf{u}_\ell(t) = \mathbf{u}(\mathbf{x}_\ell, t)\,. \tag{3.49}$$

Considering the Eulerian domain $\Omega_f \cup \Omega_s$, this equation can be alternatively written as follows

$$\mathbf{u}_\ell(t) = \int_{\Omega_f \cup \Omega_s} \mathbf{u}(\mathbf{x}_\ell, t)\, \delta(\mathbf{x} - \mathbf{x}_\ell(t))\, d\mathbf{x}\,, \tag{3.50}$$

where $\delta(\mathbf{x} - \mathbf{x}_\ell(t))$ is the Dirac delta distribution. The force density $\mathbf{F}_{\text{ib}}(\mathbf{x}, t)$ exerted by the boundary surface Γ_s on the nearby fluid can be written as

$$\mathbf{F}_{\text{ib}}(\mathbf{x}, t) = \int_{\Gamma_s} \mathbf{F}_\ell(\mathbf{x}_\ell, t)\, \delta(\mathbf{x} - \mathbf{x}_\ell(t))\, d\mathbf{x}\,, \tag{3.51}$$

where $\mathbf{F}_\ell$ is the force acting on the Lagrangian points. The discretised form of these equations requires the Dirac delta distribution to be replaced with an appropriate discrete function. Assuming that the fluid in the entire volume is homogeneous, the dis-

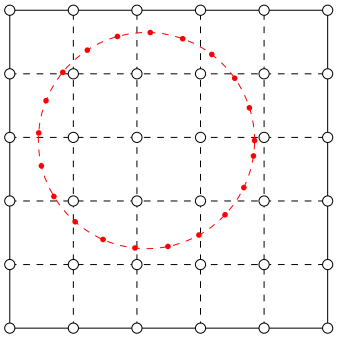


Figure 3.6: Schematics of the fluid Eulerian grid (open circles) and the Lagrangian nodes (solid nodes) in the IBM.

cretised IBM equations are expressed as follows

$$\mathbf{u}(\mathbf{x}_\ell, t) = \sum_{\mathbf{x}} \mathbf{u}(\mathbf{x}, t)\, \Phi(\mathbf{x} - \mathbf{x}_\ell)\, \Delta x^2\,, \tag{3.52}$$

$$\mathbf{F}_{\mathrm{ib}}(\mathbf{x}, t) = \sum_{\mathbf{x}_\ell} \mathbf{F}_\ell(\mathbf{x}_\ell, t)\, \Phi(\mathbf{x} - \mathbf{x}_\ell)\, \Delta s\,, \tag{3.53}$$

where Δs is the spacing between the Lagrangian markers and the interpolation kernel $\Phi(\mathbf{x} - \mathbf{x}_\ell)$ is an appropriate discretised version of the Dirac delta distribution. Equation 3.52 expresses the *velocity interpolation* procedure and Equation 3.53 reflects the *force spreading*. One of the main ideas of the IBM is that there is no direct boundary condition for the fluid, but the immersed boundary affects the surrounding fluid through the forcing term $\mathbf{F}_{\mathrm{ib}}(\mathbf{x}, t)$.

A central element in formulating the interaction between the Lagrangian boundary points and the Eulerian fluid grid is the introduction of a discrete delta function $\Phi(\mathbf{x})$. In multiple dimensions, the discrete delta function is constructed as the product of one-dimensional functions ϕ along each coordinate direction, simplifying its implementation on the Eulerian grid. A normalization factor is introduced such that $\sum_{\mathbf{x}} \Phi(\mathbf{x})\, \Delta\mathbf{x} = 1$. This procedure guarantees that the discrete delta function behaves analogously to the Dirac delta distribution when scaling tends to zero and establishes consistency between the Lagrangian and Eulerian systems [154, 158]. The discrete delta function Φ in 2D is given by

$$\Phi\left(\mathbf{x}\right) = \frac{1}{\Delta x^2}\, \phi\left(\frac{x}{\Delta x}\right) \phi\left(\frac{y}{\Delta x}\right)\,. \tag{3.54}$$

Valid discretised versions of the Dirac delta distribution can be constructed by ensuring that they satisfy the properties indicated by Peskin [154]. The functions corresponding to a two-point ϕ_2, three-point ϕ_3 and four-point ϕ_4 support interval are expressed in

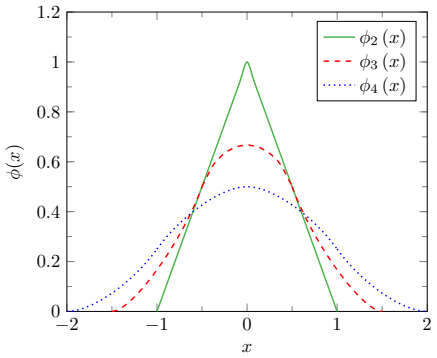


Figure 3.7: Interpolation stencils associated with different discrete delta functions used in the IBM.

the form

$$\phi_2(x) = \begin{cases} 1 - |x| & 0 \le |x| \le \Delta x\,, \\ 0 & \Delta x \le |x|\,, \end{cases} \tag{3.55a}$$

$$\phi_3(x) = \begin{cases} \frac{1}{3}\left(1 + \sqrt{1 - 3x^2}\right) & 0 \le |x| \le \frac{1}{2}\Delta x\,, \\ \frac{1}{6}\left(5 - 3|x| - \sqrt{-2 + 6|x| - 3x^2}\right) & \frac{1}{2}\Delta x \le |x| \le \frac{3}{2}\Delta x\,, \\ 0 & \frac{3}{2}\Delta x \le |x|\,, \end{cases} \tag{3.55b}$$

$$\phi_4(x) = \begin{cases} \frac{1}{8}\left(3 - 2|x| - \sqrt{1 + 4|x| - 4x^2}\right) & 0 \le |x| \le \Delta x\,, \\ \frac{1}{6}\left(5 - 2|x| - \sqrt{-7 + 12|x| - 4x^2}\right) & \Delta x \le |x| \le 2\Delta x\,, \\ 0 & 2\Delta x \le |x|\,. \end{cases} \tag{3.55c}$$

The corresponding interpolation stencils are plotted in Figure 3.7. Based on their interpolation ranges, the function $\phi_4(x)$ leads to a diffuse boundary condition, $\phi_3(x)$ is less smooth, and $\phi_2(x)$ corresponds to the sharpest boundary representation. While the two-point delta function $\phi_2(x)$ is the most efficient in terms of computing time, the four-point delta function $\phi_4(x)$ provides the best numerical stability.

Figure 3.8 graphically shows the interpolation and spreading procedures. To interpolate the lattice velocity at $\mathbf{x}_\ell$, all neighbouring lattice nodes within the grey-shaded area are required. The force density $\mathbf{F}_{\text{ib}}$ at a lattice node $\mathbf{x}$ is computed from the nodes

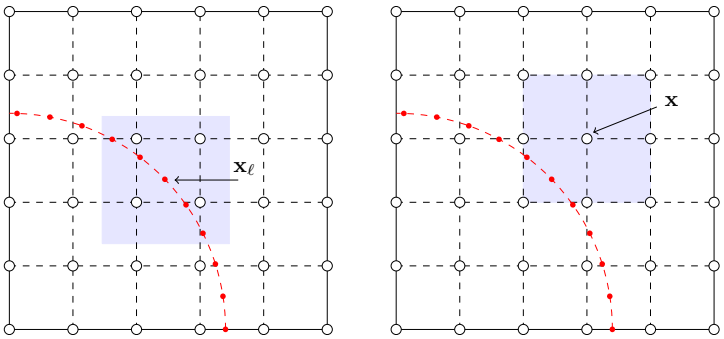
$\mathbf{x}_\ell$ whose interpolation range covers $\mathbf{x}$.

The hydrodynamic force $\mathbf{F}_\mathrm{h}$ and torque $\mathbf{T}_\mathrm{h}$ acting on a solid object are calculated by

$$\mathbf{F}_\mathrm{h}(\mathbf{x},t) = -\sum_{\mathbf{x}_\ell} \mathbf{F}_\ell(\mathbf{x}_\ell,t)\,\Delta s + \mathbf{F}_\mathrm{i}\,, \tag{3.56}$$

$$\mathbf{T}_\mathrm{h}(\mathbf{x},t) = -\sum_{\mathbf{x}_\ell} \mathbf{r}\times\mathbf{F}_\ell(\mathbf{x}_\ell,t)\,\Delta s + \mathbf{T}_\mathrm{i}\,, \tag{3.57}$$

where $\mathbf{F}_\mathrm{i}$ and $\mathbf{T}_\mathrm{i}$ are respectively the force and torque resulting from the internal fluid mass [159], and $\mathbf{r}$ is the position vector of the Lagrangian point with respect to the centre of mass of the solid object.



(a) *Interpolation* (b) *Spreading*

Figure 3.8: Schematics of the interpolation and spreading procedures used to transfer information between the Eulerian fluid grid and the Lagrangian nodes in the IBM.

3.3.2 Force Evaluation Strategies

In general, the strategies for evaluating the boundary force in the IBM have been classified into two categories: the *feedback* approach, introduced in the original IBM formulation [153, 160], and the *direct-forcing* approach [156]. In the explicit feedback-forcing IBM for rigid boundaries [41], the Lagrangian marker points are linked to reference positions that satisfy the rigid-body constraint. Any displacement between the boundary nodes and reference nodes generates a restoring force modelled as a linear spring that acts to recover the prescribed configuration. While this approach is straightforward to implement, it suffers from stability restrictions and introduces parameters that require

problem-dependent tuning [156].

In contrast, direct-forcing methods determine the boundary force directly from the governing equations, without introducing free parameters [156]. This class of methods eliminates the need for user-defined parameters and simplifies the numerical implementation while improving computational efficiency [161]. Direct-forcing IBM can be further categorised into explicit, implicit, and iterative (multi-direct-forcing) formulations. In the explicit direct-forcing approach, the boundary force is computed at the Lagrangian marker points by imposing that the known boundary velocity equals the fluid velocity at that position [107, 162]. Although simple and computationally efficient, the explicit method does not guarantee that the no-slip condition is strictly satisfied for the forcing point velocity [3, 156, 163].

The implicit IBM was introduced by Wu and Shu [164] to improve the accuracy of no-slip condition enforcement at immersed boundaries. In this method, the force density is treated as the unknown and computed such that the interpolated Eulerian velocity exactly matches the prescribed boundary velocity. This formulation leads to a linear system of the form $\mathbf{A}\,\mathbf{X} = \mathbf{B}$, where the vector $\mathbf{X}$ represents the unknown velocity corrections required to achieve the no-slip condition. The solution of this linear system requires inversion of the matrix $\mathbf{A}$, and for moving boundaries, both $\mathbf{A}$ and its inverse must be recomputed at each time step. The implicit method provides higher accuracy and robust enforcement of the no-slip condition compared to explicit approaches, but the increased computational cost can be a significant drawback for problems involving a large number of boundary points or complex moving geometries.

To address these limitations, Wang et al. [163] proposed a multi-direct-forcing immersed boundary method (MDF-IBM), which implements an iterative forcing process until the difference between the interpolated velocity and the prescribed velocity becomes sufficiently small to achieve the no-slip condition at all boundary points [156]. Because the MDF-IBM provides an effective balance between accurate enforcement of the no-slip condition and computational efficiency, it is well-suited for simulating moving rigid boundary problems and is therefore the method adopted in the following.

3.3.3 Multi-Direct-Forcing IBM

The MDF-IBM scheme was originally introduced by Wang et al. [163] to improve the implementation of the no-slip boundary condition in the direct-forcing formulation. They observed that the mutual influence of direct forcing on neighbouring nodes affects the enforcement of the no-slip boundary condition and demonstrated that implementing an iterative process to compute the velocities on the Lagrangian points improves the accuracy and efficiency of the scheme [163].

The no-slip boundary condition expressed by Equation 3.49 is enforced by introducing an appropriate force term $\mathbf{F}_{\text{ib}}$ that mimics the effect of the boundary. The boundary force modifies the fluid velocity to ensure that it matches the known boundary velocity $\mathbf{u}_\ell$ at the Lagrangian marker positions $\mathbf{x}_\ell$. The modified fluid velocity $\bar{\mathbf{u}}(\mathbf{x}, t)$ can be expressed in terms of a velocity correction $\delta\mathbf{u}(\mathbf{x}, t)$ as follows

$$\bar{\mathbf{u}}(\mathbf{x}, t) = \mathbf{u}(\mathbf{x}, t) + \delta\mathbf{u}(\mathbf{x}, t)\,. \tag{3.58}$$

Based on the velocity expression given by Equation 3.36, the corresponding corrected velocity is calculated as follows

$$\rho\,(\mathbf{x}, t)\,(\mathbf{u}(\mathbf{x}, t) + \delta\mathbf{u}(\mathbf{x}, t)) = \sum_i \mathbf{c}_i f_i(\mathbf{x}, t) + \frac{1}{2}\,(\mathbf{F}(\mathbf{x}, t) + \mathbf{F}_{\text{ib}}(\mathbf{x}, t))\,\Delta t\,. \tag{3.59}$$

Therefore, the immersed boundary force $\mathbf{F}_{\text{ib}}$ can be expressed as

$$\mathbf{F}_{\text{ib}}(\mathbf{x}, t) = \frac{2\rho\,\delta\mathbf{u}(\mathbf{x}, t)}{\Delta t}\,. \tag{3.60}$$

Similarly, the corresponding immersed boundary force on the Lagrangian points $\mathbf{F}_\ell$ can be obtained in the following way

$$\mathbf{F}_\ell(\mathbf{x}_\ell, t) = \frac{2\rho\,\delta\mathbf{u}_\ell(\mathbf{x}_\ell, t)}{\Delta t}\,, \tag{3.61}$$

where $\delta\mathbf{u}_\ell$ is the velocity correction on the Lagrangian points.

To evaluate the Eulerian body force density $\mathbf{F}_{\text{ib}}$, the force acting on the Lagrangian

points $\mathbf{F}_\ell$ is distributed to the lattice nodes next to the boundary using

$$\mathbf{F}_{\text{ib}}(\mathbf{x},t) = \sum_{\mathbf{x}_\ell} \mathbf{F}_\ell(\mathbf{x}_\ell,t)\,\Phi(\mathbf{x}-\mathbf{x}_\ell)\,\Delta s\,, \tag{3.62}$$

where Δs is the spacing between the Lagrangian points. Considering the boundary force expressions given by Equation 3.60 and Equation 3.61, the force distribution operation in Equation 3.62 can be evaluated in the following way

$$\delta\mathbf{u}(\mathbf{x},t) = \sum_{\mathbf{x}_\ell} \delta\mathbf{u}_\ell(\mathbf{x}_\ell,t)\,\Phi(\mathbf{x}-\mathbf{x}_\ell)\,\Delta s\,. \tag{3.63}$$

To satisfy the no-slip boundary condition, the velocity at the Lagrangian points locations $\mathbf{u}_\ell(\mathbf{x}_\ell,t)$ is calculated by interpolating the fluid velocity at the neighbouring lattice points, including the velocity correction

$$\mathbf{u}_\ell(\mathbf{x}_\ell,t) = \sum_{\mathbf{x}} \left(\mathbf{u}(\mathbf{x},t) + \delta\mathbf{u}(\mathbf{x},t)\right)\,\Phi(\mathbf{x}-\mathbf{x}_\ell)\,\Delta x^2\,. \tag{3.64}$$

The interpolation and distribution procedures described respectively in Equation 3.64 and Equation 3.63 are the source of the diffusive effect due to the implementation of discrete delta functions [148].

In the MDF-IBM algorithm presented by Zhang et al. [46] the interpolation procedure at time step k is implemented as follows

$$\bar{\mathbf{u}}^k(\mathbf{x}_\ell,t) = \sum_{\mathbf{x}} \bar{\mathbf{u}}^k(\mathbf{x},t)\,\Phi(\mathbf{x}-\mathbf{x}_\ell)\,\Delta x^2\,, \tag{3.65a}$$

$$\Delta\mathbf{u}_\ell^k(\mathbf{x}_\ell,t) = \mathbf{u}_\ell(\mathbf{x}_\ell,t) - \bar{\mathbf{u}}^k(\mathbf{x}_\ell,t)\,, \tag{3.65b}$$

$$\mathbf{F}_\ell^k(\mathbf{x}_\ell,t) = \mathbf{F}_\ell^{k-1}(\mathbf{x}_\ell,t) + \frac{2\rho\,\Delta\mathbf{u}_\ell(\mathbf{x}_\ell,t)}{\Delta t}\,, \tag{3.65c}$$

The force distribution is performed with the following steps

$$\Delta \mathbf{u}^k(\mathbf{x},t) = \sum_{\mathbf{x}_\ell} \Delta \mathbf{u}_\ell^k(\mathbf{x}_\ell,t)\,\Phi(\mathbf{x}-\mathbf{x}_\ell)\,\Delta s\,, \tag{3.66a}$$

$$\bar{\mathbf{u}}^{k+1}(\mathbf{x},t) = \bar{\mathbf{u}}^k(\mathbf{x},t)\; + \Delta \mathbf{u}^k(\mathbf{x},t)\,, \tag{3.66b}$$

$$\mathbf{F}_{\text{ib}}^k(\mathbf{x},t) = \mathbf{F}_{\text{ib}}^{k-1}(\mathbf{x},t) + \frac{2\rho\,\Delta \mathbf{u}(\mathbf{x},t)}{\Delta t}\,. \tag{3.66c}$$

The interpolation and distribution steps can be collectively expressed as follows

$$\begin{aligned}\Delta \mathbf{u}_\ell^k(\mathbf{x}_\ell,t) =& \mathbf{u}_\ell(\mathbf{x}_\ell,t) - \sum_{\mathbf{x}}[\bar{\mathbf{u}}^{k-1}(\mathbf{x},t)+ \\ & \sum_{\mathbf{x}_m} \Delta \mathbf{u}_m^{k-1}(\mathbf{x}_m,t)\,\Phi(\mathbf{x}-\mathbf{x}_m)\Delta s_m]\,\Phi(\mathbf{x}-\mathbf{x}_\ell)\,\Delta x^2\,.\end{aligned} \tag{3.67}$$

Considering that $\Delta \mathbf{u}_\ell^k(\mathbf{x}_\ell) = \delta \mathbf{u}_\ell^k(\mathbf{x}_\ell) - \delta \mathbf{u}_\ell^{k-1}(\mathbf{x}_\ell)$ and $\bar{\mathbf{u}}^{k-1}$ is given by the distribution of $\Delta \mathbf{u}_m$, the previous equation can be represented by the following linear system

$$\mathbf{Y}^k = (\mathbf{I}-\mathbf{A})\,\mathbf{Y}^{k-1} + \mathbf{b}\,, \tag{3.68}$$

where the components of the matrix $\mathbf{A}$ and the vectors $\mathbf{Y}$ and $\mathbf{b}$ are respectively

$$\mathbf{A}_{\ell m} = \sum_{\mathbf{x}} \Phi(\mathbf{x}-\mathbf{x}_m)\,\Phi(\mathbf{x}-\mathbf{x}_\ell)\,\Delta s_m\,\Delta x^2\,, \tag{3.69}$$

$$\mathbf{Y}_m = \delta \mathbf{u}_m(\mathbf{x}_m)\,, \tag{3.70}$$

$$\mathbf{b}_\ell = \mathbf{u}_\ell(\mathbf{x}_\ell) - \sum_{\mathbf{x}} \mathbf{u}(\mathbf{x})\,\Phi(\mathbf{x}-\mathbf{x}_\ell)\Delta x^2\,. \tag{3.71}$$

This linear system of equations corresponds to an explicit iterative method whose solution does not require cumbersome matrix inversion procedures. Therefore, this formulation improves computation efficiency compared to implicit methods [46].

The numerical procedure associated with the MDF-IBM formulation can be summarised in algorithmic form as follows

1. Calculate $\|\mathbf{A}\|_\infty$ to determine the relaxation parameter ω.

2. Start the iterative process and set the iteration step to $k = 0$.

   2.1. Set $\bar{\mathbf{u}}(\mathbf{x}) = \mathbf{u}(\mathbf{x})$, $\mathbf{F}_{\mathrm{ib}}(\mathbf{x}) = 0$, and $\mathbf{F}_{\ell}(\mathbf{x}_{\ell}) = 0$.

   2.2. Perform the velocity interpolation steps according to Equation 3.65.

   2.3. Perform the force distribution steps according to Equation 3.66.

   2.4. Advance the iteration step to $k + 1$.

3. Obtain the converged immersed boundary force $\mathbf{F}_{\mathrm{ib}}(\mathbf{x})$.

4. Calculate the hydrodynamic force $\mathbf{F}_{\mathrm{h}}(\mathbf{x})$ and torque $\mathbf{T}_{\mathrm{h}}(\mathbf{x})$.

3.3.4 Relaxed MDF-IBM

This work implements the relaxed MDF-IBM proposed by Zhang et al. [46]. This method introduces an estimated optimal relaxation parameter that accelerates the convergence rate and improves the enforcement of the no-slip boundary condition. To derive the relaxed MDF-IBM scheme, the relaxed Richardson iteration equation is implemented in the linear system presented in Equation 3.68 as follows

$$\mathbf{Y}^{k} = (\mathbf{I} - \omega\mathbf{A})\,\mathbf{Y}^{k-1} + \omega\mathbf{b}\,, \tag{3.72}$$

where ω is the relaxation parameter. The calculation of the optimal relaxation value ω_{opt} results in an additional computational burden for problems involving a large number of Lagrangian points. Therefore, an estimated optimal value $\tilde{\omega}$ can be calculated based on the properties of the infinity norm $\|\mathbf{A}\|_{\infty}$ and the maximum eigenvalue $\lambda_{\max}$

$$\tilde{\omega} = \|\mathbf{A}\|_{\infty}^{-1} \leq \lambda_{\max}^{-1} \leq \omega_{\mathrm{opt}}\,. \tag{3.73}$$

The convergence rate based on this parameter is

$$0 \leq \omega \leq 2\|\mathbf{A}\|_{\infty}^{-1}\,. \tag{3.74}$$

The relaxation parameter is implemented in the MDF-IBM scheme by modifying the interpolation step formulated in Equation 3.65b in the following way

$$\Delta \mathbf{u}_\ell^k(\mathbf{x}_\ell, t) = \omega \left[\mathbf{u}_\ell(\mathbf{x}_\ell, t) - \bar{\mathbf{u}}^k(\mathbf{x}_\ell, t) \right] . \tag{3.75}$$

Since the estimated optimal relaxation parameter should be calculated at every time step for moving boundaries simulations, Zhang et al. [46] explored the possibility of using a constant value for the relaxation parameter. Their work investigated the contributions of different factors and concluded that the choice of delta function, the spacing size between the Lagrangian points, and the no-slip boundary shape have the most prominent impact. Thus, for appropriate problems, a predetermined constant relaxation parameter can be evaluated to simplify the algorithm and improve efficiency.

3.3.5 Internal Mass Effect

As shown in Figure 2.1, IBM schemes model the computational domain using a non-conforming grid and the fluid domain Ω_f is extended inside the solid boundary Γ_s. The solid domain Ω_s is filled with an internal fluid that is subjected to the action of body forces. Similar to the moving bounce-back method [143], IBM does not require destruction or creation of fluid nodes when lattice nodes cross the solid boundary Γ_s in moving boundary problems. However, the interior nodes of the solid region continue to participate in the collision and streaming steps. Thus, the fluid inertial contributions from the nodes located inside the solid are included in the overall solution. As a consequence, the inertia associated with this *internal mass* affects the motion of the solid body [165]. While the internal mass does not alter the flow and pressure field around the solid body, a part of the force and torque exerted on the boundary Γ_s is used to move the internal fluid [157]. Therefore, to calculate the correct hydrodynamic force and torque acting on a solid object, the body forces on the solid boundary are compensated by an additional force $\mathbf{F}_\mathrm{i}$ that takes into consideration the internal mass effect. Because of its effects on the hydrodynamic force, the internal mass effect has been investigated in several studies [107, 110, 111, 157, 161, 165].

In the moving bounce-back method presented by Ladd [143], solid bodies are filled with fluid, and to compensate for the internal mass effect, the equations of motion are integrated using a corrected value for the solid body mass. The effective mass can be evaluated as the sum of the mass of the solid and the mass of the fluid occupied by the solid domain.

Ten Cate et al. [165] suggested that the force acting on a solid body is partly compensated by the change of momentum of the internal mass. The total force exerted on the solid object can be expressed as the sum of internal and external components of the force, where only the external flow field represents a physical contribution to the solid motion. The external component of the force acting on a solid body can be calculated as the change of momentum of the internal fluid between two successive time steps.

In order to determine the hydrodynamic forces acting on solid bodies, Uhlmann [107] proposed to evaluate the momentum balance over the fluid domain. The change of momentum of the internal fluid is approximated by assuming rigid-body motion inside the solid. This approach results in an implicit calculation of the internal mass effect.

Feng [161] implemented the rigid body approximation and observed that the force induced by the internal fluid mass is a passive force resulting from the particle acceleration. Therefore, it was suggested to separate the internal fluid mass from the solid body mass and determine the internal mass term by evaluating solid motion at the previous time step. Contrary to the approach introduced by Uhlmann [107], this approximation determines the internal mass effect explicitly.

The work of Suzuki and Inamuro [157] compared different schemes for approximating the internal mass effect and proposed a Lagrangian points approximation. Their approach determines the internal mass effect directly by calculating the sum of linear and angular momentum of the internal mass over internal Lagrangian points. In this scheme, the velocity of the internal Lagrangian points can be determined by interpolation from the neighbouring lattice nodes. Compared to approaches that evaluate the momentum of the internal fluid on the Eulerian lattice nodes, the Lagrangian points approximation reduces the computational costs for problems involving complex geometries.

Because of its efficiency and simple implementation, the approximation proposed by Feng [161] is used in this work to quantify the internal mass effect. Based on the momentum balance equations introduced in Section 2.4.2, the force and the torque associated with the internal fluid are defined as

$$\mathbf{F}_\mathrm{i} = \frac{\mathrm{d}}{\mathrm{d}t} \int_{\Omega_\mathrm{s}} \rho_\mathrm{f}\, \mathbf{u}\, dV\,, \tag{3.76}$$

$$\mathbf{T}_\mathrm{i} = \frac{\mathrm{d}}{\mathrm{d}t} \int_{\Omega_\mathrm{s}} \rho_\mathrm{f}\, \mathbf{r} \times \mathbf{u}\, dV\,. \tag{3.77}$$

Several approaches have been formulated to calculate the internal mass effect. Assuming rigid-body motion for the fluid occupying the domain of the immersed structure, the force $\mathbf{F}_\mathrm{i}$ and the torque $\mathbf{T}_\mathrm{i}$ resulting from the internal mass are approximated as follows

$$\frac{\mathrm{d}}{\mathrm{d}t} \int_{\Omega_\mathrm{s}} \rho_\mathrm{f}\, \mathbf{u}\, dV = \frac{\rho_\mathrm{f}\, m_\mathrm{p}}{\rho_\mathrm{s}} \frac{\mathrm{d}\mathbf{U}_\mathrm{p}}{\mathrm{d}t}\,, \tag{3.78}$$

$$\frac{\mathrm{d}}{\mathrm{d}t} \int_{\Omega_\mathrm{s}} \rho_\mathrm{f}\, \mathbf{r} \times \mathbf{u}\, dV \approx \frac{\rho_\mathrm{f}\, I_\mathrm{p}}{\rho_\mathrm{s}} \frac{\mathrm{d}\boldsymbol{\Theta}_\mathrm{p}}{\mathrm{d}t}\,, \tag{3.79}$$

where ρ_s, m_p and I_p are respectively the particle density, mass and moment of inertia. $\mathbf{U}_\mathrm{p}$ and $\boldsymbol{\Theta}_\mathrm{p}$ are respectively the translational and angular velocity of the particle's centre of mass.

It should be noted that the condition expressed by Equation 3.78 is valid for an incompressible fluid which satisfies a rigid-body motion on Γ_s, irrespectively of the motion inside the domain Ω_s. It can be demonstrated that the linear momentum of the internal mass is exactly equal to that of the rigid body with the same density of the internal mass [107, 157]

$$\int_{\Omega_\mathrm{s}} \mathbf{u}\, dV = \int_{\Omega_\mathrm{s}} \mathbf{U}_\mathrm{p}\, dV\,. \tag{3.80}$$

Assuming that the internal fluid is incompressible, the following equation is obtained

$$\frac{\mathrm{d}}{\mathrm{d}t} \int_{\Omega_\mathrm{s}} \mathbf{U}_\mathrm{p}\, dV = \int_{\Omega_\mathrm{s}} \frac{\mathrm{d}\mathbf{U}_\mathrm{p}}{\mathrm{d}t}\, dV\,. \tag{3.81}$$

Since the density of the internal fluid is uniform, the expression given in Equation 3.78 can be derived. Conversely, the expression of the angular momentum given by Equa-

tion 3.79 is only valid for an incompressible fluid that satisfies rigid-body motion throughout the domain Ω_s [107]. Thus, the condition expressed by Equation 3.79 does not satisfy a similar equality and it is approximated.

Feng [161] approximates the time derivatives in Equation 3.78 and 3.79 by the change between two successive time steps yielding

$$\mathbf{F}_i = \frac{\rho_f}{\rho_s} m_p \frac{\mathbf{U}_p(t) - \mathbf{U}_p(t - \Delta t)}{\Delta t}, \tag{3.82}$$

$$\mathbf{T}_i = \frac{\rho_f}{\rho_s} I_p \frac{\boldsymbol{\Theta}_p(t) - \boldsymbol{\Theta}_p(t - \Delta t)}{\Delta t}. \tag{3.83}$$

3.3.6 Numerical Stability

In moving boundary problems, the domain occupied by the fluid changes in time and the location of the boundary depends both on the fluid flow and the motion of the solid structure. For non-conforming methods such as the IBM, the boundary conditions implementation strategy needs to ensure that the kinematic and dynamic properties at the fluid-structure interface are matched. In order to achieve this condition, when the fluid flow equations are solved, the no-slip boundary condition needs to be satisfied, and at the same time, the hydrodynamic force and torque on the interface are required to determine the solid structure equations.

In weakly coupled IBM algorithms, the coupling conditions at the fluid-solid interface are not enforced simultaneously due to the sequential execution of the fluid and structural solvers. Therefore, if the coupling condition is not satisfied with sufficient accuracy, the resulting error may cause numerical instability. Numerical stability problems have been attributed to applications where the internal mass is comparable to or lower than the solid body mass [43, 102, 105, 110]. In such cases, the internal mass becomes the most significant contribution to the dynamics of the structural response, affecting the hydrodynamic force and torque acting on the solid body. Because weakly coupled schemes are explicit time marching methods, the force term is evaluated based on the kinematic conditions of the structure calculated at the previous time step. Thus, the internal mass effect significantly influences the coupled solution, leading to numerical instability.

In contrast, strongly coupled schemes improve the performance of IBM algorithms for problems involving low structural densities [43, 105, 112]. These strategies achieve better satisfaction of the coupling conditions with an implicit time integration and eliminate numerical stability problems. For applications involving significant internal mass, the convergence properties of strongly coupled schemes can be enhanced using under-relaxation techniques in order to achieve robust and efficient solutions [43].

3.3.7 Strongly Coupled IBM

In order to alleviate the computational cost associated with the traditional strongly coupled approaches, Wang and Eldredge [112] incorporated the IBM in the coupling conditions. The iterative block Gauss-Seidel scheme employed to solve the coupling conditions implements force corrections that are relaxed before they are used by the rigid body solver. They showed that a relaxation parameter based on an estimation of the internal mass successfully optimises convergence and achieves better stability even for density ratios of $\rho_\mathrm{s}/\rho_\mathrm{f} = 0.01$. Lācis at al. [110] presented a non-iterative strongly coupled scheme that solves the algebraic system of equations using a block LU decomposition. It was demonstrated that the method is second-order accurate in space and it achieves stable solutions for density ratio values of $\rho_\mathrm{s}/\rho_\mathrm{f} \geq 0.0001$. The strongly coupled method introduced by Tschisgale et al. [166] extends the range of stable computation to vanishing particle densities by implementing a semi-implicit scheme based on the IBM.

In the strategy presented by Zhang et al. [167], the coupling of the fluid and solid equations is achieved by implementing implicit velocity corrections in the IBM scheme. The coupled equation for a particle immersed in a fluid can be derived by considering the hydrodynamic force acting on the solid given by Equation 3.56, which accounts for both the immersed boundary force and the contribution of the internal mass effect. Including the gravitational force as an external body force, the equation of motion is expressed as

$$m_\mathrm{p}\frac{\mathrm{d}\mathbf{U}_\mathrm{p}}{\mathrm{d}t} = \mathbf{F}_\mathrm{h} + \left(1 - \frac{\rho_\mathrm{f}}{\rho_\mathrm{s}}\right) m_\mathrm{p}\,\mathbf{g}\,, \tag{3.84}$$

where the time derivative can be discretised as

$$\frac{\mathrm{d}\mathbf{U}_\mathrm{p}}{\mathrm{d}t} = \frac{1}{\Delta\, t^2}\,\left(\mathbf{X}_\mathrm{p}^{n+1} - 2\,\mathbf{X}_\mathrm{p}^{n} + \mathbf{X}_\mathrm{p}^{n-1}\right)\,. \tag{3.85}$$

As discussed in Section 3.3.5, the internal mass effect $\mathbf{F}_\mathrm{i}$ can be expressed as

$$\mathbf{F}_\mathrm{i} = \frac{\rho_\mathrm{f}}{\rho_\mathrm{s}}\, m_\mathrm{p}\, \frac{\mathrm{d}\mathbf{U}_\mathrm{p}}{\mathrm{d}t}\,. \tag{3.86}$$

The immersed boundary force on the Lagrangian points $\mathbf{F}_\ell$ is calculated as

$$\mathbf{F}_\ell(\mathbf{x}_\ell, t) = \frac{2\rho\,\delta\mathbf{u}_\ell(\mathbf{x}_\ell, t)}{\Delta t}\,, \tag{3.87}$$

where the velocity correction $\delta\mathbf{u}_\ell$ represents the unknown variable of the linear system defined by Equation 3.69–3.71, and it can be expressed as

$$\delta\mathbf{u}_\ell(\mathbf{x}_\ell) = \mathbf{A}^{-1}\left[\mathbf{u}_\ell(\mathbf{x}_\ell) - \sum_{\mathbf{x}} \mathbf{u}(\mathbf{x})\,\Phi(\mathbf{x}-\mathbf{x}_\ell)\Delta x^2\right]\,. \tag{3.88}$$

For later convenience, the matrix $\tilde{\mathbf{A}}$ is introduced

$$\tilde{\mathbf{A}}_{\ell m} = \sum_{\mathbf{x}} \Phi(\mathbf{x}-\mathbf{x}_m)\,\Phi(\mathbf{x}-\mathbf{x}_\ell)\,\Delta x^2, \tag{3.89}$$

where $\mathbf{A} = \tilde{\mathbf{A}}\,\Delta s_m$. By substituting the previous definitions into Equation 3.84, the following expression is obtained

$$\begin{aligned}&\left(1 - \frac{\rho_\mathrm{f}}{\rho_\mathrm{s}}\right)\frac{1}{\Delta\, t^2}\,\left(\mathbf{X}_\mathrm{p}^{n+1} - 2\,\mathbf{X}_\mathrm{p}^{n} + \mathbf{X}_\mathrm{p}^{n-1}\right) = \\ &-\frac{2\,S_\mathrm{p}}{\Delta t\, V_\mathrm{p}}\,\frac{\rho_\mathrm{f}}{\rho_\mathrm{s}}\,\tilde{\mathbf{A}}^{-1}\left[\mathbf{u}_\ell^n(\mathbf{x}_\ell) - \sum_{\mathbf{x}} \mathbf{u}^n(\mathbf{x})\,\Phi(\mathbf{x}-\mathbf{x}_\ell)\Delta x^2\right] + \left(1 - \frac{\rho_\mathrm{f}}{\rho_\mathrm{s}}\right)\mathbf{g}\,,\end{aligned} \tag{3.90}$$

where V_p is the volume of the particle and S_p is the number of Lagrangian points. The velocity at the Lagrangian marker positions $\mathbf{u}_\ell$ is determined from the rigid–body

motion of the particle according to

$$\mathbf{u}_\ell = \mathbf{U}_\mathrm{p} + \boldsymbol{\Theta}_\mathrm{p} \times \mathbf{r}\,, \tag{3.91}$$

The particle velocity $\mathbf{U}_\mathrm{p}$ is discretised applying the following method

$$\mathbf{U}_\mathrm{p} = \frac{1}{\Delta t}\left[\Gamma\left(\mathbf{X}_\mathrm{p}^{n+1} - \mathbf{X}_\mathrm{p}^{n}\right) + (1-\Gamma)\left(\mathbf{X}_\mathrm{p}^{n} - \mathbf{X}_\mathrm{p}^{n+1}\right)\right]\,, \tag{3.92}$$

where the parameter Γ is used to achieve different temporal discretisation schemes. An analogous discretisation can be applied to the angular velocity $\boldsymbol{\Theta}_\mathrm{p}$. For $\Gamma = 0$, the velocity is computed entirely from known values at previous time levels (n and $n-1$), corresponding to an explicit scheme. Setting $\Gamma = 0.5$ results in a semi-implicit scheme of first–order accuracy, in which the velocity is evaluated using the displacements at $n-1$ and $n+1$ as in the strong–coupling formulation presented in Ref. [167]. When $\Gamma = 1$, the velocity depends on the displacement between n and $n+1$, providing a fully implicit first–order scheme. For $\Gamma = 1.5$, a second–order implicit formulation is obtained, and the new particle velocity is more strongly influenced by the most recent position update.

Similarly, the rotational dynamics of the particle are governed by the balance of angular momentum between the hydrodynamic torque and the internal torque associated with the fluid enclosed within the particle. The governing equation for the particle rotation is given by

$$I_\mathrm{p}\frac{\mathrm{d}\boldsymbol{\Theta}_\mathrm{p}}{\mathrm{d}t} = \mathbf{T}_\mathrm{h}\,. \tag{3.93}$$

The internal torque $\mathbf{T}_\mathrm{i}$ is determined by

$$\mathbf{T}_\mathrm{i} = \frac{\rho_\mathrm{f}}{\rho_\mathrm{s}}\, I_\mathrm{p}\, \frac{\mathrm{d}\boldsymbol{\Theta}_\mathrm{p}}{\mathrm{d}t}\,. \tag{3.94}$$

Considering the definitions of $\mathbf{F}_\ell$ and $\delta\mathbf{u}_\ell$ given by Equation 3.87–3.88, the following

expression is derived

$$\begin{aligned}&\left(1-\frac{\rho_\mathrm{f}}{\rho_\mathrm{s}}\right)\frac{1}{\Delta\, t^2}\,\left(\boldsymbol{\theta}_\mathrm{p}^{n+1}-2\,\boldsymbol{\theta}_\mathrm{p}^{n}+\boldsymbol{\theta}_\mathrm{p}^{n-1}\right)=\\&-\frac{2\rho_\mathrm{f}\,S_\mathrm{p}}{I_\mathrm{p}\,\Delta t}\,\tilde{\mathbf{A}}^{-1}\,\mathbf{r}\times\left[\mathbf{u}_\ell^n(\mathbf{x}_\ell)-\sum_{\mathbf{x}}\mathbf{u}^n(\mathbf{x})\,\Phi(\mathbf{x}-\mathbf{x}_\ell)\Delta x^2\right].\end{aligned}\tag{3.95}$$

The discretised coupled translational and rotational equations can be expressed as linear systems of the form

$$\mathbf{Y}^{k+1}=(\mathbf{I}-\omega\mathbf{A}^\star)\,\mathbf{Y}^k+\omega\mathbf{b}^\star\,,\tag{3.96}$$

which can be solved iteratively using the relaxed MDF approach. The interpolation and distribution operations used in the weakly coupled IBM formulation (Equation 3.65–3.66) are modified to account for the implicit coupling between the fluid and solid phases. The velocity interpolation steps are implemented as follows

$$\bar{\mathbf{u}}^{k+1}(\mathbf{x}_\ell)=\sum_{\mathbf{x}}\bar{\mathbf{u}}^{k+1}(\mathbf{x})\,\Phi(\mathbf{x}-\mathbf{x}_\ell)\,\Delta x^2\,,\tag{3.97a}$$

$$\mathbf{u}_\ell^{k+1}(\mathbf{x}_\ell)=(1-\omega)\,\mathbf{u}_\ell^{k}(\mathbf{x}_\ell)+\omega\,\mathbf{u}_\ell^{k+1}(\mathbf{x}_\ell)\,,\tag{3.97b}$$

$$\Delta\mathbf{u}_\ell^{k+1}(\mathbf{x}_\ell)=-\frac{\rho_\mathrm{s}-\rho_\mathrm{f}}{\rho_\mathrm{s}}\,\frac{V_\mathrm{p}}{\Delta s}\left(\mathbf{u}_\ell^{k+1}(\mathbf{x}_\ell)-\mathbf{u}_\ell^{k}(\mathbf{x}_\ell)\right),\tag{3.97c}$$

$$\mathbf{F}_\ell^{k+1}(\mathbf{x}_\ell)=\mathbf{F}_\ell^{k}(\mathbf{x}_\ell)+\frac{2\rho_\mathrm{f}}{\Delta t}\,\Delta\mathbf{u}_\ell(\mathbf{x}_\ell)\,.\tag{3.97d}$$

The distribution iteration is given by

$$\Delta\mathbf{u}^{k}(\mathbf{x})=\sum_{\mathbf{x}_\ell}\Delta\mathbf{u}_\ell^{k}(\mathbf{x}_\ell)\,\Phi(\mathbf{x}-\mathbf{x}_\ell)\,\Delta s\,,\tag{3.98a}$$

$$\bar{\mathbf{u}}^{k+1}(\mathbf{x})=\bar{\mathbf{u}}^{k}(\mathbf{x})\;+\Delta\mathbf{u}^{k}(\mathbf{x})\,.\tag{3.98b}$$

The strong-coupling interface is established by applying simultaneous velocity corrections to the fluid and solid domains. The strong-coupling algorithm can be described as follows:

1. Calculate $\|\mathbf{A}\|_\infty$ to determine the relaxation parameter ω.

2. Start the iterative process and set the iteration step to $k = 0$.

   2.1. Set $\bar{\mathbf{u}}(\mathbf{x}) = \mathbf{u}(\mathbf{x})$ and $\mathbf{F}_\ell(\mathbf{x}_\ell) = 0$.

   2.2. Perform the force distribution iteration according to Equation 3.98.

   2.3. Perform the velocity interpolation steps according to Equation 3.97.

   2.4. Advance the iteration step to $k + 1$.

3. Distribute the last velocity correction as indicated by Equation 3.98

4. Distribute the Lagrangian force $\mathbf{F}_\ell(\ell)$ using Equation 3.62.

5. Calculate the hydrodynamic force $\mathbf{F}_\mathrm{h}(\mathbf{x})$ and torque $\mathbf{T}_\mathrm{h}(\mathbf{x})$.

3.4 Discrete Element Method

In order to accurately model particle interactions, the discrete element method (DEM) is introduced as a particle solver. Originally developed by Cundall and Strack [64] for the simulation of rock and soil mechanics, the DEM provides a numerical framework to model granular and particulate materials as systems composed of discrete particles interacting with each other [40]. Following the work of Tsuji et al. [168], DEM has been successfully coupled with fluid solvers to investigate particle-laden flows and fluidised systems [40, 169].

DEM solves numerically Newton's equations of motion for a system of particles that interact with each other through intermolecular potentials and force fields. The equations of motion introduced in Section 2.4.1 can be solved using integration algorithms to update the particle position $\mathbf{X}_\mathrm{p}$. A simple and effective numerical method is the Verlet integration rule

$$\mathbf{X}_\mathrm{p}(t + \Delta t) = 2\mathbf{X}_\mathrm{p}(t) - \mathbf{X}_\mathrm{p}(t - \Delta t) + \frac{\mathbf{F}_\mathrm{p}(t)}{m_\mathrm{p}} \Delta t^2 \,, \tag{3.99}$$

where the truncation error is of order $\mathcal{O}^4$. This implementation of the Verlet algorithm is based on positions and accelerations from the previous time step. The velocity $\mathbf{U}_\mathrm{p}$

can be calculated from

$$\mathbf{U}_{\mathrm{p}}(t) = \frac{\mathrm{d}\mathbf{X}_{\mathrm{p}}}{\mathrm{d}t} = \frac{\mathbf{X}_{\mathrm{p}}(t+\Delta t) - \mathbf{X}_{\mathrm{p}}(t-\Delta t)}{2\,\Delta t}\,, \tag{3.100}$$

where the truncation error is of order $\mathcal{O}^2$. The angle of rotation of the particle $\boldsymbol{\theta}_{\mathrm{p}}$ is updated according to the following expression

$$\boldsymbol{\theta}_{\mathrm{p}}(t+\Delta t) = 2\boldsymbol{\theta}_{\mathrm{p}}(t) - \boldsymbol{\theta}_{\mathrm{p}}(t-\Delta t) + \frac{\mathbf{T}_{\mathrm{p}}(t)}{I_{\mathrm{p}}}\Delta t^2\,. \tag{3.101}$$

The angular velocity $\boldsymbol{\Theta}_{\mathrm{p}}$ is determined as follows

$$\boldsymbol{\Theta}_{\mathrm{p}}(t) = \frac{\mathrm{d}\boldsymbol{\theta}_{\mathrm{p}}}{\mathrm{d}t} = \frac{\boldsymbol{\theta}_{\mathrm{p}}(t+\Delta t) - \boldsymbol{\theta}_{\mathrm{p}}(t-\Delta t)}{2\,\Delta t}\,. \tag{3.102}$$

More accurate estimates of the velocities can be obtained using the velocity Verlet algorithm in the form

$$\mathbf{U}_{\mathrm{p}}\left(t + \frac{\Delta t}{2}\right) = \mathbf{U}_{\mathrm{p}}(t) + \frac{\mathbf{F}_{\mathrm{p}}(t)}{2\,m_{\mathrm{p}}}\,\Delta t\,, \tag{3.103a}$$

$$\mathbf{X}_{\mathrm{p}}(t+\Delta\,t) = \mathbf{X}_{\mathrm{p}}(t) + \mathbf{U}_{\mathrm{p}}\left(t + \frac{\Delta t}{2}\right)\,, \tag{3.103b}$$

$$\mathbf{U}_{\mathrm{p}}(t+\Delta\,t) = \mathbf{U}_{\mathrm{p}}\left(t + \frac{\Delta t}{2}\right) + \frac{\mathbf{F}_{\mathrm{p}}(t)}{2\,m_{\mathrm{p}}}(t+\Delta\,t)\,. \tag{3.103c}$$

In the first step, the velocities are updated at an intermediate time $t + 1/2\,\Delta\,t$ using the values of the accelerations at time t. Then, these mid-step velocities are used to advance the coordinates from time t to $t + \Delta\,t$. Finally, the force is evaluated at time $t + \Delta\,t$ to calculate the velocity at the step $t + \Delta\,t$. The velocity Verlet algorithm is the most commonly used time integration algorithm because of its stability and simplicity.

The contact model provides the physical foundation of DEM, defining the interaction mechanism and the resulting contact forces. The DEM formulation adopted in this work is based on the contact model described in Section 2.4.3, allowing small particle overlaps and computing the resulting forces from linear elastic and damping relations. In the present work, the critical value ε_{c} is set to $2\Delta x$ to accommodate the range of the four-point discrete delta function [159].

3.5 Algorithm

In the numerical method considered in this work, CLBM is used as the fluid solver, IBM enforces the fluid-solid boundary condition, and DEM solves particle interactions. The different solvers interact by bi-directional information exchange. The macroscopic fluid velocity calculated by CLBM is used to compute the IBM forces that are in turn needed to determine the hydrodynamic force acting on solid bodies. This quantity serves as an input to the DEM solver to calculate the locations and velocities of the Lagrangian points. These values are then implemented in the IBM solver in order to enforce the no-slip boundary condition. The combined DEM-IB-CLMB framework based on the work of Zhang et al. [46, 159] can be summarised in the following steps.

1. Initialise the distribution functions $f_i(\mathbf{x}, t)$ at each lattice node as the equilibrium distribution function.
2. Distribute the Lagrangian points uniformly on the immersed body boundary.
3. Calculate the macroscopic fluid variables according to Equation 3.3 and 3.4.
4. Perform the relaxed MDF-IBM either using the weak coupling (Section 3.3.3) or the strongly coupled velocity-correction scheme (Section 3.3.7).
5. Calculate the hydrodynamic force $\mathbf{F}_\mathrm{h}(\mathbf{x})$ and torque $\mathbf{T}_\mathrm{h}(\mathbf{x})$.
6. Perform collision and streaming steps following Equation 3.5 and 3.6.
7. Perform the DEM.
   - 7.1. Detect particle interaction.
   - 7.2. Compute the contact force $\mathbf{F}_\mathrm{c}$ based on Equation 2.41.
   - 7.3. Calculate the total force acting on the particles.
   - 7.4. Update the rigid motion of the particles according to Equation 3.99–3.102.
8. Update the locations $\mathbf{x}_\ell$ and velocities $\mathbf{u}_\ell(\mathbf{x}_\ell)$ of Lagrangian points.
9. Advance time step.

3.6 Summary

This chapter presented the numerical framework implemented to model coupled fluid-structure systems and its advantages compared to traditional methods. The lattice Boltzmann equation was formulated under suitable assumptions and approximations, providing the basis of the lattice Boltzmann method used for the simulation of fluid flow. The analysis of the LBM formulation indicated its main advantages compared to traditional methods, including the simple implementation, the ability to capture microscopic flow phenomena, and the parallel computing capabilities. At the same time, the main drawbacks of the different LBM implementations were explained, focusing on the complex collision operator. This problem highlighted the importance of advanced strategies such as the CLBM, which improves numerical stability by retaining Galilean invariance. Additionally, the difficulties associated with modelling moving geometries and complex fluid-solid boundary shapes were examined, and the shortcomings of popular numerical methods were systematically discussed.

The general numerical implementation of the IBM and its realisation in the LBM framework were discussed by comparing different strategies. The analysis highlighted the importance of an accurate and efficient enforcement of the no-slip boundary condition at the fluid-solid interface, which is achieved by advanced schemes such as the MDF-IBM. Additionally, the relaxed scheme was considered to improve computational efficiency by accelerating the convergence rate. Because of its significant effect on the hydrodynamic force and torque acting on moving solid bodies, the internal mass effect was explained, and the strategies proposed to quantify it were systematically discussed. The comparison between fluid-solid coupling strategies highlighted important numerical stability implications and established the motivation for incorporating the strong-coupling formulation within the proposed numerical framework.

In addition to the IBM, the present strategy to model fluid-solid interaction problems is supplemented by the DEM, which allows to detect particle interaction and calculates contact forces. The combination of these approaches forms the basis of the numerical framework considered in the remainder of this thesis.

Chapter 4

Validation and Verification of the LBM Solver

4.1 Introduction

The present chapter focuses on validating the LBM solver through representative benchmark cases designed to explore the combined influence of different numerical parameters on the flow behaviour. The validation focuses exclusively on the fluid solver, establishing a foundation for the subsequent FSI problems. The BGK, TRT, and MRT collision models are considered to demonstrate the solver's performance across common LBM formulations, while the CLBM formulation is applied in later chapters within the fluid–structure framework. This chapter aims to provide insight into the numerical behaviour of LBM schemes as fluid solvers. The objective is to examine how numerical accuracy and stability are affected by the choice of relaxation parameters, collision operator, and boundary conditions treatment. In the BGK formulation, the relaxation time is directly linked to the physical viscosity, and the method exhibits viscosity-dependent behaviour that affects the predicted flow field. The analysis presented in this chapter demonstrates that this leads to a velocity slip at the boundary. A systematic study is therefore performed to test the performance of the BGK, TRT, and MRT models, assessing their stability, accuracy, computational cost, and the effort associated with selecting appropriate relaxation parameters. The resulting comparison establishes the

conditions for reliable use of each scheme, clarifies their principal limitations, and motivates the adoption of more advanced collision operators and forcing strategies in the subsequent chapters.

The benchmark problem is formulated in Section 4.2, while the numerical setup is described in Section 4.3. The subsequent sections address the main numerical parameters: the effects of Reynolds number (Section 4.4), relaxation time (Section 4.5), and boundary-condition treatment (Section 4.6). The influence of different collision operators is assessed in Section 4.7, where the BGK, TRT, and MRT models are systematically compared. Finally, the chapter concludes by consolidating individual findings and discussing the overall impact of the numerical parameters.

4.2 Problem Statement

The lid-driven square cavity flow in 2D is considered as a test case to compare different Lattice Boltzmann models. This problem is widely used as a benchmark because it displays complex flow features that can provide useful insight into the accuracy and stability of the numerical method. Since it is a well-known benchmark problem, it has been studied extensively and numerous works are available for reference and validation [170, 171].

The lid-driven cavity consists of a square cavity filled with fluid. At the top boundary, a tangential velocity u_w is applied to the lid to drive the fluid flow in the cavity. On the other three stationary rigid walls, a no-slip boundary condition is applied. While the problem geometry and the boundary conditions are relatively simple, the flow exhibits complex features. On the top boundary, where the fluid flow is being driven by the moving wall, the velocity approaches the value set by the boundary condition. The fluid is driven into the wall on the right side, where it flows downward before moving back up the left side of the cavity. This motion creates a large vortex at the centre of the cavity, and the separation of the flow at the bottom corners forms two additional smaller vortices. As the Reynolds number increases, the vortices become more prominent, and an additional vortex develops at the top left corner. At high values of the Reynolds number, the large vortex is located exactly in the centre of the cavity and

when it is further increased, the flow becomes unsteady and eventually turbulent.

4.3 Numerical Simulations

The numerical setup adopted for the benchmark simulations is established by defining a nondimensional formulation for the simulation parameters. The computational methodology is then outlined, including the domain configuration, boundary-condition treatment, and collision models used in the LBM solver.

4.3.1 Simulation Parameters

For all numerical results presented in this work, the simulation parameters are defined within a consistent nondimensional framework. The numerical computations are performed in *lattice units*, in which physical variables are expressed in a dimensionless form. Therefore, the adopted formulation requires an initial mapping of the physical parameters to their lattice representations, while the simulation results expressed in lattice units are subsequently converted back to dimensional quantities for physical interpretation and comparison.

The nondimensional form of a physical quantity is obtained by expressing it with respect to an appropriate reference scale of the same physical dimension. In this work, the lattice spacing Δx, time step Δt, and reference density ρ are used as the fundamental scaling quantities. Under these conventions, all derived physical parameters are expressed in lattice units through appropriate combinations of the fundamental conversion factors. In particular, the kinematic viscosity is linked to the relaxation time τ by the following expression

$$\nu = {c_s}^2 \left(\tau - \frac{1}{2}\right) \frac{\Delta x^2}{\Delta t}\,, \tag{4.1}$$

where $c_s = \sqrt{1/3}$. For a given lattice resolution and time step, the relaxation time is therefore determined directly from the prescribed viscosity.

Unless otherwise stated, all dimensional parameters reported for benchmark cases are expressed in CGS units, while all numerical computations are performed in lattice units.

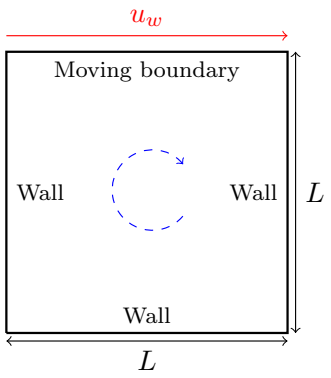


Figure 4.1: Schematics of the lid-driven cavity problem configuration.

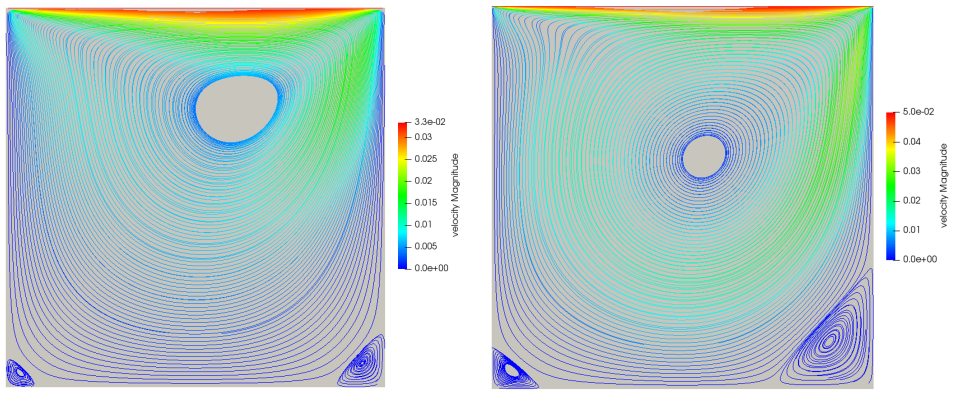
4.3.2 Methodology

This numerical test case is simulated using the LBM, and the results are then compared with the work of Ghia et al. [170]. The numerical simulation domain is shown in Figure 4.1. On the top boundary, a Zou-He [145] velocity boundary condition is applied, and on the other three remaining stationary walls bounce-back boundary conditions are imposed. A uniform lattice with the D2Q9 velocity set model is used to run all the simulations.

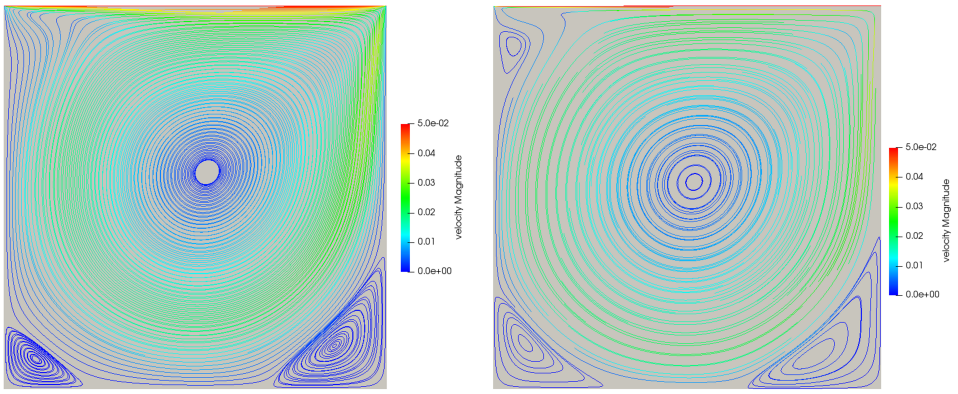
The simulations are performed for different Reynolds numbers. Starting from $Re = 100$, the Reynolds number is progressively increased to the value $Re = 3200$ to limit the simulations to a steady flow case. The relaxation time τ is another fundamental parameter in LBM simulations, and its effects on the fluid flow are tested for a range of values $\tau \in [0.55, 4]$. Both fullway and halfway bounce-back boundary conditions are used in order to compare their numerical implementation and performance. Furthermore, the BGK, TRT and MRT models for the collision operators are used to evaluate the accuracy and stability of the numerical method [125, 172, 173].

4.4 Effect of the Reynolds Number

The simulation setup considered a relaxation time $\tau = 0.6$, the BGK collision operator and fullway bounce-back wall conditions. The values of the relaxation time τ and



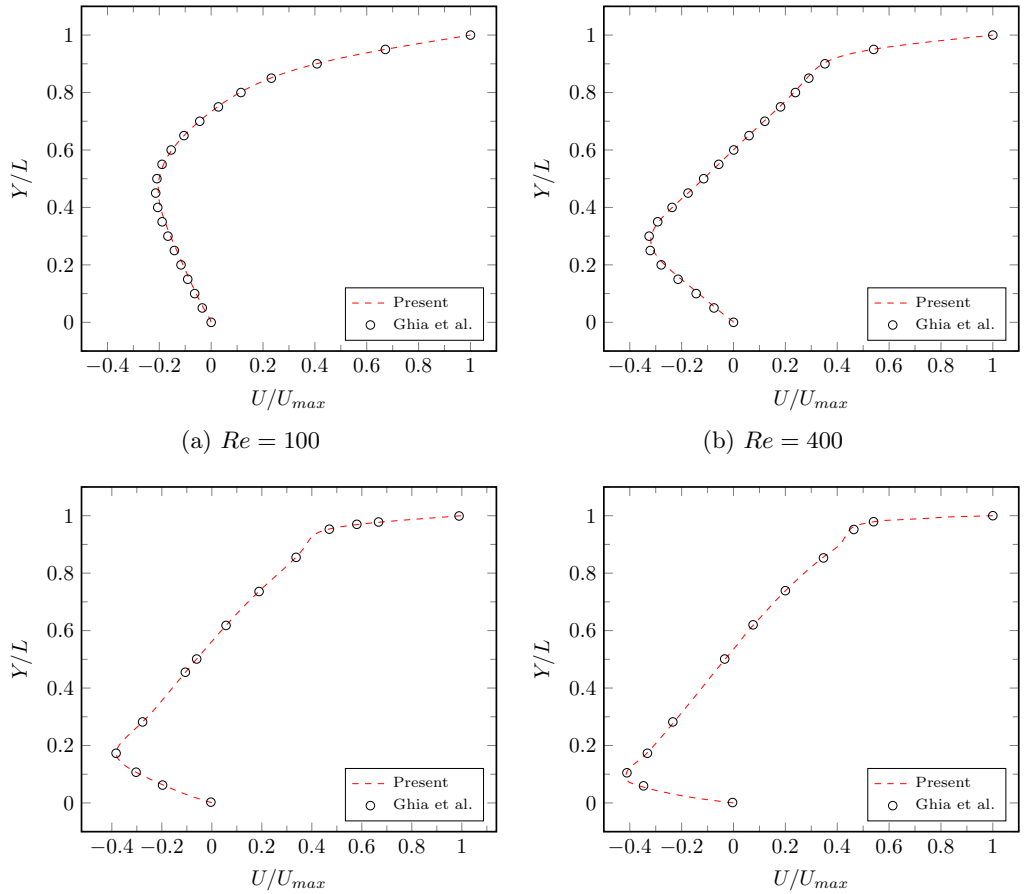
(a) $Re = 100$ (b) $Re = 400$



(c) $Re = 1000$ (d) $Re = 3200$

Figure 4.2: Streamlines for the lid-driven cavity flow at increasing Reynolds numbers.

wall velocity u_w affect the stability and accuracy of the results. In this case, their values are chosen so that the grid definition is sufficiently large to guarantee the desired accuracy without impacting the memory requirements. The corresponding simulation parameters are reported in Table 4.2. As shown in Figure 4.2, for Reynolds numbers $Re = 100$ to $Re = 1000$, the streamlines show a central vortex and two smaller vortices in the bottom corners. As the Reynolds number increases, the large vortex moves closer to the centre point of the cavity, and the corner vortices become larger. At Reynolds number $Re = 3200$, an additional vortex develops at the top left corner, and the larger one is almost exactly in the middle of the square cavity. The LBM simulations for the different Reynolds numbers are compared to the results of Ghia et al. [170]. Figure 4.3 describes the U-velocity profile for the different values of Re.



(a) $Re = 100$ (b) $Re = 400$

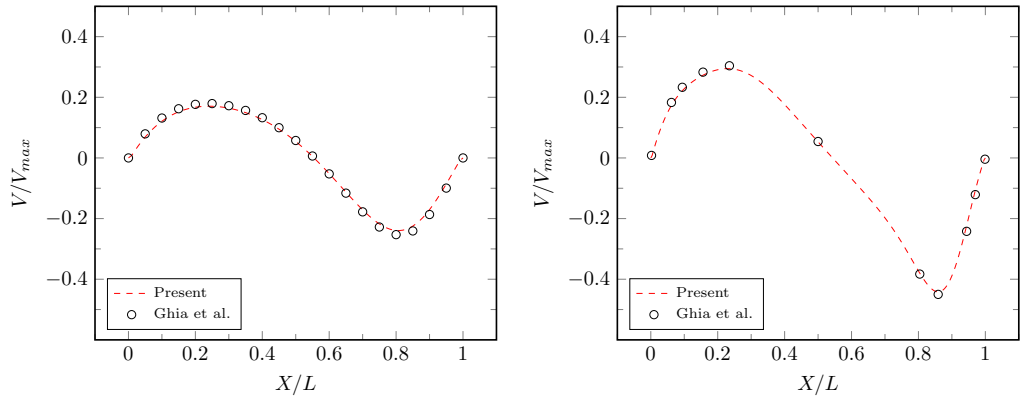
(c) $Re = 1000$ (d) $Re = 3200$

Figure 4.3: U-velocity profile along the central vertical line for the lid-driven cavity flow at increasing Reynolds numbers.

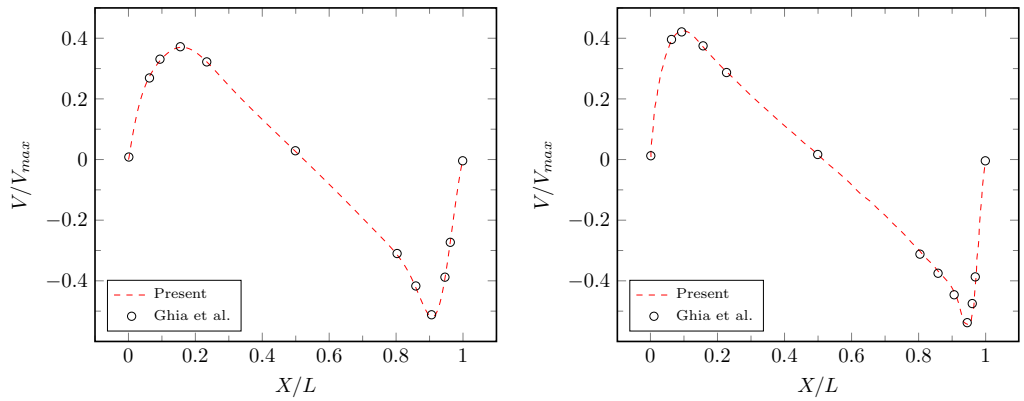
The results show good agreement with the reference simulations for the whole Reynolds number range. Figure 4.4 illustrates the different V-velocity profiles for increasing Re and confirms the close match with the reference results.

4.5 Effect of the Relaxation Time

The relaxation time τ is increased from $\tau = 0.6$ to $\tau = 4$ to evaluate its effects on the solution. The simulations are performed using the BGK collision operator, fullway bounce-back boundary conditions and a constant value of the Reynolds number $Re = 100$. The number of lattice nodes N is initially kept fixed, and the wall velocity u_w is



(a) $Re = 100$ (b) $Re = 400$



(c) $Re = 1000$ (d) $Re = 3200$

Figure 4.4: V-velocity profile along the central horizontal line for the lid-driven cavity flow at increasing Reynolds numbers.

adjusted to ensure stability for the chosen values of Re and τ. As the relaxation time τ increases, the simulations become unstable, and so the grid size has to be increased accordingly. Table 4.1 lists the simulated relaxation times and the corresponding size of the domain. The velocity profiles for the different relaxation times τ are shown in Figure 4.5. These results demonstrate the dependency of the solution on the value of the relaxation time τ and therefore the simulations are *viscosity-dependent* [48]. The detail in Figure 4.5 shows that the accuracy deteriorates as τ increases. The domain size is a compromise between the best spatial resolution possible and the available computational resources. To run the simulations for $\tau = 2$ and $\tau = 4$, the grid size is increased to ensure a sufficiently small Mach number Ma while maintaining a constant

Table 4.1: Relaxation times τ and corresponding grid sizes N for the lid-driven cavity flow simulations.

Relaxation time τ	Grid size N
0.6	101x101
0.8	101x101
1	101x101
2	251x2511
4	1460x1460

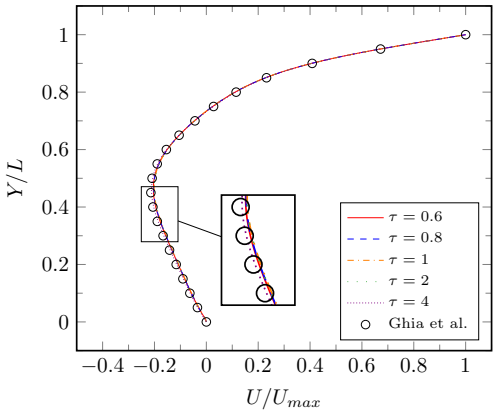


Figure 4.5: U-velocity profile along the central vertical line for the lid-driven cavity flow at increasing relaxation times.

Re. The results for $\tau = 4$ show the best match with the reference simulation because the large domain size enhances accuracy. However, the run time and memory requirements to perform these simulations are significantly larger than the previous ones due to the increased computational domain size.

4.6 Effect of the Boundary Conditions

The halfway bounce-back method is an alternative strategy to implement the bounce-back boundary conditions. This scheme modifies the propagation step rather than the collision, achieving second-order accuracy. The simulations performed implementing halfway bounce-back conditions for $Re = 100$ and the BGK collision operator are in agreement with the corresponding results obtained with the fullway bounce-back

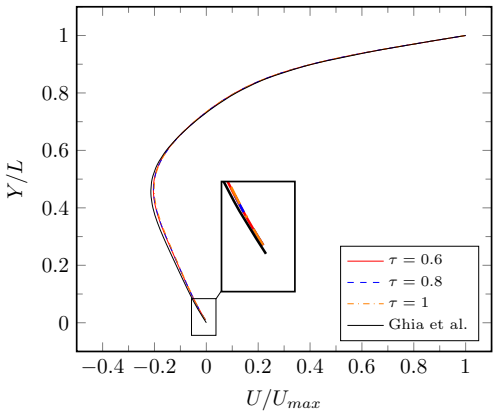


Figure 4.6: U-velocity profile along the central vertical line for the lid-driven cavity flow at increasing relaxation times, using the halfway bounce-back scheme.

method. The effect of the different implementation of the boundary conditions is usually negligible for sufficiently large domains. Conversely, for a small enough grid size the results show an interesting behaviour. To investigate that case, a $N = 36$ lattice is chosen and the relaxation time is increased from $\tau = 0.6$ to $\tau = 0.8$. The different profiles for the U-velocity are presented in Figure 4.6. Similarly to the fullway bounce-back scheme, the solution depends on the value of the relaxation time, and the accuracy deteriorates as τ increases. The detail in Figure 4.6 displays a peculiar feature of the halfway bounce-back scheme. When this method is used to enforce the no-slip boundary condition together with the BGK collision model, the exact location of the boundary depends on the value of the relaxation time. This numerical error violates the physics of the problem as the no-slip condition is no longer valid at the exact location of the boundary [174]. Because of its dependence on the relaxation time, this unphysical condition can be interpreted equivalently as a viscosity-dependent slip velocity [175]. This result is an important drawback of the standard LBM with bounce-back boundary conditions. Analytical considerations prove that there is only one τ value that locates the boundary exactly halfway on the lattice link [48]. Other values of τ lead to a shift of the location of the effective boundary condition and an unphysical slip velocity at the wall. Figure 4.6 shows that the reference solution predicts the correct no-slip velocity condition at the boundary, whereas the LBM results display a slip velocity. Since there

Table 4.2: Grid sizes N and characteristic velocities u_w used in the lid-driven cavity simulations for different collision models at each Reynolds number.

Reynolds number Re	Collision model Ω	Grid size N	Velocity u_w
100	BGK	100	0.05
	TRT	100	0.08
	MRT	100	0.1
400	BGK	267	0.05
	TRT	200	0.06
	MRT	200	0.01
1000	BGK	667	0.05
	TRT	400	0.08
	MRT	400	0.1
3200	BGK	2134	0.05
	TRT	1000	0.1
	MRT	1000	0.1

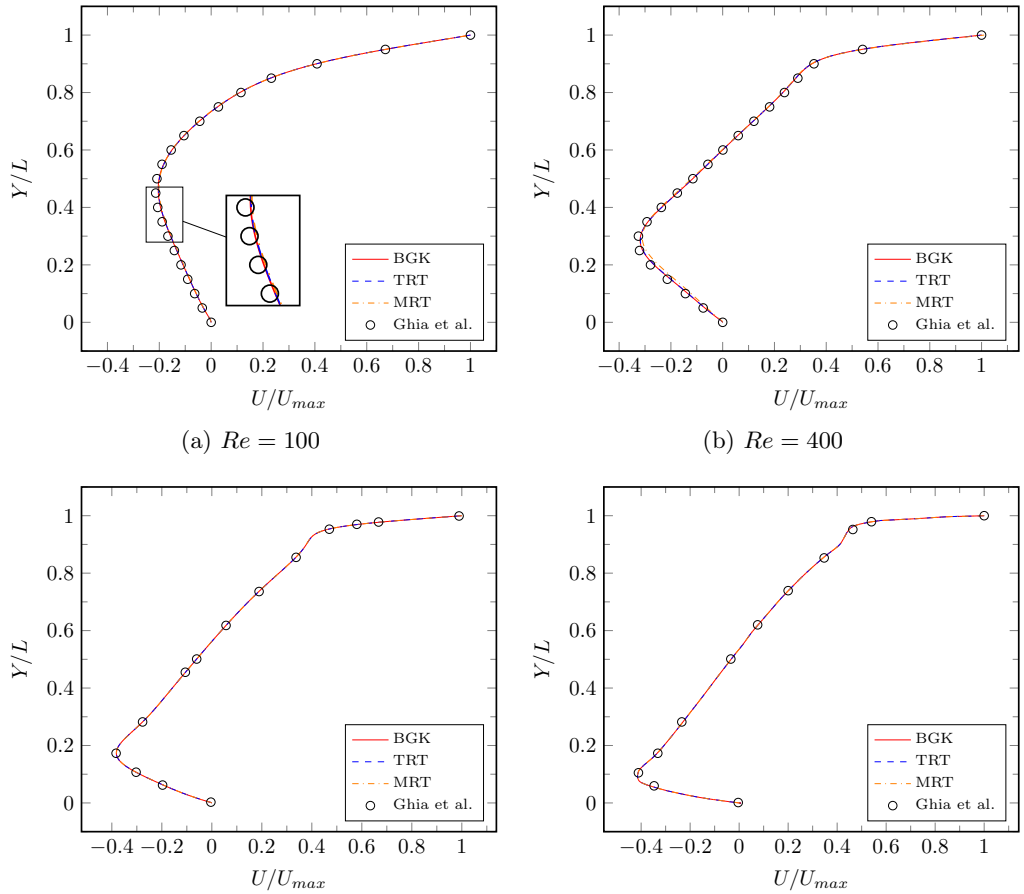
are no lattice nodes at the exact location of the boundary, the extrapolation of the velocity profile shown in Figure 4.6 leads to the numerical velocity slip at the boundary.

4.7 Effect of the Collision Operator

The BGK model is a simple and efficient way to simplify the collision operator in the LBE. However, the MRT and TRT collision operators offer a larger number of parameters that can be used to improve the accuracy and stability of the numerical method. The results for each collision operator are compared for different values of the Reynolds number, from $Re = 100$ to $Re = 3200$ in Figure 4.7 and Figure 4.8. Table 4.2 lists all the different parameters used in the simulations. The implementation of the TRT and MRT models for the collision operator is discussed in detail.

4.7.1 TRT Model

The TRT model requires two relaxation rates, one is related to the shear viscosity, and the other is a free parameter that can be tuned to improve the simulation performance. In this case, the value of the relaxation rate is fixed to $\omega^+ = 0.6$. A parametric analysis



(a) $Re = 100$ (b) $Re = 400$

(c) $Re = 1000$ (d) $Re = 3200$

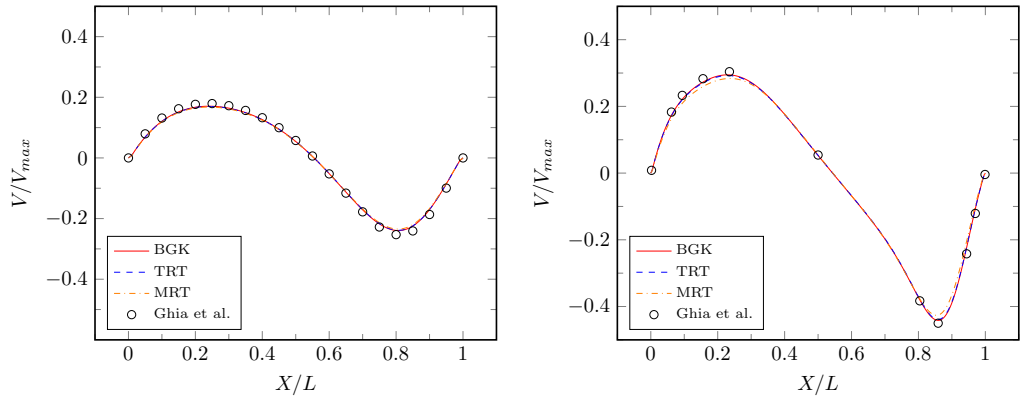
Figure 4.7: U-velocity profile along the central vertical line for the lid-driven cavity flow at increasing Reynolds numbers, comparing the BGK, TRT, and MRT collision operators.

is conducted on the magic parameter Υ to find the value that provides the best results in terms of accuracy and stability. Analytical studies prove that there are certain values of Υ that show distinctive properties [176, 177]

a. $\Upsilon = 0.25$ provides the most stable simulations.

b. $\Upsilon = 3/16$ implements the wall location exactly in the middle of the lattice link.

It is demonstrated that the value $\Upsilon = 0.25$ is the optimal choice in terms of stability and accuracy. Compared to the BGK model, the TRT scheme is stable for a wider range of relaxation times. Because the TRT model provides more flexibility on the stability



(a) $Re = 100$ (b) $Re = 400$

(c) $Re = 1000$ (d) $Re = 3200$

Figure 4.8: V-velocity profile along the central horizontal line for the lid-driven cavity flow at increasing Reynolds numbers, comparing the BGK, TRT, and MRT collision operators.

condition, a smaller domain size can be used. This decreases the computational costs, which become especially significant for high Reynolds number simulations. As Table 4.2 shows, for $Re = 3200$ the grid size used for the BGK model is more than double the size of the one used in the TRT scheme. The TRT collision operator decouples the stability condition and the kinematic viscosity. In this way, optimal stability can be achieved for any viscosity just by adjusting the free parameter such that $\Upsilon = 0.25$, while maintaining a constant Re. Since the most important parameter for controlling the accuracy is the relaxation time, the TRT model simplifies this process. If the viscosity is changed, then the only condition required to guarantee the same accuracy is to keep $\Upsilon = 0.25$ fixed by correspondingly adjusting the free parameter ω^-.

4.7.2 MRT Model

The MRT model is a more general and advanced collision operator. The most important benefit of this model is that it allows choosing the bulk viscosity ν_B independently of the shear viscosity ν. Unfortunately, the large number of user-defined relaxation parameters ω_α can only be chosen after some careful testing, as their optimal values are problem-specific. Recommended default values for the relaxation frequencies of the D2Q9 lattice model are [178]

$$\omega_\alpha = (0, 1.63, 1.14, 0, 1.92, 0, 1.92, \omega_\nu, \omega_\nu) \ , \tag{4.2}$$

where ω_ν is the relaxation parameter related to the shear viscosity ν and the relaxation time τ, as defined in Equation 3.18. These values provide a robust baseline for achieving stable simulations. The adjustable relaxation parameters are then systematically varied within their recommended range to determine a configuration optimised for the present flow problem [131, 179]. The set yielding the best agreement with the benchmark lid-driven cavity results is

$$\omega_\alpha = (0, 1.6, 1.2, 0, 1.6, 0, 1.6, 1.7, 1.7) \ . \tag{4.3}$$

Similarly to the TRT model, the MRT collision operator improves the stability so that a smaller domain size can be used, as shown in Table 4.2. However, the MRT model usually requires 15-20% more computational costs compared to the BGK and TRT operators [129].

4.8 Conclusions

This chapter considered the lid-driven cavity flow problem to demonstrate the numerical implementation of the LBM fluid solver and to evaluate the performance of different collision models. The lid-driven cavity flow is characterised by an increasingly complex behaviour for larger Reynolds number values. It is demonstrated that the LBM simulations with the BGK collision operator and fullway bounce-back conditions are capable of capturing the distinctive flow features, and the results for the velocity profile match

the reference simulations for the whole Reynolds number range.

The effect of the relaxation time is investigated for a range of values to understand its overall contribution to the numerical accuracy and stability. The simulations become unstable as the relaxation time increases, and it is shown that a larger numerical domain is required to achieve stable results. Additionally, the solution depends on the value of the relaxation time, and the simulations are viscosity-dependent with a decreasing accuracy for larger relaxation time values.

The halfway bounce-back scheme is tested and compared to the fullway condition to discuss the limitations of the most common boundary conditions. It is shown that the halfway bounce-back scheme used together with the BGK collision model is characterised by a viscosity-dependent slip velocity at the boundary. This numerical error is due to the exact location of the no-slip boundary being dependent on the value of the relaxation time. It is discussed that there is only one value of the relaxation time that achieves the no-slip condition at the exact location of the boundary, resulting in significant drawbacks for this method.

The influence of different collision operators on the simulations is investigated to evaluate their potential. The TRT model provides an easy-to-use parameter to optimise stability and accuracy. Due to the implementation of the magic parameter, the TRT scheme is stable for a wider range of relaxation times compared to the BGK model. Therefore, smaller domain sizes are able to achieve stable results, and the computational costs decrease. The MRT model offers a larger number of parameters that can be tuned to improve accuracy and stability. Additionally, it allows choosing the bulk viscosity independently of the shear viscosity. However, the optimal values of the parameters depend on the specific problem and require tuning.

This chapter demonstrated the validity of the implemented fluid solver, while insights from the performance of the different collision operators informed the selection of more advanced schemes. In particular, the CMLB is adopted in the subsequent chapters to further enhance accuracy and stability for fluid-structure configurations.

Chapter 5

Numerical Diffusion in Confined Flow Problems

5.1 Introduction

Generally, IBM approaches implement a diffuse representation of the fluid-solid interface, which suppresses numerical oscillations significantly compared to sharp-interface methods. However, the diffuse interface might reduce the accuracy of the flow field around the solid boundary. The aim of this chapter is to investigate the diffusive effects associated with the present IBM implementation and quantify their impact on numerical accuracy by comparison with sharp-interface approaches. In addressing this problem, the chapter provides insight into the competing effects of accuracy and stability in different boundary representations. A boundary retraction scheme is developed within the current IB–LBM framework with the objective of reducing the diffusive effects related to the IBM formulation, and its effectiveness is examined across a range of representative test problems of increasing complexity. Through this analysis, the study demonstrates the limits of diffuse-interface IBM implementations and develops a corrective strategy that effectively restores accuracy.

This chapter is based on previously published work [180]. The analysis was conceived and designed in collaboration with the co-authors, who further contributed through scientific discussion and editorial feedback. Dedicated code was developed and imple-

mented within the existing IB–LBM framework [159] for the purposes of this study.

Section 5.2 outlines the numerical challenges associated with diffuse-interface immersed boundary formulations and motivates the need for a boundary-retraction strategy. Section 5.3 introduces the boundary-retraction scheme and its integration into the IB–LBM solver. The numerical methodology and simulation setup are described in Section 5.4. The performance of the approach is then investigated for different test cases: flow past a cylinder (Section 5.4.1), sedimentation of a single particle (Section 5.4.2), flow around two impacting particles (Section 5.4.3), and the drafting–kissing–tumbling problem (Section 5.4.4). Finally, Section 5.5 summarises the findings and discusses their broader implications.

5.2 Problem Statement

In IBM schemes, the Eulerian grid and Lagrangian marker points exchange information through velocity interpolation and force distribution. The operations between the different node systems are based on discrete delta functions, which diffuse the interface around the solid boundary to limit numerical oscillations [154]. However, interpolation stencils involving discrete delta functions formally introduce a first-order error term in the velocity field [108, 148, 154, 181, 182]. Another consequence of the diffuse interface is the *effective thickness* of the fluid-solid boundary, which changes the apparent size of solid objects and surface locations [61, 183–186]. The diffusive effect becomes increasingly significant for confined flows and particle collisions, which are common features for particulate flows.

In contrast to the diffuse-interface IBM, in the LBM framework there are several methods that feature a sharp representation of the interface as a fluid-solid boundary treatment. The most common strategies are the simple and interpolated bounce-back methods [143, 149], which suffer from spurious numerical oscillations for moving boundary problems. The PSM presented by Noble and Torczynski [150] is a modified bounce-back approach that allows for a sharp reconstruction of the boundary by representing lattice nodes as pure fluid, pure solid, and mixed nodes depending on a weighting pa-

rameter. To improve the accuracy of this sharp-interface method, Chen et al. [187] combined it with a ghost method that introduces virtual nodes within the solid object to extrapolate fluid properties.

The method presented in the work of Tsigginos et al. [152] (see Section 3.2.8) achieves second-order accuracy by modelling fluid-particle interaction as a two-phase mixture. The solid objects are represented as virtual fluids, and the computational nodes are identified as pure fluid, pure virtual fluid, and partially saturated based on their solid fraction. The fluid–solid coupling is handled through momentum exchange schemes, i.e. MES-I and MES-II. In MES-I, the momentum transfer from the solid to the virtual fluid is fully enforced only at solid nodes, while at partially saturated nodes the imposed velocity also depends on the surrounding fluid velocity. MES-II refines this approach by directly enforcing the solid velocity on both virtual and partially saturated nodes, leading to a more consistent interface treatment. However, accurate calculation of the solid fraction is crucial to correctly represent complex fluid-solid interfaces. Therefore, this method introduces a significant computational cost for moving boundary problems as the solid fraction needs to be updated at every time step. Because of their accuracy, the results presented in Ref. [152] are considered in this work to evaluate the performance of the diffuse-interface IBM.

The main focus of this study is to investigate the diffuse-interface effects for particulate flows with no geometrical confinement, fixed and variable confinements, in addition to particle interactions and collisions. The results are compared to experimental data in Ref. [188], analytical formulations, and the results of sharp-interface methods in Ref. [152, 189]. The effects of the diffuse interface are systematically analysed, and the implementation of a boundary retraction scheme is considered as a mitigation strategy.

Another important aspect of particle interaction is the role of lubrication forces in near-contact dynamics. When two surfaces move relative to each other in a fluid and the gap between them becomes sufficiently small, a strong hydrodynamic resistance develops in the fluid film. This short-range lubrication force governs the hydrodynamic interaction between approaching particles and between particles and walls [190, 191]. Classical lubrication theory indicates that this force becomes singular as the gap approaches zero,

effectively preventing smooth surfaces from coming into physical contact [189]. In IB-LBM simulations, the near-contact interactions are numerically challenging because the fluid gap size is comparable to the lattice grid spacing, and the diffuse interface further reduces the effective gap. When the gap becomes smaller than one lattice spacing, fluid nodes are excluded, and the flow in the fluid film is unresolved. The breakdown of lubrication forces in the calculation of hydrodynamic interactions results in underpredicted forces and altered particle approach dynamics [2, 192, 193]. Lubrication breakdown is typically addressed by adding force corrections for unresolved gaps, which restore the hydrodynamic resistance without grid refinement [165, 191–193]. In the present work, lubrication corrections are not applied, and the effects of lubrication breakdown in short-range particle interactions are examined. In addition, the influence of the diffuse interface on near-contact dynamics is evaluated to establish its role in these interactions.

5.3 Boundary Retraction Scheme

The interpolation and distribution procedures described respectively in Equation 3.52 and Equation 3.63 are the source of the diffusive effects due to the implementation of discrete delta functions [148]. To take advantage of IBM while alleviating the diffuse interface effects on the flow field, Breugem [108] suggested correcting the effective diameter of immersed objects by retracting the Lagrangian interface grid points some distance inside the solid surface. It is shown that this strategy partly cancels the interpolation errors and improves the simulation accuracy significantly. Additionally, the retraction distance is affected by the solid object geometry, and the optimal values for spheres, tubes and cubes are provided. Since discrete delta functions used in IBM have different interpolation ranges, the effective boundary thickness is also affected by the choice of kernel function.

The work of Peng et al. [148] tested the boundary retraction approach for different discrete delta functions and concluded that the optimal distance value is larger for more diffusive functions. Furthermore, Peng and Wang [182] derived an analytical demonstration of the optimal retraction distance for a plane channel flow. However,

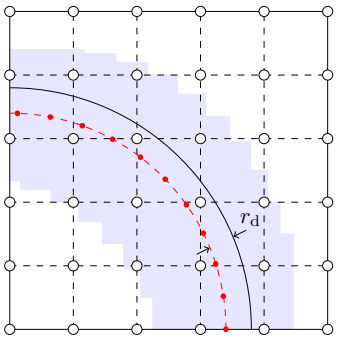


Figure 5.1: Representation of the fluid-solid boundary. The Lagrangian points indicated by red dots are retraced inwards by a distance r_d. The range of action of the discrete delta functions is represented by the light blue shaded area.

for surface-confined particulate flows particularly with inter-particle collisions, further work is required to understand the extent to which the diffuse interface affects simulation accuracy and to improve the boundary retraction approach accordingly.

The boundary retraction scheme implemented in the present work mitigates the diffuse-boundary effect caused by the discrete delta functions by modifying the position of the Lagrangian points. This approach is reflected in the way that the IB-LBM algorithm updates the position and velocity of the Lagrangian points.

Figure 5.1 schematises the representation of a solid object according to the current IBM implementation. The support lattice nodes required for the interpolation and distribution operations are defined by the choice of delta function and they determine the smoothness of the boundary representation. In the boundary retraction algorithm, the Lagrangian points are retracted inwards by a distance r_d. In the following section, the effectiveness of this strategy is evaluated for increasingly complex problems. Different values of retraction distance r_d are tested to investigate their impact on numerical errors. Additionally, the effects of geometrical confinement, particle interaction and collision are examined.

5.4 Numerical Simulations

In contrast to sharp-interface approaches, the accuracy of the IB-LBM scheme deteriorates quickly as particulate flow becomes more confined due to the diffusive boundary

Table 5.1: Geometry and fluid properties for unconfined flow past a cylinder.

Geometry		Parameters	
Diameter D	1	Density ρ_f	1
Square domain width L	50	Viscosity μ_f	0.001

effect. To alleviate this, the simple but effective boundary retraction scheme is applied in the following. The performance is evaluated in four cases: flow past a cylinder, settling of a particle under gravity, flow around two impacting particles, and the drafting-kissing-tumbling process of two particles settling in a channel. These test cases are arranged to show how the diffusive effect of IBM influences flows with very different confinements and to examine the effectiveness of the boundary retraction scheme. The simulation results are be compared with experimental data, and the numerical results obtained with the sharp-interface approach in Ref. [152].

All simulations are performed on a uniform lattice using the D2Q9 velocity set. The collision operator is defined using the CLBM, and the IBM formulation is based on a four-point regularised discrete delta function.

5.4.1 Flow Past a Cylinder

The flow past a stationary circular cylinder in a two-dimensional channel is used to test the performance of the IB-LBM scheme for fixed boundary problems in both confined and unconfined geometries.

Unconfined Flow

The stationary circular cylinder of diameter D is positioned at the centre of a square of size L. A fixed constant velocity u_i is prescribed at the inlet, top and bottom boundaries, while a pressure boundary condition is imposed at the outlet. The results from extensive experiments of Tritton [188] and the sharp-interface approach of Tsigginos et al. [152] are employed for a quantitative comparison.

The geometry parameters and fluid properties listed in Table 5.1 are normalised in the same way as Tsigginos et al. [152] for consistent comparison. The Reynolds number

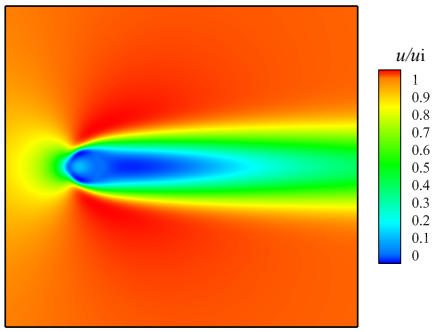


Figure 5.2: Unconfined flow past a cylinder: contours of the dimensionless horizontal velocity u/u_i at $Re = 40$.

is increased from 1 to 40 by varying the inlet velocity u_i according to the equation $Re = \rho_\mathrm{f} u_\mathrm{i} D/\mu_\mathrm{f}$, where ρ_f and μ_f are respectively the density and the dynamic viscosity of the fluid. The drag coefficient C_d is calculated from

$$C_\mathrm{d} = \frac{2F}{\rho_\mathrm{f} u_\mathrm{i}^2 D}\,. \tag{5.1}$$

A lattice size $\Delta x = D/30$ is used in the current case as it was demonstrated to be sufficiently accurate [152].

The dimensionless horizontal velocity u/u_i is displayed in Figure 5.2. The calculated drag coefficients C_d for different Re values are plotted in Figure 5.3, showing a good agreement with both the experimental data [188] and the numerical results [152]. Therefore, for the unconfined flow above, the diffuse interface does not lead to significant numerical error, and the boundary retraction scheme is not required.

Confined Flow and Wall Interaction Effects

The flow past a cylinder of diameter D in a channel of width W and length L is simulated to investigate the confinement effect on the flow behaviour in the creeping laminar flow regime, where the bounding walls of the channel alter the characteristic features of the flow field. The channel confinement ratio $\kappa = D/W$ is the characteristic parameter for measuring the extent of confinement, with $\kappa > 0$ corresponding to confined flow and $\kappa \to 0$ representing the unbounded flow limit. This classical case has been studied extensively and detailed descriptions of the available analytical studies, computational

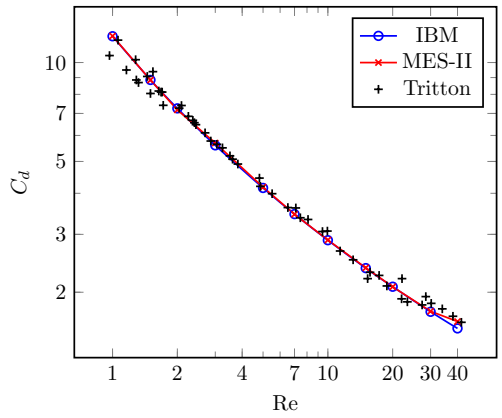


Figure 5.3: Drag coefficient C_d for unconfined flow past a cylinder at different Reynolds numbers Re. Experimental results from Tritton [188] and MES-II numerical results in Ref. [152] are given for comparison.

simulations and experiments have been presented in several works, e.g. Refs. [194–197].

The computational domain geometry and the fluid field are displayed in Figure 5.4. A parabolic velocity profile with a maximum speed of u_m is imposed at the inlet and outlet boundaries. No-slip boundary conditions are applied at the top and bottom channel walls with the halfway bounce-back scheme. The geometry and fluid properties used in the simulations are listed in Table 5.2.

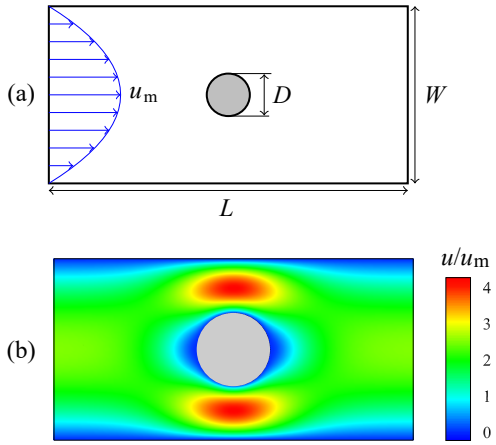


Figure 5.4: Flow past a fixed cylinder: (a) schematics of the computational domain and (b) contours of the dimensionless horizontal velocity u/u_m.

For the current flow past a cylinder in the creeping laminar flow regime, the wall effect on the drag force can be estimated using a *wall correction factor* λ, which is

defined as

$$\lambda(\kappa) = \frac{F_{\mathrm{d}}(\kappa)}{u_{\mathrm{m}}\mu_{\mathrm{f}}}, \tag{5.2}$$

where F_{d} is the drag force, and μ_{f} is the fluid viscosity. As one of the most common expressions for the wall correction factor that can offer an accurate analytical solution for Stokes flow, the wall correction factor λ_{F} derived by Faxén [152] is expressed in the form [152, 194]

$$\lambda_{\mathrm{F}}(\kappa) = \frac{4\pi}{f(\kappa) + g(\kappa)}, \tag{5.3}$$

where $f(\kappa)$ and $g(\kappa)$ are defined as

$$\begin{aligned} f(\kappa) &= A_0 - \left(1 + 0.5\,\kappa^2 + A_4\,\kappa^4 + A_6\,\kappa^6 + A_8\,\kappa^8\right)\ln(\kappa)\,, \\ g(\kappa) &= B_2\,\kappa^2 + B_4\,\kappa^4 + B_6\,\kappa^6 + B_8\,\kappa^8\,, \end{aligned} \tag{5.4}$$

and the corresponding numerical coefficients are

$$\begin{aligned} A_0 &= -0.9156892732\,, & B_2 &= 1.26653975\,, \\ A_4 &= 0.05464866\,, & B_4 &= -0.9180433\,, \\ A_6 &= -0.26462967\,, & B_6 &= 1.8771010\,, \\ A_8 &= 0.792986\,, & B_8 &= -4.66549\,. \end{aligned}$$

This expression is valid for confined flows with $0 < \kappa \leq 0.5$ [194]. To evaluate the performance of the IB-LBM scheme, the calculated wall correction factor λ is compared to the Faxén wall correction factor λ_{F}. The numerical error E_λ is given by the expression,

$$E_\lambda = \left|\frac{\lambda - \lambda_{\mathrm{F}}}{\lambda_{\mathrm{F}}}\right|. \tag{5.5}$$

Simulations are performed for different lattice sizes, i.e. $\Delta x = (D/12,\, D/16,\, D/20,\, D/30,\, D/40)$ to show the effect of the computational grid. The corresponding numerical error E_λ with $\kappa = 0.4$ is plotted in Figure 5.5 and compared to the results in Ref. [152]. As Figure 5.5 shows, the simulation results' accuracy increases drastically for a larger lattice resolution. Importantly, the accuracy of the present simulation is comparable

Table 5.2: Geometry and fluid properties for confined flow past a cylinder.

Geometry		Parameters	
Diameter D	1	Density ρ_f	1
Channel width W	2.5	Viscosity μ_f	0.005
Channel height H	40	Velocity u_m	10^{-6}
Confinement ratio κ	0.4	Reynolds number Re	2×10^{-4}

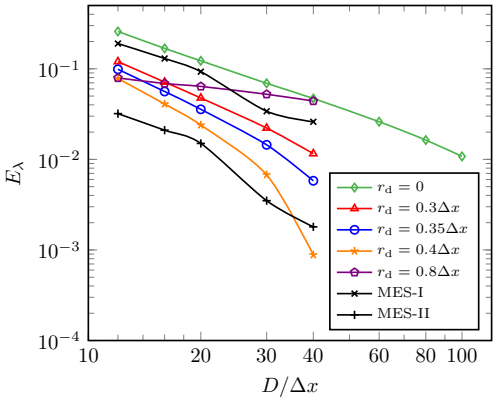


Figure 5.5: Confined flow past a cylinder: wall correction factor error E_λ for confinement ratio $\kappa = 0.4$, comparing different retraction distances r_d. The numerical results (MES-I, MES-II) reported in Ref. [152] are given for comparison.

to the MES-I scheme, but it is less accurate than the second-order algorithm MES-II. It seems that the diffuse interface in the highly confined geometry ($\kappa = 0.4$) has a more significant impact on the performance of the IB-LBM scheme compared to sharp-interface methods, including MES-I and MES-II.

The approach of retracting the Lagrangian surface grid points is applied to the simulations with the retraction distance $r_d = (0, 0.3, 0.35, 0.4)\Delta x$, where the case with $r_d = 0$ does not include boundary retraction. As displayed in Figure 5.5, the wall correction factor error E_λ decreases considerably as r_d grows. The error E_λ with $r_d = 0.35\Delta x$ decreases significantly from 4.7% to 0.58% for the lattice size $\Delta x = D/40$ and from 26% to 9.9% for $\Delta x = D/12$. It can also be noted that retracting the Lagrangian points by $r_d = 0.4\Delta x$ for lattice size $\Delta x = D/40$ makes the results even more accurate than the ones for $\Delta x = D/100$ without retraction. The above results suggest an appropriate $r_d = 0.4\Delta x$, which is close to the optimal value suggested by Breugem [108] and Peng et al. [182]. Additionally, a larger retraction distance

$r_\mathrm{d} = 0.8\Delta x$ is also considered in Figure 5.5. It is clear that $r_\mathrm{d} = 0.8\Delta x$ performs significantly worse.

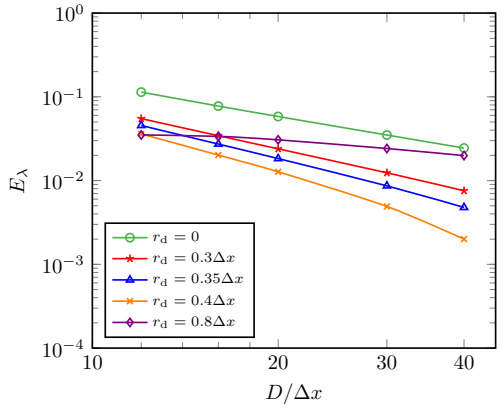


Figure 5.6: Confined flow past a cylinder: wall correction factor error E_λ for confinement ratio $\kappa = 0.2$, comparing different retraction distances r_d.

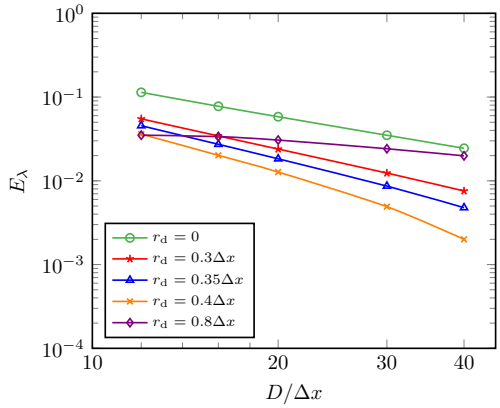


Figure 5.7: Confined flow past a cylinder: wall correction factor error E_λ for confinement ratio $\kappa = 0.1$, comparing different retraction distances r_d.

Since a larger degree of confinement accentuates interface diffusion in the IB-LBM simulations, it is interesting to compare the results of different confinement ratios $\kappa = (0.1, 0.2, 0.4)$, where the corresponding channel widths W are (10, 5, 2.5). By comparing the cases in Figures 5.5, 5.6 and 5.7, it can be seen that the wall correction factor error E_λ becomes much smaller as the confinement ratio κ decreases. Specifically for lattice size $\Delta x = D/40$, when the confinement ratio κ is reduced from 0.4 to 0.1, the error E_λ for cases without retraction decreases from 4.7% to 1.5%, while E_λ for cases with

$r_\mathrm{d} = 0.35\Delta x$ reduces from 0.58% to 0.3%.

As demonstrated in Figures 5.5, 5.6 and 5.7, the interface diffusion effect can be compensated successfully by applying different retraction distances, $r_\mathrm{d} = (0.3, 0.35, 0.4)\Delta x$. To be specific, as the retraction distance r_d grows from zero to $0.4\Delta x$, in Figure 5.6 with $\kappa = 0.2$, the error E_λ reduces from 2.4% to 0.2% for lattice sizes $\Delta x = D/40$ respectively, while in Figure 5.7 with $\kappa = 0.1$, E_λ decreases from 1.5% to 0.13% for $\Delta x = D/40$. However, the retraction distance $r_\mathrm{d} = 0.8\Delta x$ makes the accuracy of the IBM much worse for all the tested confinement ratios κ. Therefore, the boundary retraction strategy is competitive in reducing computational cost while maintaining simulation accuracy, as long as an appropriate retraction distance is used.

5.4.2 Sedimentation of a Single Particle Under Gravity

The case of a cylindrical particle settling under gravity in a two-dimensional channel is simulated to investigate confined flow with moving boundaries in the creeping laminar flow regime. In addition to approximate analytical formulations [152], this problem has been investigated by various numerical and experimental studies, and extensive benchmark results are available [194, 198–203].

As represented in Figure 5.8, the problem geometry is schematised by a vertical channel of width W and height H. The computational domain is bounded by solid walls, and a no-slip boundary condition is implemented using a halfway bounce-back scheme. The initial geometry and fluid flow conditions used in the simulations are listed in Table 5.3. A cylindrical particle of diameter D initially at rest is released along the centreline of the channel. As the particle starts moving downwards under the action of gravity, the drag force exerted by the surrounding fluid increases. Once the drag force balances the gravitational force, the particle settles with a constant velocity known as the *terminal velocity* V_t.

Because of the interaction with the walls, the settling velocity is lower than the corresponding one in the unconfined flow case [41, 200, 203]. A wall correction factor λ_F is introduced to account for the effect of the bounded geometry. By balancing the gravitational force $F_\mathrm{g} = \left(\pi\, g D^2 \left(\rho_\mathrm{s} - \rho_\mathrm{f}\right)\right)/4$ and the drag force acting on the particle

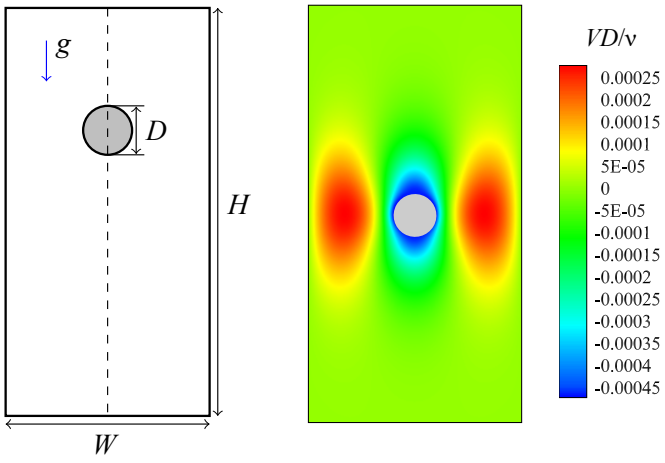


Figure 5.8: Sedimentation of a particle under gravity: (a) schematics of the computational domain and (b) contours of the vertical velocity V.

Table 5.3: Particle and fluid properties for sedimentation of a particle under gravity.

Geometry		Parameters	
Diameter D	1	Density ρ_f	1
Channel width W	5	Viscosity μ_f	0.005
Channel height H	80	Particle density ρ_s	2.6
Confinement ratio κ	0.2	Reynolds number Re	5×10^{-4}

$F_\mathrm{d} = \lambda_\mathrm{F}\, \mu_\mathrm{f}\, V_\mathrm{t}$, the wall-corrected terminal velocity of a settling particle can be estimated as [152, 203]

$$V_\mathrm{t} = \frac{\pi g D^2 \left(\rho_\mathrm{s} - \rho_\mathrm{f}\right)}{4 \mu_\mathrm{f} \lambda_\mathrm{F}\left(\kappa\right)}\,, \tag{5.6}$$

where ρ_s is the particle density, g is the gravitational acceleration, and λ_F is the Faxén wall correction factor. For this case, the Faxén wall correction factor is calculated as [152, 204]

$$\lambda_\mathrm{F} = \frac{4\pi}{A_0 - \ln\left(\kappa\right) + A_2\,\kappa^2 + A_4\,\kappa^4 + A_6\,\kappa^6 + A_8\,\kappa^8}\,, \tag{5.7}$$

where κ is the channel confinement ratio and the numerical coefficients are $A_0 = -0.9156892732$, $A_2 = 1.7243844$, $A_4 = -1.730194$, $A_6 = 2.405644$, and $A_8 = 4.59131$. The gravitational acceleration value g is calculated using Equation 5.6 to match the specified value of the Reynolds number $Re = \rho_\mathrm{f} V_\mathrm{t} D / \mu_\mathrm{f}$, where V is the numerical value of the terminal velocity. As the terminal velocity V_t can be accurately calculated by

Equation 5.6, it is used to evaluate the numerical velocity error E_{v} in the diffusive IB-LBM scheme as follows,

$$E_{\mathrm{v}} = \left| \frac{V - V_{\mathrm{t}}}{V_{\mathrm{t}}} \right| . \tag{5.8}$$

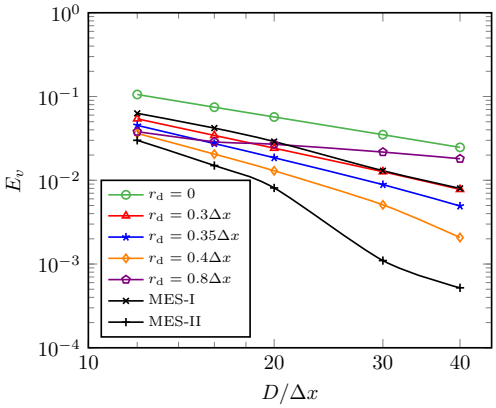


Figure 5.9: Sedimentation of a particle under gravity: velocity error E_{v} for confinement ratio $\kappa = 0.2$, comparing different retraction distances r_{d}. The numerical results in Ref. [152] are given for comparison.

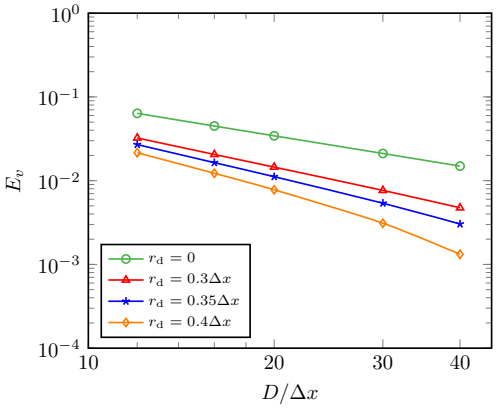


Figure 5.10: Sedimentation of a particle under gravity: velocity error E_{v} for confinement ratio $\kappa = 0.1$, comparing different retraction distances r_{d}.

Simulations are run for different lattice sizes, i.e. $\Delta x = (D/12,\ D/16,\ D/20,\ D/30,\ D/40)$. The calculated E_{v} for different lattice sizes is illustrated in Figure 5.9 and compared to the numerical results of the sharp-interface method reported in Ref. [152]. The boundary retraction scheme with distance $r_{\mathrm{d}} = (0.3, 0.35, 0.4)\Delta x$ is applied to

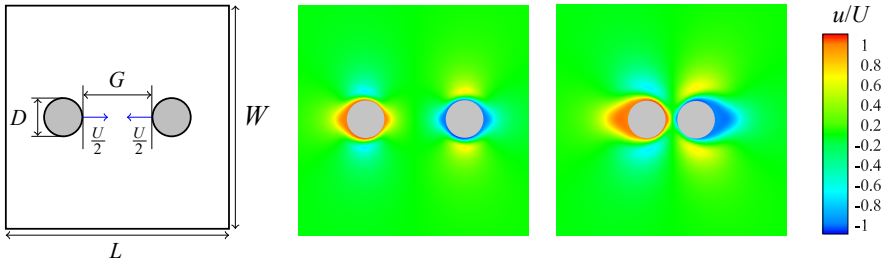
alleviate the diffusive effects. Figure 5.9 shows that the velocity error E_v decreases significantly when the boundary retraction approach is used. It can be estimated that the velocity error E_v for retraction distance $r_d = 0.4\Delta x$ decreases from 11% to 3.6% for the lowest resolution case $\Delta x = D/12$ and from 2.5% to 0.21% for lattice size $\Delta x = D/40$. The IB-LBM with retracted interface shows a better performance compared to the MES-I scheme, but the accuracy is still lower than the second-order MES-II model.

To investigate the effect of confinement, the particle sedimentation case is simulated in a wider computational domain with the confinement ratio $\kappa = 0.1$. The values of velocity error E_v for lattice sizes $\Delta x = (D/12, D/16, D/20, D/30, D/40)$ and the retraction distance $r_d = (0, 0, 3, 0.35, 0.4)\Delta x =$ are shown in Figure 5.10. As observed in Figure 5.10, the terminal velocity error E_v for the case of $r_d = 0.4\Delta x$ is reduced from 1.5% to 0.13% for $D = 40\Delta x$ and from 6.4% to 2.2% for $D = 12\Delta x$. Moreover, it can be noted that due to the less significant confinement effect, the error E_v for $r_d = 0.4\Delta x$ in comparison to its corresponding case in Figure 5.9 decreases from 3.6% to 2.2% and from 0.21% to 0.13% for $D = 12\Delta x$ and $D = 40\Delta x$, respectively. In this case, the retraction distance $r_d = 0.4\Delta x$ still shows the best accuracy.

5.4.3 Flow Around Two Impacting Particles

The test case of flow around two impacting cylindrical particles in a two-dimensional channel has been chosen to investigate the effect of diffuse interface for moving objects with a variable confinement and considering the interaction between particles where two diffuse interfaces could overlap. This problem has been studied by Bampalas and Graham [205] using a finite element method with a body-fitted mesh.

The computational domain used for the simulations is a channel of width W and length L, as illustrated in Figure 5.11a. Two identical particles of diameter D are placed at the centre of the channel with an initial horizontal separation G. The fluid is initially stationary, and the particles are moving towards each other along the centreline of the channel with the same velocity $U/2$. The computational domain is bounded by four stationary walls, where a gradient boundary condition is imposed. Geometry and fluid properties used in this case are the same as in Ref. [152], which are listed in Table 5.4.



(a) (b) (c)

Figure 5.11: Flow around two impacting cylinders: (a) schematics of the computational domain and (b) contours of the horizontal velocity U at $t^* = -1$; and (c) $t^* = -0.1$.

Figures 5.11b and 5.11c show the velocity contours at different instants, where the normalised time t^* is defined by the following expression [152, 205],

$$t^* = \frac{U\,t - G}{D}\,, \tag{5.9}$$

where U is the relative velocity of the particles.

Table 5.4: Particle and fluid properties for flow around the two impacting particles.

Geometry		Parameters	
Diameter D	1	Density ρ_{f}	1
Channel width W	50	Viscosity μ_{f}	0.0015
Channel height H	50	Velocity U	0.15
Initial gap G	2	Reynolds number Re	50

Simulations are carried out for different lattice sizes, i.e. Δx =($D/12$, $D/30$, $D/60$, $D/80$). Figure 5.12 presents the evolution in time of the drag coefficient C_{d} for the different computational grids. As shown in Figure 5.12, the accuracy of the IB-LBM model improves significantly by increasing the lattice resolution from $D = 12\Delta x$ to $D = 30\Delta x$, which is favoured. However, in spite of the great computational cost when increasing the lattice grid refinement to $D = 60\Delta x$ and $D = 80\Delta x$, the error on the drag coefficient C_{d} can hardly be much smaller.

The numerical error on the drag coefficient C_{d} appears to be related to the interface diffusion effect associated with the IBM model. Considering Figure 5.11, it is evident that as the particles approach each other, the diffuse interface has an increasingly sig-

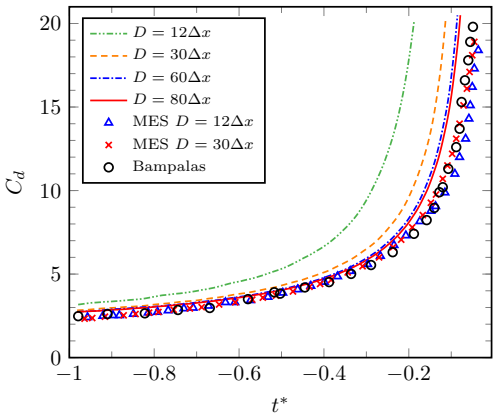
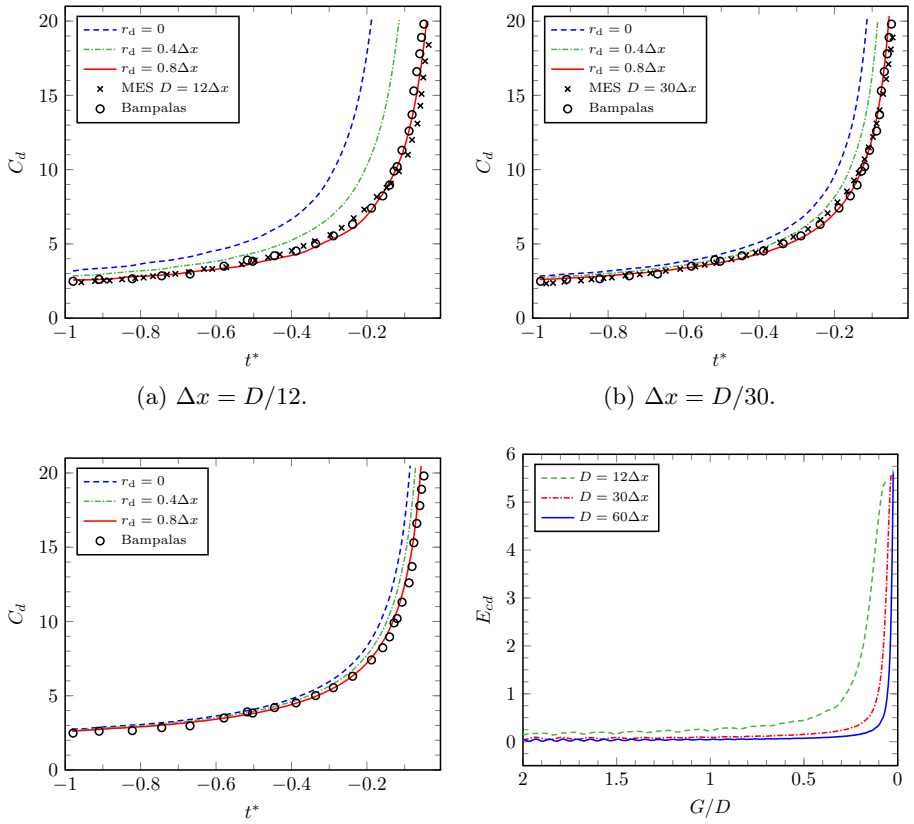


Figure 5.12: Drag coefficient C_d evolution in time for the flow around two impacting cylinders, comparing different lattice resolutions. The numerical results in Ref. [152] (MES) and Ref. [205] (Bampalas) are given for comparison.

nificant impact on the results. Therefore, the boundary retraction approach is used to minimise the interface diffusion effect and improve simulation accuracy. The impact of this strategy can be visualised in Figure 5.13 for three different grid resolutions, i.e. $D = (12, 30, 60)\Delta x$. It is evident that the results obtained using the boundary retraction scheme show a much closer match to the ones presented in Ref. [152, 205]. The difference between the drag coefficient C_d values for $r_\mathrm{d} = 0$ and $r_\mathrm{d} = 0.8\Delta x$ can be quantified by calculating the relative difference E_Cd. Figure 5.13 shows the evolution of E_Cd as a function of the separation distance G/D between the particles for $D/\Delta x = [12,\ 30,\ 60]$. Initially, the drag coefficient C_d values for $r_\mathrm{d} = 0$ and $r_\mathrm{d} = 0.8\Delta x$ are similar and E_Cd is negligible. As the separation distance G/D between the particles is progressively reduced, the results for $r_\mathrm{d} = 0$ and $r_\mathrm{d} = 0.8\Delta x$ diverge and E_Cd becomes significant. In particular, when the separation distance G becomes smaller than $4\Delta x$, the diffuse interfaces start to overlap, and the numerical error for the drag coefficient C_d grows exponentially. As shown in Figure 5.13, although the retraction distance $r_\mathrm{d} = 0.4\Delta x$ works well for single-particle problems, a much larger retraction distance is needed, i.e. $r_\mathrm{d} = 0.8\Delta x$ when the interaction between different diffuse interfaces becomes much stronger.

In addition to diffuse-interface effects, the near-contact interactions between the two particles are also influenced by lubrication forces, which are important to understand the



(a) $\Delta x = D/12$. (b) $\Delta x = D/30$.

(c) $\Delta x = D/60$. (d) E_{Cd}.

Figure 5.13: Flow around two impacting cylinders: effect of the diffuse-interface on the drag coefficient C_{d} evolution in time for lattice sizes: (a) $\Delta x = D/12$, (b) $\Delta x = D/30$, and (c) $\Delta x = D/60$. The numerical results in Ref. [152] (MES) and Ref. [205] (Bampalas) are given for comparison. (d) Drag coefficient difference E_{Cd} as a function of the separation distance between the particles G/D.

need for a larger retraction distance. Lubrication theory predicts that the hydrodynamic resistance to relative motion between two approaching particles increases sharply as the gap between them decreases. However, in the IB-LBM framework with diffuse interfaces, the fluid film cannot be fully resolved once the gap size becomes comparable to the lattice spacing. The diffuse interface further reduces the effective gap, leading to incomplete resolution of the film layer and an underestimation of lubrication forces. Consequently, the hydrodynamic resistance predicted by lubrication theory is not captured accurately, and this limitation is amplified when diffuse interfaces overlap, as this representation alters the near-contact dynamics. Increasing the retraction distance compensates for

Table 5.5: Particle and fluid properties for sedimentation of two particles.

Geometry		Parameters	
Diameter D	0.2	Density ρ_f	1
Channel width W	2	Viscosity μ_f	0.08
Channel height H	6	Particle density ρ_s	1.1
Initial gap G	0.3	Gravitational acceleration g	981
Initial separation S	0.006	Spring coefficient k_n	2500
		Damping coefficient c_n	0.4

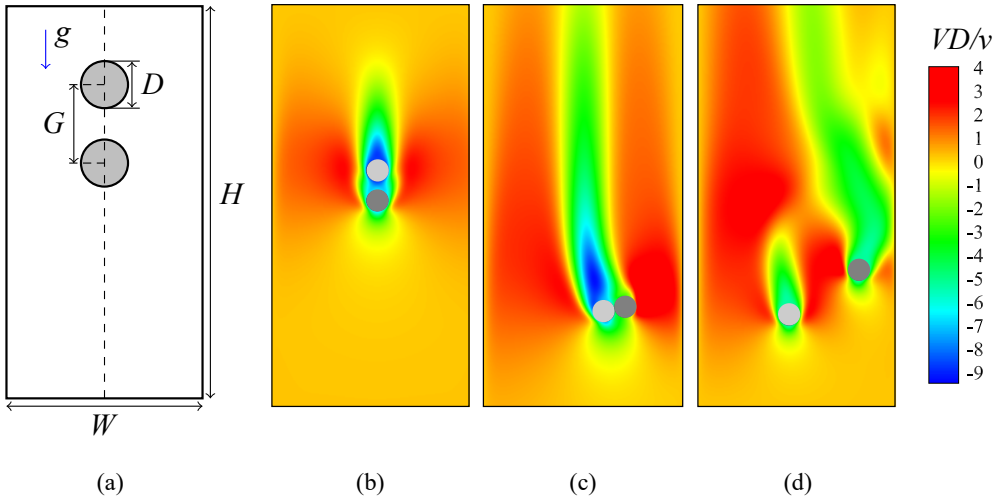


Figure 5.14: Drafting-kissing-tumbling of two particles settling in a channel under gravity: (a) computational domain, contours of the vertical velocity V at (b) $t = 0.4$, (c) $t = 0.8$, and (d) $t = 1.2$.

interface overlap and the unresolved lubrication layer, improving the resolution of short-range particle interactions.

5.4.4 Drafting-Kissing-Tumbling Process of Two Particles Settling

The sedimentation of two circular cylindrical particles in a two-dimensional channel is considered to investigate moving boundary problems with a variable confinement. Since this test case involves a close interaction including collision between the falling particles, the diffuse interfaces could have a significant influence on their movement.

The fundamental mechanism associated with pairwise coupling of particles settling in a channel was first described by Fortes et al. [206] who performed experiments on

spherical particles in fluidised beds. Significant work has been conducted to investigate this problem using various lattice Boltzmann models [207–209] and different IBM schemes [41, 45, 210]. As shown in Figure 5.14, the computational domain is geometrically represented by a vertical channel of width W and height H. Two identical particles of diameter D are placed along the centreline of the channel with an initial vertical separation G. The trailing particle is initially displaced off-centre with a horizontal separation distance from the centreline S. Non-slip boundary conditions are prescribed at the channel walls by applying a halfway bounce-back scheme. The computational domain geometry and fluid flow conditions used in the simulations are listed in Table 5.5, and these values are the same as Ref. [189]. Two particles settling in close proximity in a channel under gravity undergo a typical sequence of movements, known as the *drafting-kissing-tumbling* (DKT) process, which can be visualised in Figure 5.14. After the particles are released, the trailing particle is caught in the wake of the leading particle and it experiences a reduction in its drag force. In the *drafting* part of the process, the trailing particle velocity increases and it starts to fall faster than the leading one. The trailing particle eventually catches up with the leading one in the *kissing* stage, when the particles are in contact. Because this configuration is unstable, the trailing particle rotates around the leading one and overtakes it in a *tumbling* movement.

Since the DKT process involves a contact stage, the IB-LBM implements the discrete element method to handle collisions between particles. In the soft-sphere approach used, the interaction between particles is approximated by constructing the contact force as a function of the overlap and the relative velocity at the contact point. A linear spring-dashpot model is applied to both particle-particle and particle-wall interactions when the distance is less than the critical value ε_c. The contact force $\mathbf{F}_\mathrm{c}$ can be decomposed into normal F_cn and tangential F_ct terms that are respectively calculated as follows,

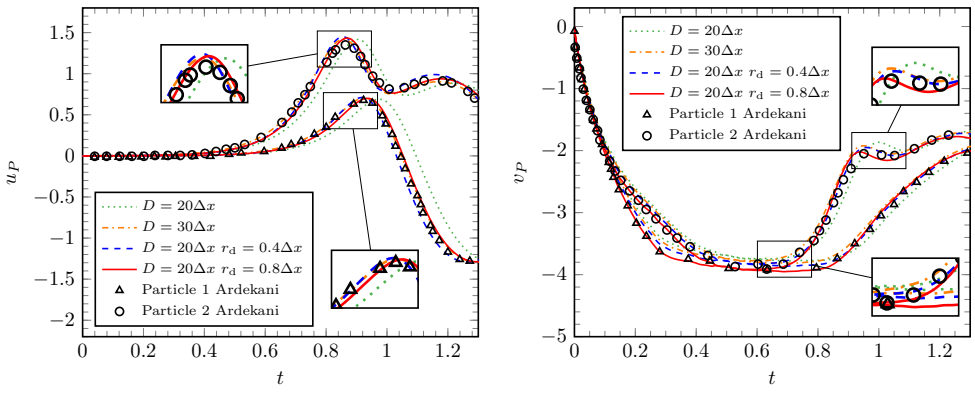
$$F_\mathrm{cn} = k_\mathrm{n}\,\delta_\mathrm{n} + c_\mathrm{n}\,v_\mathrm{n}\,, \tag{5.10a}$$

$$F_\mathrm{ct} = \begin{cases} k_\mathrm{t}\,\Delta\,\delta_\mathrm{t} + c_\mathrm{t}\,v_\mathrm{t} & F_\mathrm{ct} < \eta\,F_\mathrm{ct}\,, \\ \eta\,F_\mathrm{ct} & F_\mathrm{ct} \geq \eta\,F_\mathrm{ct}\,, \end{cases} \tag{5.10b}$$

where k_n, k_t are the normal and tangential spring coefficients, c_n, c_t are the normal and tangential damping coefficients, v_n, v_t are the normal and tangential relative velocity at contact point, δ_n is the normal overlap, $\Delta\,\delta_t$ is the increment of the relative tangential displacement, and η is the friction coefficient. In the present work, the critical value ε_c is set to $2\Delta x$ to accommodate the range of the four-point discrete delta function [159].

Simulation results are illustrated in Figure 5.15, where the evolution of the velocity of the particles is plotted and compared to the sharp-interface method presented by Ardekani and Rangel [189]. Since the separation distance between the two particles for most of the DKT process approaches zero, the effect of the interface diffusion associated with the IBM becomes increasingly significant, and the numerical accuracy is affected. In Figure 5.15, the diffusive effect is alleviated by introducing the retraction distance scheme with $r_d = 0.4\Delta x$ and $r_d = 0.8\Delta x$, which can achieve accuracy equivalent to an increased spatial resolution.

From the above case for two impacting particles, it is shown that when the two particles are not in close contact, the usual r_d of 0.4 can be chosen. However, when the two particles move close to each other, the value of r_d should be switched to 0.8 as the diffuse interfaces start to overlap (G becomes $4\Delta x$ or less). This adjustment is necessary



(a) Transverse velocity u_p. (b) Longitudinal velocity v_p.

Figure 5.15: Effect of the interface diffusion on the motion of two particles settling in a channel under gravity: (a) transverse velocity u_p, and (b) longitudinal velocity v_p as functions of time, comparing different retraction distances r_d. The numerical results in Ref. [189] are given for comparison.

because, as the gap between particles decreases, the interaction enters the lubrication

regime, where hydrodynamic resistance rises sharply with reducing separation. In the present IB-LBM formulation, the diffuse interface alters the effective boundary thickness, which in turn influences the fluid gap treatment and results in an underestimation of lubrication resistance. This limitation is particularly relevant for the DKT process, which involves an extended near-contact phase. When lubrication forces are not properly captured, contact dynamics are affected, and the transition to the tumbling phase is altered. Increasing r_d mitigates diffuse-interface overlap and preserves lubrication effects prior to contact.

To simplify the computation, retraction distances r_d of $0.4\Delta x$ and $0.8\Delta x$ are tested in the current DKT process, and both show satisfactory results. However, the collision model used in the simulations has a significant influence on the interface retraction scheme. The present DEM algorithm allows particle overlap by modelling their interaction using a linear spring-dashpot model, which is considerably different from the strategy used in Ref. [189]. Additionally, a cut-off distance ε_c is applied in order to activate the DEM contact forces when the gap between the particles falls below this threshold. The resulting short-range repulsive force models the hydrodynamic resistance when the particles are approaching and ensures that the contact interactions are correctly captured. Overall, the combination of the boundary retraction scheme and the DEM contact model alleviates the limitations of diffuse-interface IB-LBM in close-range particle interactions during DKT. Nevertheless, further work is required to improve the interface retraction technique in the near-contact treatment.

5.5 Conclusions

Because of its versatility, diffuse-interface IBM is a viable method to simulate complex fluid-solid interaction problems. It offers advantages in terms of computational efficiency as it does not require updating solid fractions at every time step for moving boundary problems. Additionally, since the fluid-solid interface is tracked, the coupling with particle solvers such as DEM is easier to implement than in Ref. [152], where the particles need to be mapped into the fluid domain. An important drawback of this approach is the diffuse interface, which changes both the apparent size of the solid object and the

exact surface location. In this work, the coupled IB-LBM has been applied to four benchmark problems to investigate the effects of interface diffusion. It has been found that the diffuse interface has a negligible impact on unbounded geometries. However, in confined computational domains, surface interaction enhances interface diffusion effects and reduces the numerical accuracy of diffuse-interface IBM compared to sharp-interface methods. Interactions between particles are another challenging issue for traditional diffusive IBM formulations. When particles are in close contact, diffuse interfaces start to overlap, leading to more pronounced effects.

A boundary retraction approach has been tested to compensate for these sources of error. This strategy has been proven effective in achieving a better representation of the solid boundary and improving the accuracy with limited computational costs. It has been demonstrated that compared to a traditional implementation, multi-direct-forcing IBM with boundary retraction achieves a better performance for confined geometries and particle interaction problems. The easy-to-use retraction distance is found numerically to be $r_{\mathrm{d}} = 0.4$, which is to be doubled when two diffuse interfaces start to overlap.

Chapter 6

Numerical Stability in the Dynamics of Light Structures

6.1 Introduction

The stability properties of IBM approaches are usually limited to cases characterised by density ratios greater than unity. The introduction of a strong-coupling scheme overcomes this limiting restriction and extends the application range of the current IB-LBM framework. This chapter aims to provide an understanding of the stability properties of the strongly coupled IB–LBM formulation and evaluate its performance across representative problems.

The numerical simulations investigate the dynamics of falling and rising particles over a range of Reynolds numbers. These configurations allow to assess the stability and computational performance of the strongly coupled IB-LBM scheme while exploring the effects of the structural parameters and the local flow field. This analysis establishes the conditions when the strong coupling becomes necessary to ensure numerical stability and evaluates its influence on both accuracy and computational performance. At the same time, the results improve the understanding of the dynamics of low-density bodies, clarifying the role of the internal mass effect in cases where weakly coupled approaches become unstable.

Section 6.2 describes the sources of instability related to the internal mass effect and

the associated density-ratio limitation. The numerical setup and simulation methodology are presented in Section 6.3. The performance of the strongly coupled IB–LBM formulation is then assessed through a series of test cases: falling and rising particles (Section 6.3.1), a single particle released off-centre (Section 6.3.2), and multiple particles rising (Section 6.3.3). Finally, Section 6.4 summarises findings on the stability behaviour of different coupling strategies and highlights how the proposed formulation enables the accurate modelling of light-particle dynamics.

6.2 Problem Statement

Several findings indicate that the internal mass effect described in Section 3.3.5 affects the numerical stability of IBM schemes in problems where the solid body density is comparable to or smaller than the density of the surrounding fluid, i.e. $\rho_s/\rho_f \leq 1$ [107, 110, 111, 157, 161, 165]. In such cases, the internal mass term becomes comparable to the solid object mass causing instabilities to arise when integrating the equations of rigid body motion. As a result, different studies observed growing oscillations of the particle velocity while updating the rigid body motion [107].

Despite the efforts to compensate the internal mass effect, the moving bounce-back method presented by Ladd [143] becomes unstable for solid to fluid density ratio values below 2. Similarly to the approach presented by Qi [211], the compensation force calculated by ten Cate et al. [165] extends the numerical stability to density ratios of $\rho_s/\rho_f \geq 1.15$.

The rigid body approximation proposed by Uhlmann [107] to evaluate the motion of the internal fluid introduces a singularity in the equations of body motion for $\rho_s/\rho_f = 1$. Considering the case of a solid particle accelerating from rest due to gravity, the lower limit of the density ratio that achieves numerical stability corresponds to $\rho_s/\rho_f \geq 1.05$ for circular disks and $\rho_s/\rho_f \geq 1.2$ for spherical particles.

Alternatively, the formulation of the rigid body motion suggested by Feng [161] eliminates the singular value in the equations of body motion and does not present a limitation of the density ratio. Similarly, the Lagrangian points approximation developed by Suzuki and Inamuro [157] is unconditionally stable.

Kempe and Fröhlich [111] suggested that for problems involving significant angular acceleration, the motion of the internal fluid deviates from rigid body approximation due to the distribution of forcing points on the interface on Γ_s rather than on the interior solid domain Ω_s. Therefore, their formulation replaces the rigid body approximation with a direct evaluation of the linear and angular momentum volume integrals by means of a second-order midpoint quadrature rule. This approach increases the numerical stability limit to $\rho_s/\rho_f \geq 0.3$ [108, 111].

These findings indicate that the coupling between the fluid and solid equations imposes a limitation on the density ratio to achieve numerical stability. Although various remedies have been proposed, their performance depends on both the formulation employed and the characteristics of the problem under consideration.

Moreover, different studies identified that the stability properties of partitioned approaches are not exclusively influenced by the density ratio [43, 105]. The local flow properties also have a significant contribution because they affect the hydrodynamic force and torque acting on the solid body. Additionally, it has been suggested that weakly coupled schemes suffer from numerical stability problems for a given structural density when the computational domain increases [43]. Therefore, the numerical stability depends both on structural properties such as density and geometry, and on the local conditions of the surrounding fluid.

It has been demonstrated that weakly coupled schemes optimise computational costs and reduce algorithm complexity, but restrict the stability limit for low-density ratio problems. Therefore, for such applications strongly coupled algorithms are generally preferred [43, 105].

6.3 Numerical Simulations

The aim of this section is to provide a comprehensive and systematic study of problems involving solid particles characterised by different density ratios including small values, i.e. $\rho_s/\rho_f < 1$. As opposed to the weakly coupled scheme, the strong coupling expands the stability interval of the IBM in order to correctly capture the dynamics of light

particles. The extended stability properties of the strongly coupled scheme allow to reduce the resolution required for accurate simulations, resulting in a reduced demand of computational resources. In addition to this, the strongly coupled scheme successfully captures physical phenomena that cannot be simulated with a regular IB scheme. The performance of the strongly coupled IB-LBM scheme is evaluated for three test cases: falling and rising particles both in the creeping flow regime and for moderate values of the Reynolds number, single particle released off-centre, and multiple particles rising. The numerical results are consistently compared to analytical expressions and both experimental and numerical studies in the available literature.

All simulations are performed on a uniform lattice using the D2Q9 velocity set, with the collision operator defined by the central-moment lattice Boltzmann method (CLBM). The immersed boundary formulation is characterised by a four-point regularised discrete delta function and a retraction distance of $r_\mathrm{d} = 0.4$, unless otherwise stated.

6.3.1 Falling and Rising Particles

The problem of a particle moving freely under hydrodynamic forces provides a suitable test case to investigate the performance of the strongly coupled IB-LBM scheme and assures a significant comparison with the weakly coupled scheme. The study focuses first on the creeping flow regime for $Re = 5 \times 10^{-4}$. This case is particularly significant as the available approximate analytical formulations provide a valuable comparison. The stability properties of the scheme are investigated for a wide range of density ratio values $\rho_\mathrm{s}/\rho_\mathrm{f}$ to verify the ability of the strong coupling to capture the dynamics of light particles. The problem is then extended to a moderate Reynolds number regime to investigate the dependence of stability on this parameter. Additionally, a higher confinement ratio is considered.

Creeping Flow Regime

The strong-coupling scheme is tested for the case of a particle moving freely under hydrodynamic forces in the creeping laminar flow regime. This problem is suitable for

validation as approximate analytical formulations are available [194,203], in addition to extensive numerical and experimental benchmark results [194,195,199–203].

Table 6.1: Particle and fluid properties for falling and rising particles in the creeping flow regime.

Geometry		Parameters	
Diameter D	0.1	Density ρ_f	1
Channel width W	2	Viscosity μ_f	1
Channel height H	5	Reynolds number Re	5×10^{-4}
Confinement ratio κ	0.05		

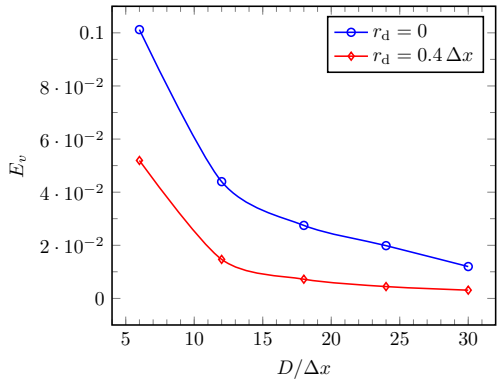
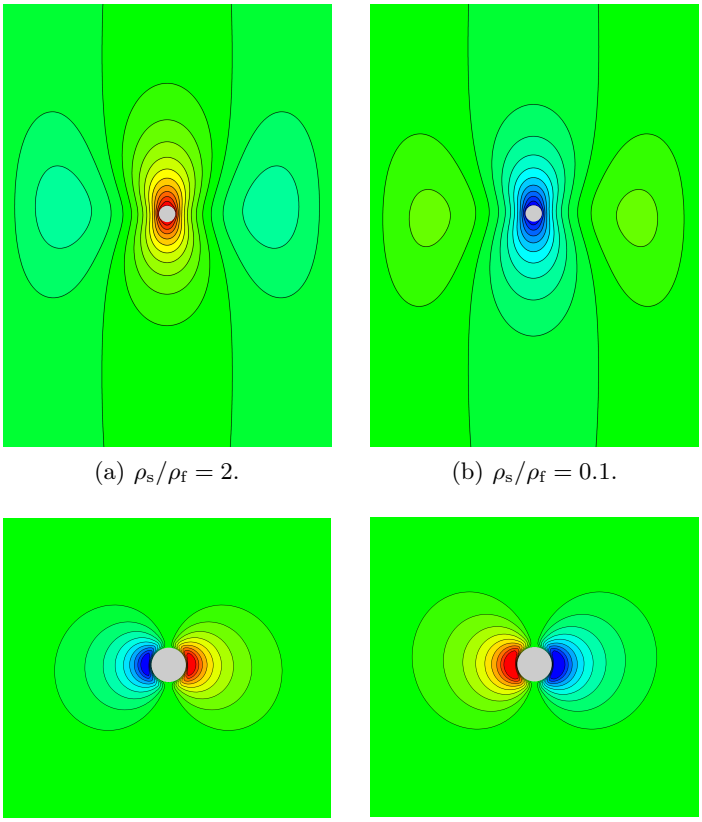


Figure 6.1: Velocity error E_v for sedimentation of a particle under gravity for retraction distance $r_\mathrm{d} = 0$ and $r_\mathrm{d} = 0.4\Delta x$.

A cylindrical particle of diameter D is initially located along the centreline of a channel of width W and height H. The computational domain is bounded by solid walls, and a no-slip boundary condition is implemented using a halfway bounce-back scheme. A schematic representation of the geometry of this case is provided in Figure 5.8 for reference. The initial geometry and properties used in the simulations are listed in Table 6.1. The net gravitational force F_g acting on the particle is given by the expression

$$F_\mathrm{g} = \frac{\pi\, g D^2\, (\rho_\mathrm{s} - \rho_\mathrm{f})}{4} \tag{6.1}$$

where g is the gravitational acceleration, ρ_s is the particle density, and ρ_f is the fluid density. When the particle density is lower than the fluid density, i.e. $\rho_\mathrm{s} < \rho_\mathrm{f}$, the particle moves upwards, while $\rho_\mathrm{s} > \rho_\mathrm{f}$ corresponds to the sedimentation case. For



(a) $\rho_s/\rho_f = 2.$ (b) $\rho_s/\rho_f = 0.1.$

(c) $\rho_s/\rho_f = 2.$ (d) $\rho_s/\rho_f = 0.1.$

Figure 6.2: Particles falling and rising: contours of the vertical velocity (a)-(b), and vorticity (c)-(d) for $D = 12\Delta x$ and retraction distance $r_d = 0.4\Delta x$.

both configurations, a drag force F_d develops as the particle is accelerated and once it balances the gravitational force, the particle reaches a constant velocity V_t. The approximate analytical expression for the wall-corrected terminal velocity V_t is given by

$$V_t = \frac{\pi g D^2 (\rho_s - \rho_f)}{4\mu_f \lambda_F(\kappa)}, \tag{6.2}$$

where λ_F is the Faxén wall correction factor that can be expressed as [152, 203]

$$\lambda_F = \frac{4\pi}{A_0 - \ln(\kappa) + A_2\,\kappa^2 + A_4\,\kappa^4 + A_6\,\kappa^6 + A_8\,\kappa^8}, \tag{6.3}$$

where the numerical coefficients are $A_0 = -0.9156892732$, $A_2 = 1.7243844$, $A_4 = -1.730194$, $A_6 = 2.405644$, and $A_8 = 4.59131$. The velocity error $E_v = |V - V_t/V_t|$

is used to evaluate the accuracy of the numerical results by comparing the analytical terminal velocity V_t and the simulated one V. The simulations are performed with increasing lattice resolution, i.e. $\Delta x = (D/6,\ D/12,\ D/16,\ D/24)$ using a density ratio $\rho_s/\rho_f = 1.01$. The calculated velocity error values E_v are plotted in Figure 6.1 and compared to the numerical results of the IB-LBM scheme without boundary retraction scheme, i.e $r_d = 0$. As Figure 6.1 suggests, the numerical error using the boundary retraction scheme shows a satisfactory convergence for an increased spatial resolution, therefore this configuration is chosen to run the simulations.

Table 6.2: Velocity error E_v and stability at different density ratio values ρ_s/ρ_f for the falling and rising particle test case, using lattice size $D = 6\Delta x$.

	Weak coupling	Strong coupling			
		$\Gamma = 0$	$\Gamma = 0.5$	$\Gamma = 1$	$\Gamma = 1.5$
ρ_s/ρ_f	E_v	E_v	E_v	E_v	E_v
2	0.0130	-	0.00918	0.00918	0.00918
1.5	0.0109	-	0.00664	0.00668	0.00665
1.01	-	-	0.0410	0.00569	0.00568
0.9	-	-	-	0.00547	0.00547
0.7	-	-	-	0.00608	0.00601
0.5	-	-	-	0.00662	0.00662
0.3	-	-	-	0.00743	0.00743
0.1	-	-	-	0.00849	0.00849
0.05	-	-	-	0.00879	0.00874
0.01	-	-	-	0.00904	0.00899

To test the stability of the strongly coupled IB-LBM scheme, increasingly smaller density ratios are considered, ranging from the sedimentation case for $\rho_s/\rho_f > 1$ to particle rising for $\rho_s/\rho_f < 1$. The contours of the vertical velocity and the vorticity are presented in Figure 6.2 for a heavy $\rho_s/\rho_f = 2$ and light $\rho_s/\rho_f = 0.1$ particle configuration. The stability of the scheme is evaluated by performing simulations using the weak-coupling scheme and comparing results with the strong coupling for different values of Γ. The numerical parameter Γ controls the temporal discretisation of the particle motion according to Equation 3.92, defining the implementation of the fluid–solid coupling interface. The values of the terminal velocity error E_v are presented in Table 6.2 - 6.4

Table 6.3: Velocity error E_v and stability at different density ratio values ρ_s/ρ_f for the falling and rising particle test case, using lattice size $D = 12\Delta x$.

	Weak coupling	Strong coupling			
		$\Gamma = 0$	$\Gamma = 0.5$	$\Gamma = 1$	$\Gamma = 1.5$
ρ_s/ρ_f	E_v	E_v	E_v	E_v	E_v
2	0.00306	-	0.00297	0.00297	0.00281
1.5	0.000493	-	0.000391	0.000391	0.000391
1.01	0.000321	-	0.000409	0.000408	0.000410
0.9	-	-	-	0.000364	0.000423
0.7	-	-	-	0.000369	0.0004098
0.5	-	-	-	0.000392	0.000461
0.3	-	-	-	0.00120	0.00120
0.1	-	-	-	-	0.00227

Table 6.4: Velocity error E_v and stability at different density ratio values ρ_s/ρ_f for the falling and rising particle test case, using lattice size $D = 18\Delta x$.

	Weak coupling	Strong coupling			
		$\Gamma = 0$	$\Gamma = 0.5$	$\Gamma = 1$	$\Gamma = 1.5$
ρ_s/ρ_f	E_v	E_v	E_v	E_v	E_v
2	0.00290	-	0.00285	0.00285	0.00279
1.5	0.000345	-	0.000299	0.000299	0.000299
1.01	0.0000265	-	0.0000180	0.0000180	0.0000127
0.9	-	-	-	0.000201	0.0000203
0.7	-	-	-	0.000295	0.000258
0.5	-	-	-	0.000327	0.000851

for different lattice resolutions. It is worth noting that the weakly coupled scheme suffers from numerical stability issues for particle rising cases ($\rho_s/\rho_f < 1$), and the lowest lattice resolution, i.e. $D = 6\Delta x$ is not capable of simulating cases where the density ratio is around unity. In this implementation of the scheme, the stability can be improved by increasing the lattice grid size, as the limit density ratios for $D = 6\Delta x$, $D = 12\Delta x$, and $D = 18\Delta x$ are $\rho_s/\rho_f = 1.5$, $\rho_s/\rho_f = 1.01$, and $\rho_s/\rho_f = 1.01$ respectively. However, a further increase of lattice resolution does not correspond to a stability improvement and $\rho_s/\rho_f = 1.01$ is the limit density ratio that can be achieved using this method. The origin of this limit lies in the asynchronous coupling of the fluid and solid solvers

associated with weakly coupled schemes. In such formulations, the hydrodynamic force and torque are evaluated based on the kinematic quantities from the previous time step. As a result, the coupling conditions at the fluid–solid interface are not satisfied simultaneously. Furthermore, for light particles the internal mass of the fluid enclosed within the particle can become comparable to or larger than the solid mass, and even small discrepancies in the applied hydrodynamic force can generate oscillations.

In contrast, the strong-coupling strategy employed in this work solves the fluid and solid motions concurrently by adding the velocity corrections to both the fluid and the solid simultaneously, ensuring that the coupling conditions are satisfied at each time step. This approach eliminates the temporal mismatch inherent to explicit schemes and suppresses the instabilities associated with the internal mass effect. Within the strong-coupling framework, the parameter Γ controls the temporal discretisation. The strong coupling results in Table 6.2 - 6.4 are listed for different values of the parameter Γ and demonstrate its influence on the stability of the scheme implementation. For $\Gamma = 0$, the scheme is fully explicit, and the results are unstable for all the considered lattice resolutions. The results for $\Gamma = 0.5$ yield an improved stability limit compared to the weakly coupled formulation, and the scheme remains stable at the lowest lattice resolutions considered, i.e. $D = 6\Delta x$. The observed stability trend is consistent with the findings of Zhang et al. [167], where a stability analysis indicated that the scheme is conditionally stable only for $\rho_s > \rho_f$. The choices of $\Gamma = 1$ and $\Gamma = 1.5$ correspond to first and second-order implicit discretisation, respectively. Both implementations produce stable and accurate results across the entire range of density ratios tested, including light particle cases ($0.1 < \rho_s/\rho_f < 0.9$), and the particle rising problem can be successfully simulated. For the strong coupling with $\Gamma = 1$ and $\Gamma = 1.5$, the numerical stability cannot be improved by increasing the lattice resolution. The terminal velocity values V_t for different density ratios in the range $\rho_s/\rho_f = (0.1 - 2)$ are plotted in Figure 6.3 and compared to the ones calculated using the approximate analytical expression given by Equation 6.2. The results show a satisfactory agreement with the predicted ones, proving that the strongly coupled scheme is stable and accurate even for light particles.

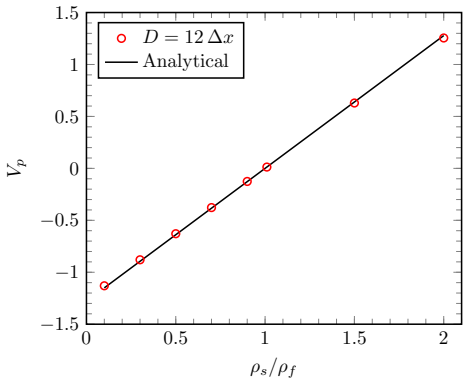


Figure 6.3: Terminal velocity V_p for sedimentation of a particle under gravity for different density ratio values $\rho_\mathrm{s}/\rho_\mathrm{f}$. Analytical results for V_t calculated with Equation 6.2 are given for comparison.

Moderate Reynolds Number Regime

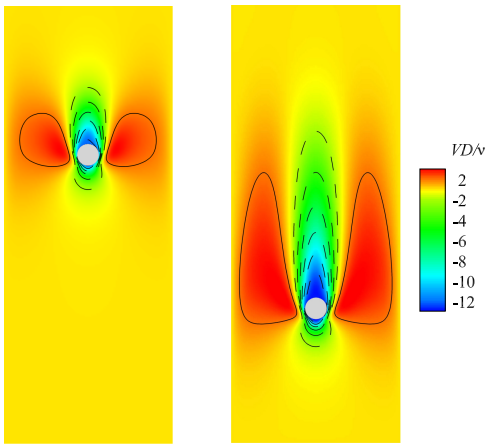
The test case is expanded to cover the intermediate Reynolds number regime and evaluate the effects of a more significantly confined geometry. The case setup is chosen to compare results with the work of Wan and Turek [212, 213], and the simulation parameters are listed in Table 6.5. As opposed to the creeping flow limit, the moderate Reynolds number regime is characterised by an asymmetric wake structure, which adds complexity to the problem and impacts the stability of the scheme. For this problem,

Table 6.5: Particle and fluid properties for the case of falling and rising particles at moderate Reynolds number.

Parameters		Parameters	
Diameter D	0.25	Fluid density ρ_f	1
Channel width W	2	Viscosity μ_f	0.1
Channel height H	6	Particle density ρ_s	1.25
Confinement ratio κ	0.125		

the Reynolds number is defined as

$$Re = \frac{\rho_\mathrm{s}\, D \sqrt{u_\mathrm{p}^2 + v_\mathrm{p}^2}}{\mu_\mathrm{f}}\,, \tag{6.4}$$



(a) $t = 0.2$. (b) $t = 0.6$.

Figure 6.4: Particles falling and rising: contours of the vertical velocity of the particle centre for $D = 12\Delta x$ at time steps (a) $t = 0.2$ and (b) $t = 0.6$.

Table 6.6: Maximum Reynolds number value Re_m for the case of falling and rising particles at moderate Reynolds number and comparison to the reference data.

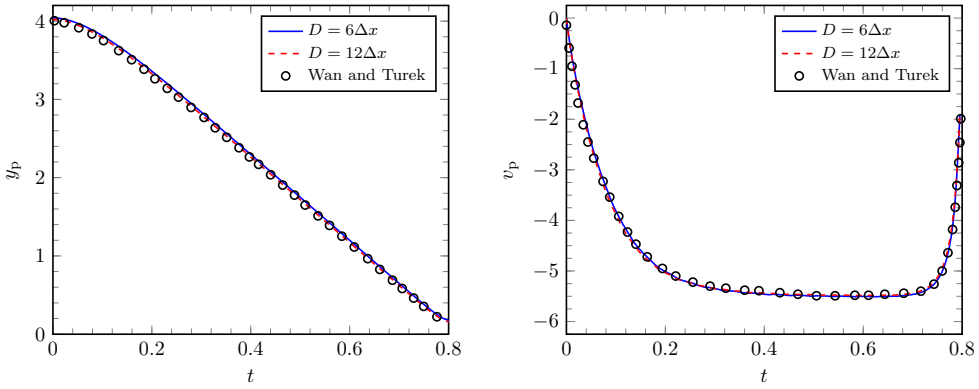
Study	ρ_s/ρ_f	$D/\Delta x$	Re_m
Present	1.25	1/60	17.25
	1.25	1/120	17.28
Glowinski et al. [214]	1.25	1/256	17.31
Wan and Turek [212]	1.25	1/96	17.15
Di et al. [215]	1.25	1/265	17.32
Wang et al. [163]	1.25	1/265	17.31

where u_p and v_p are the horizontal and vertical velocity component, respectively. Figure 6.4 illustrates the contours of vertical velocity of the particle centre and the characteristic wake structure corresponding to this Reynolds number regime.

To verify the spatial resolution, the simulations are performed using two increasingly refined lattice grids, i.e. $D = 6\Delta x$ and $D = 12\Delta x$. The maximum computed values of the Reynolds number Re_m are reported in Table 6.6 for the different lattice grids and compared to other available numerical studies. The results indicate that the selected lattice resolutions provide a suitable comparison with other numerical methods. It is worth noting that the boundary retraction scheme provides similar accuracy compared to the results in Refs. [163,214,215] whose resolutions are approximately double the one

considered in this study, i.e. $D/\Delta x = 120$. The evolution in time of the vertical position y_p and the vertical velocity v_p of the falling particle are plotted in Figure 6.5. Since the results for both spatial resolutions are a satisfactory match with the corresponding simulations in Ref. [212], this setup is selected for the particle rising case.

The density ratio is adjusted to explore the range $\rho_\mathrm{s}/\rho_\mathrm{f} = (0.1 - 0.99)$, while keeping the same Reynolds number value. The time evolution of the vertical velocity v_p of the particle centre for $D = 6\Delta x$ is plotted in Figure 6.6 for the different density ratios. The results confirm the stability properties of the strongly coupled scheme for a significant range of Reynolds number values.



(a) Vertical position y_p.

(b) Vertical velocity v_p.

Figure 6.5: Particles falling and rising: time evolution of (a) the vertical position y_p and (b) vertical velocity v_p of the particle centre for $D = 12\Delta x$. The results of Wan and Turek [212] are included for comparison.

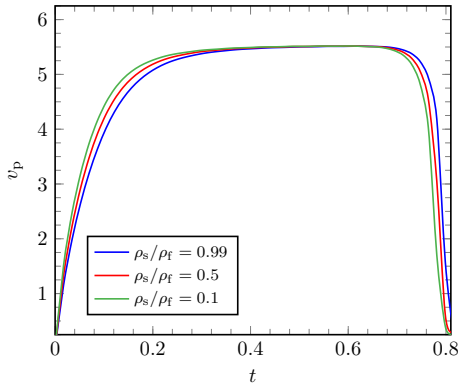


Figure 6.6: Particles falling and rising: time evolution of the vertical velocity v_p of the particle centre for $D = 12\Delta x$ and different density ratios $\rho_\mathrm{s}/\rho_\mathrm{f}$.

6.3.2 Single Particle Released Off-Centre

The case of sedimentation of a particle released off-centre is used as a benchmark to test the accuracy of the strongly coupled IB-LBM scheme for intermediate Reynolds number values. Then, the case is expanded to the problem of particle rising off-centre to investigate the stability properties. This problem includes an additional level of complexity by introducing particle rotation. The sedimentation of a particle released

Table 6.7: Particle and fluid properties for the case of a single particle released off-centre.

Geometry		Parameters	
Diameter D	0.08	Fluid density ρ_f	1
Channel width W	0.32	Viscosity μ_f	0.01
Channel height H	4	Particle density ρ_s	1.002
Initial location (W, H)	$(1, 45)$		
Confinement ratio κ	0.25		

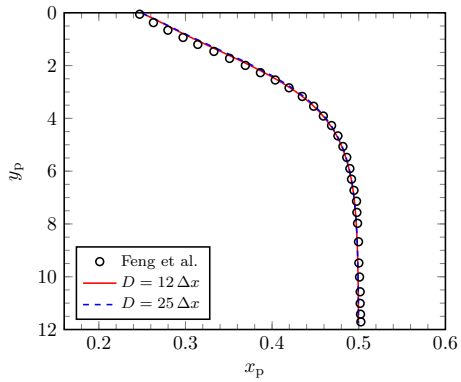


Figure 6.7: Settling trajectory of a particle released off-centre for $D = 12\Delta x$ and $D = 25\Delta x$. The numerical results from Feng et al. [220] are given for comparison.

off-centre has been investigated in several studies [216–219], and the results of Feng et al. [220] are used to validate the model. Feng et al. [220] studied the motion of a particle settling between parallel walls and identified the following sedimentation regimes:

(a) Steady equilibrium with monotonic approach.

(b) Steady equilibrium with a transient overshoot.

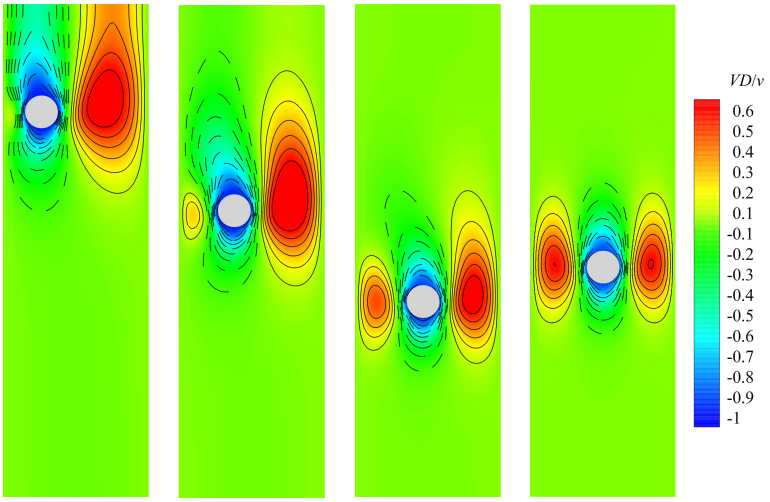
(c) Weak oscillatory motion.

(d) Strong oscillatory motion.

(e) Irregular oscillatory motion.

The characterisation of the different regimes is based on the equilibrium position, the approaching trajectory and the oscillations around the equilibrium position. It has been suggested in Ref. [220] that the transition between the monotonic approach to equilibrium and the transient overshoot is connected to the transition between the viscous regime without flow separation and the laminar flow corresponding to the emerging steady symmetric eddies in the particle wake.

The initial geometry and fluid properties used in the simulations are listed in Table 6.7.

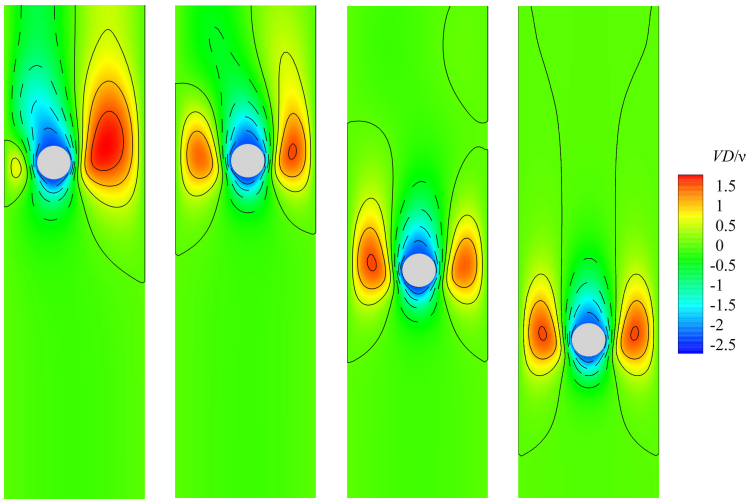


(a) $t = 100$. (b) $t = 300$. (c) $t = 500$. (d) $t = 800$.

Figure 6.8: Velocity contours of a settling particle released off-centre at $Re = 1.88$ at time steps (a) $t = 100$, (b) $t = 300$, (c) $t = 500$, and (d) $t = 800$.

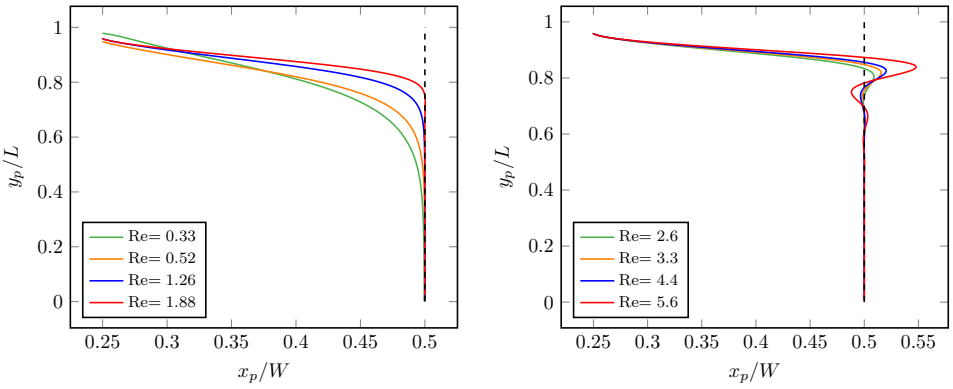
The present numerical model is validated by comparing the results to the ones presented by Feng et al. [220]. Figure 6.7 shows an excellent agreement between the current method and the trajectory reported in Ref. [220] for the case of a particle released from the initial position $x/W = 0.25$ at $Re = 0.52$.

The current simulations investigate a broad range of Reynolds number values to capture the characteristics of different sedimentation regimes and the corresponding transition. The distinguishing flow structures of the steady equilibrium with a monotonic approach and the steady equilibrium with a transient overshoot regime are illustrated in Figure 6.8 and Figure 6.9, respectively. In the steady equilibrium with monotonic approach regime, the particle is released asymmetrically from an initial off-centre position, and as it settles, it gradually drifts towards the centreline experiencing a small rotational motion. The centre of the channel represents the equilibrium position where the particle reaches its terminal velocity V_t and the rotation stops. The steady equilibrium with a transient overshoot regime is characterised by a different approach to the equilibrium position at the centreline of the channel. The particle overshoots the centreline and subsequently undergoes a damped oscillation around the centre of the channel. It is worth noting that the oscillation amplitude increases proportionally to the Reynolds number value. For both regimes, the steady equilibrium position at the centre of the channel is independent of the initial position from which the particle is released. Figure 6.10 presents the particle trajectory for the different sedimentation regimes. The findings align with the results described in Ref. [203, 220].



(a) $t = 100$. (b) $t = 200$. (c) $t = 300$. (d) $t = 800$.

Figure 6.9: Velocity contours of a settling particle released off-centre at $Re = 4.4$ at time steps (a) $t = 100$, (b) $t = 300$, (c) $t = 500$, and (d) $t = 800$.



(a) Monotonic approach. (b) Transient overshoot.

Figure 6.10: Settling trajectory of a particle released off-centre at increasing Reynolds numbers, illustrating different sedimentation regimes: (a) steady equilibrium with monotonic approach and (b) steady equilibrium with transient overshoot.

The effects of the geometric confinement on the stability of the method and the previously described sedimentation regimes are investigated. The width of the computational domain is increased to $W = 8$, corresponding to a confinement ratio of $\kappa = 0.125$. The trajectory of the particle centre is presented in Figure 6.11 for a wide range of Reynolds number values. It is shown that for a decreased confinement, the transition between the different sedimentation regimes is not observed for the same range of Reynolds number values considered in the previous case. It is suggested that the sedimentation regimes are affected by the wall-particle interactions, which are less significant for a confinement ratio of $\kappa = 0.125$.

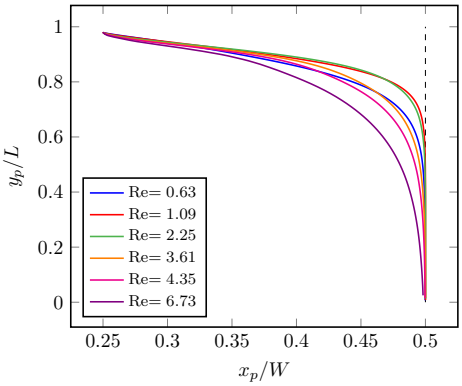
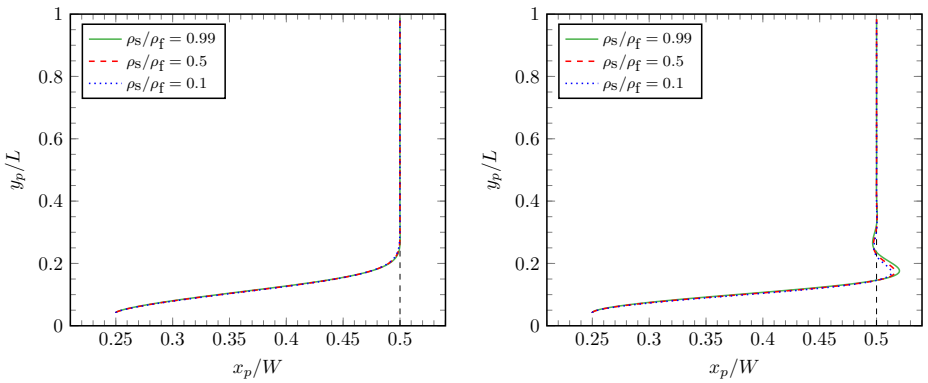


Figure 6.11: Settling trajectory of a particle released off-centre at different Reynolds numbers for confinement ratio $\kappa = 0.125$.



(a) Monotonic approach.

(b) Transient overshoot.

Figure 6.12: Rising trajectory of a particle released off-centre at increasing Reynolds numbers, illustrating different regimes: (a) steady equilibrium with monotonic approach and (b) steady equilibrium with transient overshoot.

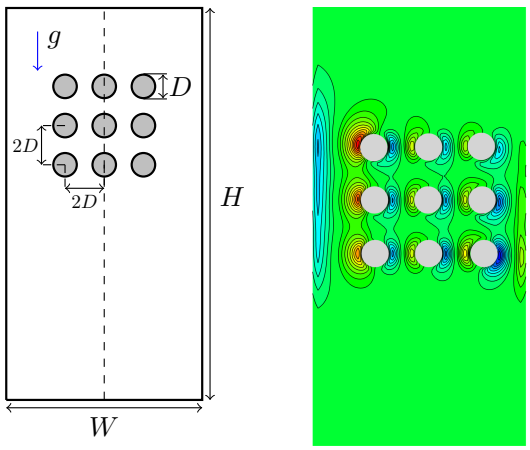
Building upon the successful simulation of the sedimentation case, the problem of a particle rising off-centre is investigated. The stability of the strongly coupled scheme is tested by extending the density ratio range to $0.5 \leq \rho_s/\rho_f \leq 0.99$. The Reynolds number values selected to simulate the rising trajectory of a particle released off-centre in the steady equilibrium with the monotonic approach regime and the steady equilibrium with a transient overshoot are $Re = 1.88$ and $Re = 4.4$, respectively. The corresponding results are presented in Figure 6.12. As reported, the strongly coupled IB-LBM scheme provides satisfactory results for this problem and successfully captures the flow characteristic of light particles.

6.3.3 Multiple Particles Rising

The increased stability of the strongly coupled scheme is not only important for its ability to capture light particle phenomena but also for its computational efficiency. The capabilities of the strong coupling to simulate low-density ratio problems while saving computational costs are tested for the case of multiple particles rising, and the results serve as a demonstration of the method's applicability to multi-particle configurations. The present test case focuses on the flow patterns of multiple particle systems moving freely in a narrow channel. The initial geometry is represented in Figure 6.13 and fluid

Table 6.8: Particle and fluid properties for multiple falling and rising particles.

Geometry		Parameters	
Diameter D	1	Fluid density ρ_f	1
Channel width W	6	Viscosity μ_f	1
Channel height H	200	Particle density ρ_s	0.1
Confinement ratio κ	0.17		



(a) (b)

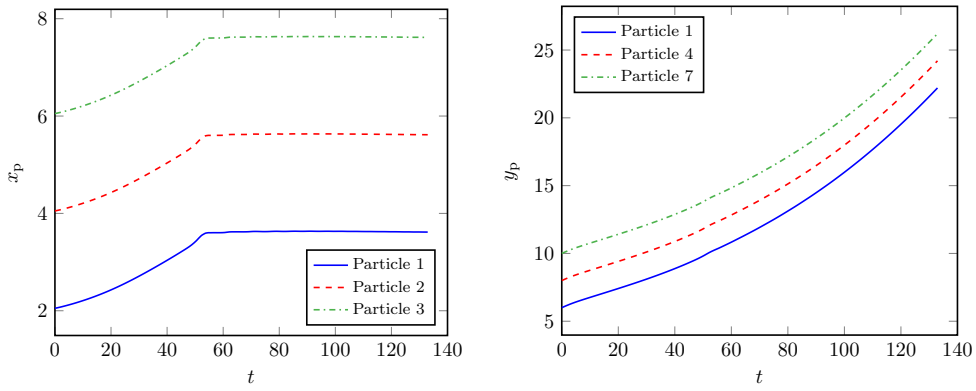
Figure 6.13: Multiple particles rising: (a) schematics of the computational domain and (b) vorticity contours.

flow conditions used in the simulations are listed in Table 6.8.

A characteristic parameter for this test case can be defined with the following nondimensional expression

$$F = \frac{\left(|\rho_\mathrm{s}/\rho_\mathrm{f} - 1|\, Dg\right)^{1/2}}{\nu}\,. \tag{6.5}$$

The value considered in the following simulations is $F = 1$. The corresponding value of the Reynolds number can be calculated using the average rising velocity V, resulting in $Re = 0.4$. The vorticity contours for the case of nine particles rising in this flow regime can be visualised in Figure 6.13. At $F = 1$, the nine particles rise with the same vertical velocity and undergo a slight lateral migration before reaching their equilibrium positions. The time evolution of the trajectory of the particle centres is plotted in Figure 6.14. The horizontal displacement is shown for the particles in the first row, and the vertical position is given for the particles in the first column.



(a) Horizontal position.

(b) Vertical position.

Figure 6.14: Rising trajectory of nine particles: (a) horizontal and (b) vertical displacement of the particle centre.

To test the use of computational resources required by the strongly coupled algorithm, the problem is expanded to fifty particles, considering the same parameters. The vorticity contours for this test case are shown in Figure 6.15. It is demonstrated that the stability of the scheme allows the simulation of a large number of particles with a significant improvement in computational efficiency compared to the weakly coupled scheme.

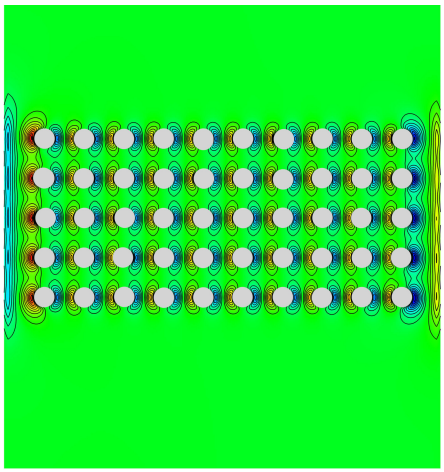


Figure 6.15: Vorticity contours for the case of fifty particles rising.

6.4 Conclusions

This chapter provided a comprehensive analysis of the strongly coupled IB-LBM scheme through various test cases. The performance was evaluated for increasingly complex problems, and satisfactory results were found. It was demonstrated that the strong coupling successfully extends the stability of IBM to cases characterised by small density ratios. The simulations accurately explored the dynamics of light particles and revealed behaviours that are not accessible with weakly coupled approaches. In addition, the formulation demonstrated improved computational efficiency.

Chapter 7

Critical Mass Effects in Vortex-Induced Vibration

7.1 Introduction

Vortex-induced vibrations (VIV) represent a complex class of flow-induced instability problems, characterised by strong two-way coupling between vortex shedding and the motion of the structure. In the lock-in regime, synchronisation between vortex shedding and natural frequency leads to large oscillations and a strong dependence of the response on structural parameters. For these reasons, VIV is considered to assess the robustness of the numerical scheme.

This chapter examines the capability of the strongly coupled IB–LBM framework to simulate VIV across a range of Reynolds numbers and mass ratios. The objective is to determine whether the stability and accuracy benefits of the strong coupling extend to problems involving complex wake dynamics and large-amplitude structural vibrations. The numerical results are used to assess the ability of the method to capture characteristic VIV features, including the onset of the lock-in regime, the resulting oscillation amplitudes, and the associated wake structures. Additionally, the analysis contributes to the understanding of VIV phenomena relevant to light structures, where weakly coupled approaches exhibit stability limitations.

Section 7.2 reviews the critical-mass behaviour and defines the VIV configurations

considered in this work. The numerical approach and simulation setup are outlined in Section 7.3. To consolidate the numerical setup and resolution, the flow past a stationary cylinder is first examined in Section 7.3.1. The framework is then applied to the vortex-induced vibrations of a freely oscillating cylinder in Section 7.3.2, where the onset of the lock-in regime and the associated response branches are analysed over a range of Reynolds numbers and mass ratios. Finally, Section 7.4 draws together the main outcomes, assessing the ability of the strongly coupled IB–LBM formulation to capture the critical-mass phenomenon and to remain stable at very low density ratios.

7.2 Problem Statement

Navrose and Mittal [74] focused on vortex-induced vibrations of light structures and explored the critical mass phenomenon in the laminar flow regime. They estimated the cylinder response for different mass ratio values and suggested that large amplitude oscillations can be observed for all Reynolds numbers at sufficiently low mass ratio m^*. It was demonstrated that the transition from desynchronised response to lock-in state corresponding to a sharp amplitude increase only occurs for Reynolds numbers higher than a critical value Re_j. In this case, low amplitude oscillations are observed for $m^* > m^*_c$ but further decreasing the mass ratio to $m^* \leq m^*_c$ results in an abrupt jump in the vibration amplitude. Alternatively, for $Re < Re_j$ the amplitude of cylinder oscillation increases smoothly as m^* is reduced. It was suggested that the amplitude variation is associated with the different transitions between the lower branch response and the desynchronised state. The estimated value for the critical Reynolds number is in the interval $107 \leq Re_j \leq 110$. While the response for $Re < Re_j$ exhibits a single state for each m^*, multiple response states are reported for $Re > Re_j$ within a certain range of mass ratio m^*. The response branch for $Re > Re_j$ could be observed on the lower branch, initial branch (II) or in the desynchronised state, leading to hysteresis.

Additionally, VIV problems have been modelled using different IBM approaches in various numerical studies focusing on the flow past elastically mounted cylinders [73, 102, 109, 221–223]. In the present work, vortex-induced vibration problems are investigated to highlight the capabilities of the strongly coupled scheme in case of complex

physical phenomena. Particular attention is devoted to the critical-mass behaviour and to configurations involving small density ratios, where numerical instabilities typically arise.

7.3 Numerical Simulations

This section initially focuses on the classical problem of flow around a stationary cylinder at moderate Reynolds numbers to validate the model formulation and implementation. The geometry of the computational domain and the lattice resolution are tested, and results are compared to numerous experimental and numerical works. The numerical setup is then used to investigate the problem of vortex-induced vibrations for the case of a stationary cylinder that oscillates in the direction transverse to the flow. Building upon the work of Navrose and Mittal [74], the study focuses on the critical mass phenomenon in light structures, and the stability properties of the method are systematically tested for such problems.

All simulations are performed on a uniform lattice using the D2Q9 velocity set, with the collision operator defined by the central-moment lattice Boltzmann method (CLBM). The immersed boundary formulation implements a four-point regularised discrete delta function and a retraction distance of $r_\mathrm{d} = 0.4$. The strongly coupled IB–LBM scheme is considered.

7.3.1 Flow Past a Stationary Circular Cylinder

The current numerical implementation, geometry and resolution are investigated for the case of flow around a stationary circular cylinder. A circular cylinder of diameter D is positioned in a channel of width W and length L. A velocity inflow condition is prescribed at the inlet with an associated free-stream velocity U_0, while zero-gradient boundary conditions are applied at the upper and lower boundaries and at the outlet of the channel. The computational domain and fluid flow conditions used in the simulations are listed in Table 7.1. This choice of parameters allows a systematic comparison with several numerical [164, 224–228] and experimental results [229, 230]. The Reynolds

number is calculated using the free-stream velocity U_0 as the characteristic value, i.e. $Re = U_0 D/\nu$. The drag C_d and lift C_l coefficients are defined as

$$C_\mathrm{d} = \frac{2F_\mathrm{d}}{\rho_\mathrm{f} {U_0}^2 D} \qquad C_\mathrm{l} = \frac{2F_\mathrm{l}}{\rho_\mathrm{f} {U_0}^2 D}\,, \tag{7.1}$$

where F_d is the drag force and F_l is the lift force. The wall pressure coefficient C_p can be calculated in the following way

$$C_\mathrm{p} = \frac{p - p_0}{\frac{1}{2}\,\rho_\mathrm{f} {U_0}^2}\,, \tag{7.2}$$

where p_0 is the stagnation point pressure. In this section, it is considered a moderate Reynolds number flow, i.e. $50 \leq Re \leq 150$. This regime is characterised by boundary layer separation at both sides of the cylinder. The instability generates an oscillatory flow pattern in the wake region, which leads to the formation of a trail of vortices known as the *von Karman vortex street* [231]. At $Re \geq 100$ the vortices alternatively form and then shed, and their circular motion is stopped by viscous forces further downstream of the cylinder [232]. Another important nondimensional parameter used to characterise the oscillatory flow around a solid object is the Strouhal number St, which is defined as

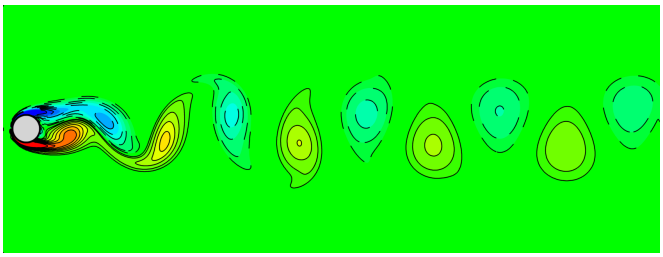
$$St = \frac{f_v D}{U_0}\,, \tag{7.3}$$

where f_v is the vortex shedding frequency. The Strouhal number relates the frequency of vortex shedding to the flow condition. The instantaneous vorticity contours plotted in Figure 7.1 show the formation of an array of periodic alternating vortices shed from the cylinder. The wake is characterised by regions of locally high vorticity forming vortices that alternatively rotate in opposite directions and travel downstream before being dissipated. The subsequent time steps illustrate the periodic formation of an attached vortex on one side of the cylinder while the eddy on the other side is being shed from the cylinder.

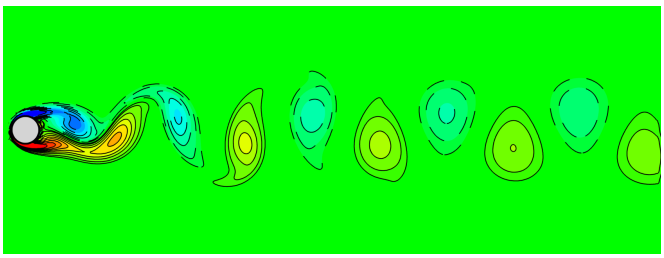
Vortex shedding results in an asymmetrical pressure distribution around the cylinder, which gives rise to an oscillating lift force. The lift force varies periodically with

Table 7.1: Geometry and fluid properties for flow past a cylinder simulations.

Geometry		Properties	
Diameter D	1	Density ρ_{f}	1
Channel length L	35.5	Velocity U_0	0.05
Channel width W	20	Reynolds number Re	100
Cylinder location (L, W)	$(10, 10)$		
Aspect ratio κ	0.05		



(a) $t = 400$.

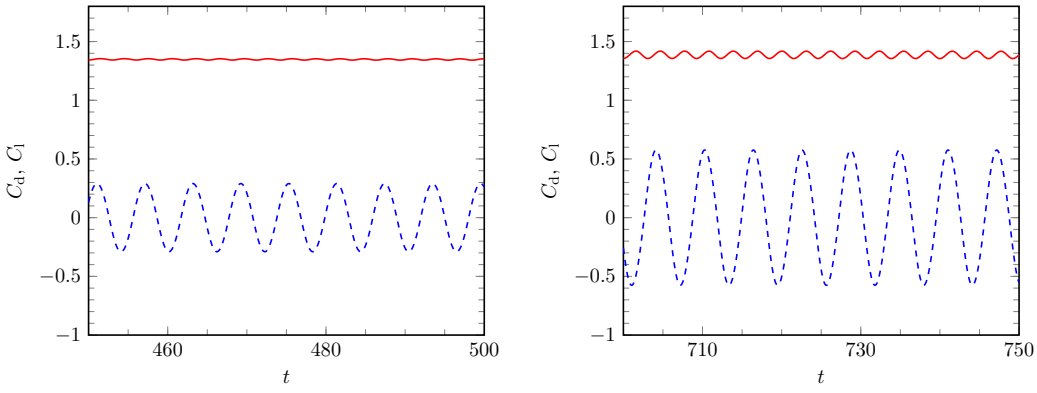


(b) $t = 500$.

Figure 7.1: Instantaneous vorticity contours for flow past a stationary cylinder at (a) $t = 400$ and (b) $t = 500$ for $Re = 100$ and $D = 10\Delta x$.

time and its frequency is related to the vortex oscillation, where one cycle corresponds to the distance between successive vortices of the same sign. Thus, the vortex shedding frequency can be calculated by operating a fast Fourier transform on the lift coefficient curves, and the result can be used to determine the Strouhal number of the flow. The periodic properties of the flow are reflected by the time-dependent drag C_{d} and lift C_{l} coefficients. The evolution in time of C_{d} and C_{l} is presented in Figure 7.2 for increasing values of Re.

Simulations are performed for increasing lattice resolution, i.e. $\Delta x = (D/5,\ D/10,\ D/20,\ D/40)$. The effects of the spatial resolutions on the drag coefficient C_{d}, lift coefficient C_{l}, and Strouhal number St are presented in Table 7.2 for the case of $Re =$



(a) $Re = 100$. (b) $Re = 150$.

Figure 7.2: Time evolution of the drag C_d (−) and lift C_l (−−) coefficients for flow past a stationary cylinder at (a) $Re = 100$ and (b) $Re = 150$.

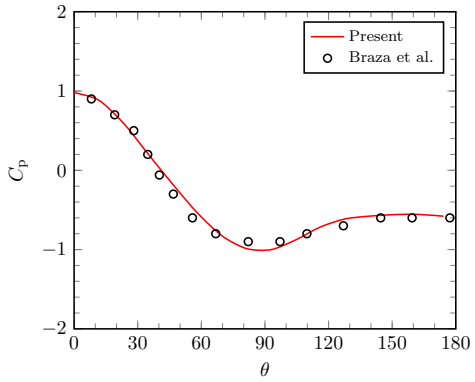


Figure 7.3: Pressure distribution on the surface of the cylinder for $Re = 100$ and $D = 10\Delta x$.

100. The results suggest that even smaller lattice sizes are capable of capturing the main flow features while saving computational time. To evaluate the current model, the present results are compared to different numerical and experimental studies listed in Table 7.2. The results show good agreement for all the flow characteristic parameters considered in this study.

In Figure 7.3, the pressure coefficient C_p at $Re = 100$ is plotted at different radial positions θ, where $\theta = 0$ corresponds to the stagnation point. The current numerical method shows a satisfactory agreement with the numerical results presented by Braza et al. [224].

Table 7.2: Flow around a stationary cylinder: comparison of the drag coefficient C_d, lift coefficient C_l, and Strouhal number St for $Re = 100$. The present results are reported for different lattice resolutions $D/\Delta x$. Additional numerical and experimental results are given for comparison.

Study	$D/\Delta x$	C_d		C_l	St
Present	5	1.140	± 0.016	± 0.160	0.141
	10	1.320	± 0.013	± 0.300	0.162
	20	1.334	± 0.011	± 0.290	0.165
	40	1.334	± 0.009	± 0.290	0.166
Braza et al. [224]		1.36	± 0.015	± 0.293	0.160
Mittal et al. [225]		1.33		± 0.326	0.163
Liu et al. [226]		1.350	± 0.012	± 0.339	0.165
Kim et al. [227]		1.33		± 0.32	0.165
Wu and Shu [164]		1.364		± 0.344	0.163
Le et al. [228]		1.39	± 0.009	± 0.323	0.160
Williamson [229]					0.164
Roshko [230]					0.165

7.3.2 Vortex-induced Vibrations of a Circular Cylinder

This study considers a one-degree-of-freedom system that is only allowed to move in the direction transverse to the flow. Applying a lumped parameter approach, a vibrating cylinder can be modelled as a linear spring-dashpot system [231,233]. This configuration is schematically illustrated in Figure 7.4. The governing equation of motion in the case of a one-degree-of-freedom system undergoing self-induced oscillation is expressed by the following differential equation

$$m\ddot{y} + c\dot{y} + ky = F_y(t) \tag{7.4}$$

where m, c, and k are respectively the mass of the solid object, the structural damping and the stiffness. The terms on the left-hand side correspond to the inertia force, the structural damping force, and the restoring force, respectively. The overdots indicate differentiation with respect to t, corresponding to velocity $\dot{y}$ and acceleration $\ddot{y}$. F_y is the self-induced oscillation force exerted on the solid object in the transverse direction. An important characteristic parameter of this system is the natural frequency of the

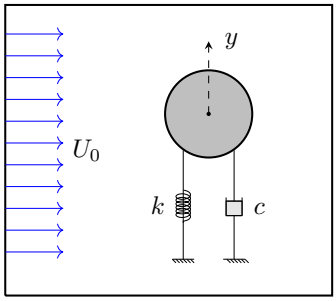


Figure 7.4: Schematic representation of the one-degree-of-freedom spring–dashpot model used to describe the transverse motion of a vibrating cylinder in crossflow.

oscillator in vacuum f_n defined as

$$f_n = \frac{1}{2\pi}\sqrt{\frac{k}{m}} \tag{7.5}$$

Equation 7.4 can be written in the following nondimensional form [74]

$$\ddot{Y} + 4\pi\, F_n\, \zeta \dot{Y} + (2\pi\, F_n)^2\, Y = \frac{2\, C_\mathrm{l}}{\pi\, m^*} \tag{7.6}$$

where Y is the nondimensional displacement of the object, F_n is the nondimensional natural frequency of the oscillator, $\zeta = c/\left(2\sqrt{km}\right)$ is the damping coefficient, and $m^* = 4m/\left(\pi\, \rho_\mathrm{f}\, D^2\right)$ is the mass ratio. In the following study, both the structural damping force and the restoring force are set to zero to investigate a limiting case.

The geometry and parameters considered for this problem are the same as the stationary case and they are listed in Table 7.1. This setup enables a meaningful comparison with the numerical results of Navrose and Mittal [74]. This work investigates the free vibration of a circular cylinder in a uniform flow for various mass ratios m^*, focusing on moderate Reynolds number values, i.e. $Re = 100$ and $Re = 150$. In particular, the amplitude of vibration patterns and the critical mass phenomenon are explored in detail. Based on the successful validation for the case of a stationary cylinder, the lattice resolution considered in this study is $\Delta x = D/10$ and the mass ratio values explored are in the range $0.08 \leq m^* \leq 1$.

In the flow regime relevant to the present study (i.e. $40 \leq Re \leq 150$), vortex-induced vibrations are characterised by laminar wake dynamics that determine different

structural response behaviours. As discussed in Section 2.5, the wake is dominated by the 2S (two single vortices) shedding mode, where alternating clockwise and counter-clockwise vortices are shed each cycle. In this regime, the structural response is associated with different branches depending on the reduced velocity U^*. When the system is in a desynchronised state, the vortex shedding frequency adapts to the cylinder motion but does not become phase-locked with it, resulting in low-amplitude oscillations. In the synchronised state, the vortex shedding frequency matches the natural oscillation frequency, and the resulting lock-in structural response exhibits three characteristic branches: initial branch I (IB(I)), lower branch (LB), and initial branch II (IB(II)).

For the case of $Re = 100$, the variation of the nondimensional amplitude of cylinder oscillation with mass ratio is presented in Figure 7.5. The current results show a satisfactory match with the numerical study presented in Ref. [74]. It is worth noting that the variation of the nondimensional amplitude with mass ratio is smooth, and no jump in the response is detected. The vertical displacement of the cylinder and the time evolution of its oscillatory pattern are shown in detail in Figure 7.6 for consecutive values of the mass ratio m^*. It is shown that the amplitude of oscillation increases as the mass ratio decreases from $m^* = 0.1$ to $m^* = 0.08$, but the transition is smooth and there are no jumps in the response. This behaviour is consistent with the response-branch structure reported for VIV at this Reynolds number [74]. The flow at $Re = 100$ supports only a single stable synchronised response branch, namely the lower lock-in branch (LB). As a result, the increasing influence of the fluid forcing on the body motion leads to a gradual strengthening of the vibration response as m^* decreases, producing a smooth increase in oscillation amplitude without any abrupt change in the underlying dynamics.

Then, the Reynolds number is increased to $Re = 150$ by increasing the free-stream velocity. The corresponding results for the nondimensional amplitude of cylinder oscillation with different values of mass ratio in the interval $0.08 \leq m^* \leq 1$ are shown in Figure 7.7. At this Reynolds number, the amplitude response variation with mass ratio exhibits a markedly different behaviour compared to the $Re = 100$ case. For mass ratios $m^* \geq 0.09$, the oscillation amplitude remains nearly constant at a low value

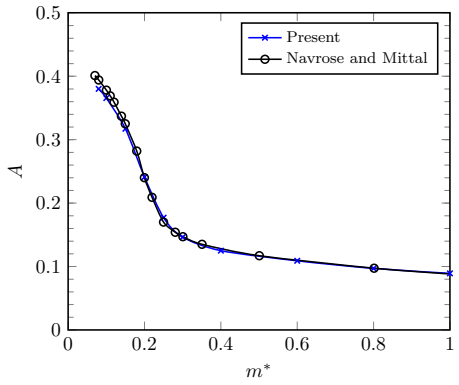
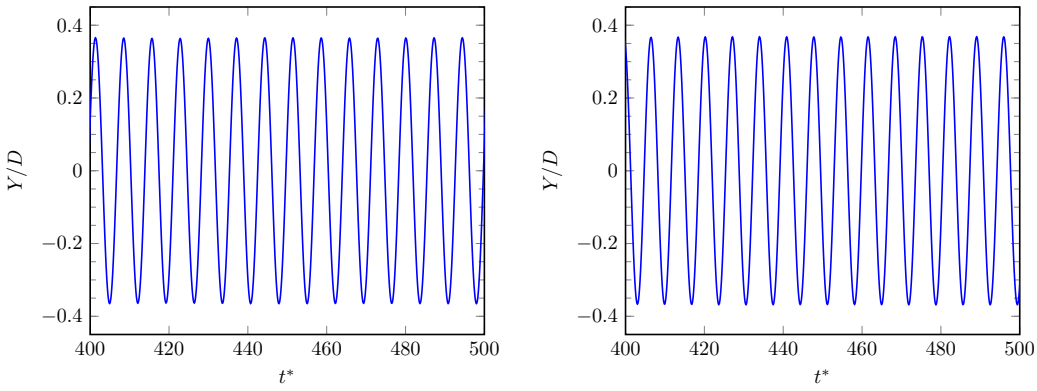


Figure 7.5: Variation of the nondimensional amplitude of cylinder oscillation with mass ratio for $Re = 100$. Numerical results by Navrose and Mittal [74] are given for comparison.



(a) $m^* = 0.1$. (b) $m^* = 0.08$.

Figure 7.6: Flow past a vibrating cylinder at $Re = 100$: time evolution of the cylinder vertical displacement for mass ratios (a) $m^* = 0.1$ and (b) $m^* = 0.08$.

($A \approx 0.1$), characteristic of the low-amplitude desynchronised branch (DS(II)). When the mass ratio is reduced to $m^* = 0.08$, the response exhibits an abrupt increase of approximately $\Delta A \approx 0.12$, determining a jump in the structural response. This sharp discontinuity contrasts with the smooth amplitude variation observed at $Re = 100$, and it is interpreted as a shift from the low-amplitude desynchronized branch (DS(II)) to the lock-in response on initial branch II (IB(II)). The onset of this branch transition identifies a critical mass ratio below which the fluid–structure coupling becomes significantly stronger.

To further illustrate the change in oscillation characteristics, the time evolution of

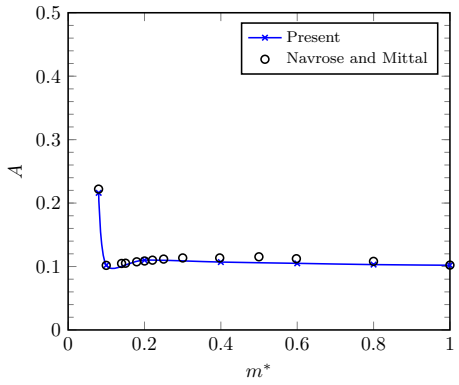
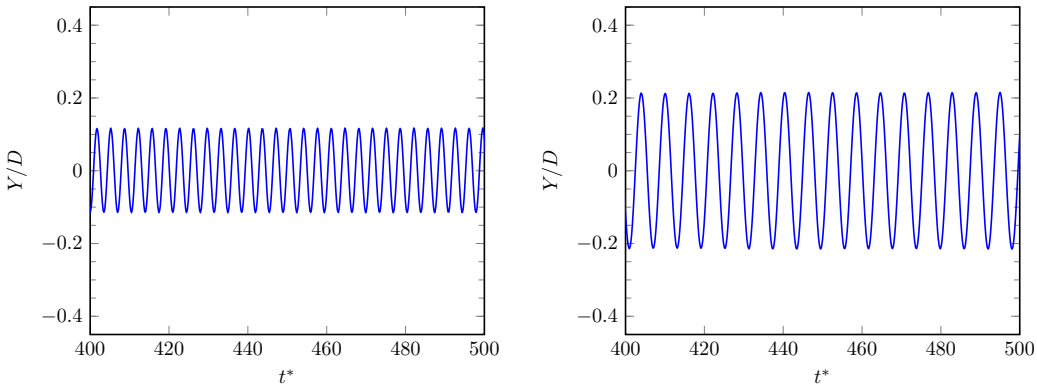


Figure 7.7: Variation of the nondimensional amplitude of cylinder oscillation with mass ratio for $Re = 150$. Numerical results by Navrose and Mittal [74] are given for comparison.



(a) $m^* = 0.1$. (b) $m^* = 0.08$.

Figure 7.8: Flow past a vibrating cylinder at $Re = 150$: time evolution of the cylinder vertical displacement for mass ratios (a) $m^* = 0.1$ and (b) $m^* = 0.08$.

the cylinder vertical displacement for $m^* = 0.1$ and $m^* = 0.08$ is shown in Figure 7.8. Although the vertical displacement varies nearly sinusoidally in both cases, the oscillation for $m^* = 0.08$ clearly shows a larger amplitude than that for $m^* = 0.1$. This comparison highlights the increase in structural response that occurs as the mass ratio is reduced. Thus, it can be concluded that the critical mass ratio m^*_c phenomenon is observed at $Re = 150$ and its value is $m^*_c = 0.08$.

The amplitude of cylinder oscillation for different Reynolds numbers is presented in Figure 7.9. This comparison highlights that the relationship between oscillation amplitude and mass ratio depends strongly on Re, with significantly different trends

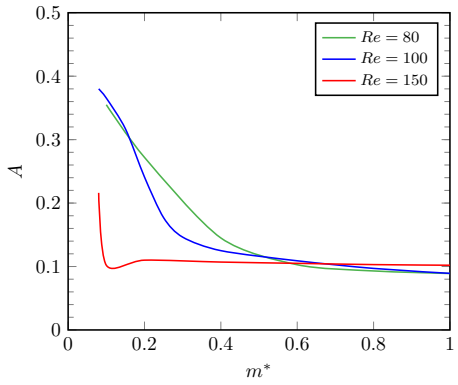


Figure 7.9: Variation of the nondimensional amplitude of cylinder oscillation with mass ratio for different Reynolds numbers.

emerging across the flow regime considered. For $Re = 80$ and $Re = 100$, the vibration amplitude increases smoothly with decreasing mass ratio, and no abrupt transition is observed. This behaviour indicates that the synchronised response at these Reynolds number values is restricted to the lower branch (LB) without the emergence of additional lock-in branches. In contrast, the curve corresponding to $Re = 150$ displays a distinct jump at $m^* = 0.08$, reflecting a sudden transition from the desynchronised branch DS(II) to the higher-amplitude lock-in response on the initial branch II (IB(II)). This identifies a critical mass ratio for the onset of large-amplitude oscillation at this Reynolds number. These observations are consistent with the findings of Ref. [74], which show that a critical mass ratio m_c^* can be defined only for Reynolds numbers above a threshold value Re_j. For cases where $Re < Re_j$, the amplitude of cylinder oscillation varies smoothly with mass ratio, and the critical mass ratio cannot be defined.

The present analysis extends the understanding of vortex-induced vibrations in the laminar regime and demonstrates that the proposed coupling strategy can accurately resolve the underlying FSI dynamics. The numerical results successfully capture the characteristic branch structure of the structural response and the associated wake–body synchronisation mechanisms in this regime. The results confirm that the critical mass ratio emerges only beyond a threshold Reynolds number value Re_j. An additional noteworthy outcome is the robustness of the strong-coupling formulation at very low mass ratios ($m^* \lesssim 0.1$), a parameter range in which weakly coupled IB–LBM schemes

are typically affected by instabilities related to the internal mass effect. The present approach therefore addresses both the physical and numerical challenges associated with the behaviour of light structures at moderate Reynolds numbers and provides a robust framework for analysing VIV problems.

7.4 Conclusions

The objective of this chapter was to investigate vortex-induced vibrations using a strongly coupled IB–LBM framework. The numerical setup and spatial resolution were first verified using the canonical case of flow past a stationary circular cylinder. Then, the method was applied to the vibration of a freely oscillating cylinder in uniform flow over a range of Reynolds numbers and mass ratios. The simulations captured response branches and lock-in behaviour and indicated the emergence of a critical mass ratio only above a threshold Reynolds number. Importantly, the formulation remained stable and accurate at very low mass ratios, where weakly coupled schemes become unstable. These results show that the strong coupling enables stable and accurate simulation of VIV phenomena in the laminar regime and provides a solid foundation for its application to further FSI problems.

Chapter 8

Conclusions and Future Work

This chapter consolidates the main outcomes of this work and reflects on their significance for the numerical modelling of fluid–structure interaction within the lattice Boltzmann framework. The principal contributions are summarised in Section 8.1, highlighting the development of numerical strategies, their application to challenging FSI problems, and the insights into interface diffusion, coupling stability, and the dynamics of light structures. Building on these findings, Section 8.2 outlines potential directions for future research and identifies extensions that could further enhance the capability and applicability of the proposed methodologies.

8.1 Concluding Remarks and Contributions

The research conducted in this thesis contributed to the understanding of FSI problems that are relevant in important engineering applications and natural phenomena. The necessity and significance of developing advanced numerical tools were emphasised by describing their utility in design optimisation and performance evaluation processes.

The numerical framework adopted in this work was chosen to address the limitations of conventional macroscopic methods. The lattice Boltzmann method was shown to provide an effective approach owing to its simple implementation, suitability for GPU architectures, and ability to capture mesoscopic effects. Particular attention was paid to collision models and forcing schemes, confirming the advantages of the central-moment

formulation in terms of stability.

Fluid–solid coupling was realised through the immersed boundary method, incorporating a multi-direct-forcing scheme for accurate enforcement of the no-slip condition and a relaxation scheme to improve computational efficiency. The internal-mass effect was analysed in detail, and a strongly coupled IB–LBM formulation was implemented to improve numerical stability.

The discrete element method was incorporated to model particle interactions and contact forces, completing a combined DEM–IB–CLBM approach to simulate complex FSI simulations. Building on this numerical framework, this thesis has advanced the modelling of fluid–structure interaction problems by developing and analysing IB-LBM strategies for cases involving light and moving structures. In particular, the principal results lead to contributions across the following aspects.

Interface diffusion and boundary representation

This work addressed the diffuse representation of the fluid-solid interface that characterises the selected IBM algorithm. It was explained that for moving boundary problems, the diffuse interface successfully suppresses spurious numerical oscillations that affect different sharp-interface methods. However, since the diffuse-interface approach changes both the apparent size of the solid object and the exact surface location, further studies on its influence were conducted. This work considered four benchmark problems to investigate the effects of interface diffusion: flow past a cylinder, settling of a particle under gravity, flow around two impacting particles, and drafting-kissing-tumbling of two particles.

It was determined that the diffuse interface has a negligible impact on problems characterised by unconfined flows. In particular, the study of the flow past a cylinder proved that the diffuse interface does not cause significant numerical error for problems involving fixed unbounded geometries. However, the investigation of the remaining test cases indicated that confined geometries accentuate interface diffusion effects, reducing the numerical accuracy of diffuse-interface IBM compared to sharp-interface methods. The cases selected in this work consider both a fixed and a moving geometry in the

creeping laminar flow regime. Having established the influence of bounding walls on the characteristic features of the flow field, it is of central importance to investigate the influence of larger degrees of confinement. The same problems were studied considering different confinement ratio values, demonstrating that a larger confinement accentuates interface diffusion in IB-LBM simulations.

To further analyse the interface diffusion effects, problems involving interactions between particles were considered. The flow around two impacting particles was chosen to investigate the case of moving objects with a variable confinement. It was noted that when particles are in close contact, the numerical diffusion causes an overlap between their interfaces. The simulations highlighted that as particles approach each other, the diffuse interface has an increasingly significant impact on the accuracy of the results. The drafting-kissing-tumbling process of two particles settling in a channel was selected because it adds further complexity by considering a contact stage and a collision between the particles. This problem confirmed that numerical accuracy is significantly affected by interface diffusion.

Taking those results into account, a boundary retraction approach was considered as an error mitigation strategy. It was demonstrated that this approach improves the representation of the solid boundary while limiting the additional computational costs. The results showed that the multi-direct-forcing IBM with boundary retraction achieves a better performance for significantly confined geometries and particle interaction problems. The evaluation of the results in different test cases indicated the optimal retraction distance as $r_\mathrm{d} = 0.4$, which is to be doubled in case of overlapping interfaces.

Numerical Stability and Coupling Strategies

Another objective of this work was to improve the understanding of the strategies for coupling fluid and structure equations, focusing on the strongly coupled IB-LBM. It was suggested that the internal mass effect influences the numerical stability of weakly coupled IBM schemes and imposes a limitation on the fluid-solid density ratio. Additionally, it was indicated that numerical stability is affected by both the local conditions of the fluid and structural properties such as density and geometry. A comparison be-

tween the capabilities of weakly coupled and strongly coupled IB-LBM schemes was conducted for the case of falling and rising particles in the creeping flow regime, considering increasingly smaller solid density values. The weakly coupled scheme was found to be affected by numerical stability issues in cases where the density ratio was around unity. It was shown that the stability can be improved by increasing the lattice grid size, but $\rho_s/\rho_f = 1.01$ was established as the limiting density ratio for the weakly coupled scheme. Conversely, the strongly coupled IB-LBM was able to achieve stable simulations for light solids, successfully capturing the dynamics of rising particles. The case of falling and rising particles and single particle released off-centre were considered to investigate the effect of the Reynolds number and more complex flow structures. Additionally, multiple particles rising were simulated to evaluate computational efficiency. The strongly coupled IB-LBM scheme provided satisfactory results for all test cases, extending the numerical stability properties.

Dynamics of Light Structures and Vortex-Induced Vibrations

An important aim of this study was to investigate fluid–structure interaction problems involving light structures across different configurations. The simulations of falling and rising particles explored the effects of structural parameters, flow conditions, and geometrical confinement. The results provided insight into the resulting trajectories and flow patterns across a range of operating conditions.

Finally, the vortex-induced vibration problem was explored to demonstrate the ability of the strong coupling to capture complex flow phenomena that occur in systems involving light structures. The simulations investigated the characteristic vibration response of the system, including the development of synchronised states and transitions between distinct branches. A critical mass effect was also observed, showing that the vibration response depends on both the mass ratio and the characteristics of the surrounding flow. The studies conducted in this work contributed to demonstrating the capabilities of the strong coupling in terms of both stability and computational efficiency.

8.2 Future work

Based on the research developed in this thesis, different future studies can be suggested.

Extension to Non-Circular and Complex Particle Geometries

Building on the analysis of diffuse interfaces and the implementation of the boundary-retraction strategy, an important next step is to extend the methods presented in this thesis to simulate the dynamics of non-circular particles. This would clarify the dependence of diffuse-interface effects on structural geometry and assess the performance of the boundary-retraction approach in more complex configurations. In particular, particle–particle interactions and collisions should be considered to establish the effect of the overlapping interfaces.

Such configurations would also enable a systematic assessment of the influence of structural geometry on numerical stability and on the density ratio limits of the method. In this context, the presence of non-circular shapes introduces further complexity during particle–particle and particle–wall collisions, where orientation dependency can significantly affect the contact force calculation [234].

In addition to numerical challenges, non-circular and arbitrarily shaped particles introduce further complexity in the underlying physics. Existing studies indicate that such geometries strongly influence wake formation, lateral migration, and settling behaviour, leading to results that cannot be reproduced with circular geometries [235, 236]. The capability to model these cases is of practical significance, as non-circular particulate flows occur in numerous processes and phenomena.

Inclusion of Rotational Dynamics

This work primarily addressed configurations in which rotational motion was limited, and the internal mass contribution could be treated accordingly. Another challenging problem that would further strengthen the capabilities of the strongly coupled IB-LBM scheme is to consider cases in which the solid undergoes significant rotation. This would allow a more rigorous assessment of the internal-mass formulation, particularly

in relation to the expression of the torque associated with the internal fluid. This contribution is only approximate, being derived under the assumption of rigid-body motion throughout the solid volume and not accounting for the actual motion of the fluid inside that region. In this context, the influence of rotation on stability and density-ratio limits should be examined.

In the context of vortex-induced vibrations, the inclusion of rotation would introduce an additional level of physical complexity. Previous studies [237, 238] have shown that rotation alters the synchronisation range and can produce significantly larger vibration amplitudes. It also generates distinct wake patterns with asymmetric vortex arrangements, and regimes in which oscillations occur even in the absence of vortex shedding. These phenomena directly affect the phasing between forces and structural response and fundamentally modify the vibration mechanisms. Within the present framework, investigating such configurations would therefore extend the analysis of the critical-mass effect to cases in which rotation plays a significant role.

Progression Towards Application-Oriented Configurations

The investigation of the critical-mass effect described in this work focused mainly on configurations with simplified structural behaviour. In practice, structural damping and stiffness significantly influence the response, modifying the lock-in regime, branch transitions, and vibration amplitudes [74]. Introducing more complex structural models into the present framework would therefore extend the analysis to conditions closer to representative applications [71, 237].

The findings presented in this work were assessed in two-dimensional settings, which offered a well-defined framework for developing methods, analysing interface representation and coupling strategies, and interpreting the behaviour of light structures. However, many FSI problems of interest display characteristics that are inherently three-dimensional. Freely rising and falling particles develop features absent in two-dimensional models [239], and in vortex-induced vibrations the onset of three-dimensional transition strongly influences the underlying physics [237]. Owing to the increasing growth of computational power and the possibility of leveraging GPU architectures,

the present framework could be realistically extended to three-dimensional simulations. Such an extension would also complement the enhanced structural modelling previously discussed, moving the methodology closer to application-relevant engineering systems. Three-dimensional simulations would also facilitate more direct comparison with experimental studies, such as particulate flows [239, 240] and on flow-induced vibrations [71, 241].

From a numerical standpoint, this extension would also intersect with ongoing developments in immersed-boundary approaches, particularly regarding the distribution of Lagrangian marker points on complex particle surfaces, which remains a central challenge in three-dimensional IBM and is closely linked to accurate treatment of inter-particle collisions within DEM frameworks [242]. In addition, a three-dimensional implementation would make it possible to evaluate the computational performance and scalability of the approach on modern platforms.

Overall, these developments would advance the present methodology towards application-oriented configurations, linking the numerical analysis more closely to experimentally accessible cases, while preserving a rigorous foundation for physical interpretation.

Appendix A

Boundary Retraction Scheme Implementation

In both the weak and strong coupling solvers, the boundary retraction scheme used in this work is implemented directly in the construction of the immersed-boundary (IBM) geometry for rigid particles. Instead of placing Lagrangian points on the physical surface of a particle, they are retracted inwards by a prescribed distance r_{d}. The implementation is presented in structured algorithmic form in Algorithm 1, capturing the essential computational logic.

Geometry allocation. During the initialisation stage, a DEM–IBM preparation routine determines for each rigid particle the number of Lagrangian boundary points required on the retracted surface. This number is computed from the effective surface size and the target spacing. A cumulative array is then assembled and stored in the IBM data structure.

Geometry update. At every time step, the IBM geometry module uses the cumulative array, together with the current particle centre and the effective radius, in order to construct the position of the boundary point on the retracted surface, and update the corresponding entries. In this way, the retraction distance enters the IBM formulation through the geometry and all subsequent interpolation and force spreading operate on

this retracted surface.

Algorithm 1: Construction of Lagrangian points on a retracted surface

Require: number of solids `nb`

Require: geometry descriptors `geomType[p]`, `geomData[p]`

Require: rigid–body state `center[p]`, `orient[p]`, `vel[p]`, `omega[p]`

Require: target spacing `ds`

Require: retraction distance `r_d`

```
// Geometry allocation
for p = 1 to nb do
  nl[p] = lagCount(geomType[p], geomData[p], r_d, ds)
  lag[p] = lag[p-1] + nl[p]
end for
// Geometry update
for p = 1 to nb do
  for j = 0 to nl[p]-1 do
    k = lag[p-1] + j
    (x_s, n_s, w_s) = surfaceIBM(geomType[p], geomData[p], center[p],
    orient[p], j)
    x_ib = x_s - r_d * n_s
    u_ib = vel[p] + omega[p] × (x_ib - center[p])
    ibPos[k] = x_ib
    ibVel[k] = u_ib
    ibSpacing[k] = w_s
    ibVol[k] = Vol(geomType[p], geomData[p], r_d, j)
  end for
end for
```

Bibliography

[1] F. Sotiropoulos and X. Yang, "Immersed boundary methods for simulating fluid–structure interaction," *Progress in Aerospace Sciences*, vol. 65, pp. 1–21, 2014.

[2] C. K. Aidun and J. R. Clausen, "Lattice-Boltzmann method for complex flows," *Annual Review of Fluid Mechanics*, vol. 42, pp. 439–472, 2010.

[3] W. Kim and H. Choi, "Immersed boundary methods for fluid-structure interaction: A review," *International Journal of Heat and Fluid Flow*, vol. 75, pp. 301–309, 2019.

[4] T. Nakamura, S. Kaneko, F. Inada, M. Kato, K. Ishihara, T. Nishihara, N. W. Mureithi, and M. A. Langthjem, *Flow-Induced Vibrations: Classifications and Lessons From Practical Experiences.* Elsevier, 2013.

[5] D. A. Rubenstein, W. Yin, and M. D. Frame, *Biofluid Mechanics.* Academic Press, 2015.

[6] F. Sotiropoulos and I. Borazjani, "A review of state-of-the-art numerical methods for simulating flow through mechanical heart valves," *Medical & Biological Engineering & Computing*, vol. 47, no. 3, pp. 245–256, 2009.

[7] G. Karniadakis, A. Beskok, and N. Aluru, *Microflows and Nanoflows: Fundamentals and Applications.* Springer, 2005.

[8] R. Kamakoti and W. Shyy, "Fluid–structure interaction for aeroelastic applications," *Progress in Aerospace Sciences*, vol. 40, no. 8, pp. 535–558, 2004.

[9] Y. Li and X. Shan, "Lattice Boltzmann method for adiabatic acoustics," *Philosophical Transactions of the Royal Society A: Mathematical, Physical and Engineering Sciences*, vol. 369, no. 1944, pp. 2371–2380, 2011.

[10] G. Hou, J. Wang, and A. Layton, "Numerical methods for fluid-structure interaction—a review," *Communications in Computational Physics*, vol. 12, no. 2, pp. 337–377, 2012.

[11] Y. Tominaga and T. Stathopoulos, "CFD simulation of near-field pollutant dispersion in the urban environment: A review of current modeling techniques," *Atmospheric Environment*, vol. 79, pp. 716–730, 2013.

[12] S. Di Sabatino, R. Buccolieri, B. Pulvirenti, and R. Britter, "Simulations of pollutant dispersion within idealised urban-type geometries with CFD and integral models," *Atmospheric Environment*, vol. 41, no. 37, pp. 8316–8329, 2007.

[13] T. Zhao, G. T. Houlsby, and S. Utili, "Investigation of granular batch sedimentation via DEM–CFD coupling," *Granular Matter*, vol. 16, no. 6, pp. 921–932, 2014.

[14] P. Zahedi, J. Zhang, H. Arabnejad, B. S. McLaury, and S. A. Shirazi, "CFD simulation of multiphase flows and erosion predictions under annular flow and low liquid loading conditions," *Wear*, vol. 376-377, pp. 1260–1270, 2017.

[15] H.-C. Zheng, Z.-M. Shi, M. Peng, and S.-B. Yu, "Coupled CFD-DEM model for the direct numerical simulation of sediment bed erosion by viscous shear flow," *Engineering Geology*, vol. 245, pp. 309–321, 2018.

[16] A. Mansouri, H. Arabnejad, S. Shirazi, and B. McLaury, "A combined CFD/experimental methodology for erosion prediction," *Wear*, vol. 332-333, pp. 1090–1097, 2015.

[17] A. Kubilay, D. Derome, B. Blocken, and J. Carmeliet, "CFD simulation and validation of wind-driven rain on a building facade with an Eulerian multiphase model," *Building and Environment*, vol. 61, pp. 69–81, 2013.

[18] T. Esposti Ongaro, C. Cavazzoni, G. Erbacci, A. Neri, and M. Salvetti, "A parallel multiphase flow code for the 3D simulation of explosive volcanic eruptions," *Parallel Computing*, vol. 33, no. 7, pp. 541–560, 2007.

[19] G. Tian, M. Hindle, S. Lee, and P. W. Longest, "Validating CFD predictions of pharmaceutical aerosol deposition with in vivo data," *Pharmaceutical Research*, vol. 32, no. 10, pp. 3170–3187, 2015.

[20] S. R. Idelsohn, J. M. Gimenez, R. Löhner, and E. Oñate, "A multiscale approach for the study of particle-laden flows using a continuous model," *Computer Methods in Applied Mechanics and Engineering*, vol. 401, p. 115174, 2022.

[21] F. Mashayek and R. Pandya, "Analytical description of particle/droplet-laden turbulent flows," *Progress in Energy and Combustion Science*, vol. 29, no. 4, pp. 329–378, 2003.

[22] S. K. Friedlander *et al.*, *Smoke, Dust, and Haze*. Oxford University Press, 2000.

[23] C. T. Crowe, J. D. Schwarzkopf, M. Sommerfeld, and Y. Tsuji, *Multiphase Flows with Droplets and Particles*. CRC Press, 2011.

[24] M. Yang, J. Zhang, S. Zhong, T. Li, T. Løvås, H. Fatehi, and X.-S. Bai, "CFD modeling of biomass combustion and gasification in fluidized bed reactors using a distribution kernel method," *Combustion and Flame*, vol. 236, p. 111744, 2022.

[25] B. Xu and A. Yu, "Numerical simulation of the gas-solid flow in a fluidized bed by combining discrete particle method with computational fluid dynamics," *Chemical Engineering Science*, vol. 52, no. 16, pp. 2785–2809, 1997.

[26] D. Gidaspow, *Multiphase Flow and Fluidization: Continuum and Kinetic Theory Descriptions*. Academic Press, 1994.

[27] Y. Modarres-Sadeghi, *Introduction to Fluid-Structure Interactions*. Springer International Publishing, 2021.

[28] T. Sarpkaya, "A critical review of the intrinsic nature of vortex-induced vibrations," *Journal of Fluids and Structures*, vol. 19, no. 4, pp. 389–447, 2004.

[29] A. Jain, N. P. Jones, and R. H. Scanlan, "Coupled flutter and buffeting analysis of long-span bridges," *Journal of Structural Engineering*, vol. 122, no. 7, pp. 716–725, 1996.

[30] J. N. Yang, A. K. Agrawal, B. Samali, and J.-C. Wu, "Benchmark problem for response control of wind-excited tall buildings," *Journal of Engineering Mechanics*, vol. 130, no. 4, pp. 437–446, 2004.

[31] K.-S. Hong and U. H. Shah, "Vortex-induced vibrations and control of marine risers: A review," *Ocean Engineering*, vol. 152, pp. 300–315, 2018.

[32] G. R. Pirrung, C. Grinderslev, N. N. Sørensen, and R. Riva, "Vortex-induced vibrations of wind turbines: From single blade to full rotor simulations," *Renewable Energy*, vol. 226, p. 120381, 2024.

[33] H. Ren, M. Zhang, J. Cheng, P. Cao, Y. Xu, S. Fu, and C. Liu, "Experimental investigation on vortex-induced vibration of a flexible pipe under higher mode in an oscillatory flow," *Journal of Marine Science and Engineering*, vol. 8, no. 6, p. 408, 2020.

[34] S. Kang, I. Borazjani, J. A. Colby, and F. Sotiropoulos, "Numerical simulation of 3D flow past a real-life marine hydrokinetic turbine," *Advances in Water Resources*, vol. 39, pp. 33–43, 2012.

[35] J. Arrigan, V. Pakrashi, B. Basu, and S. Nagarajaiah, "Control of flapwise vibrations in wind turbine blades using semi-active tuned mass dampers," *Structural Control and Health Monitoring*, vol. 18, no. 8, pp. 840–851, 2011.

[36] Z. Mao, R. Tao, F. Chen, H. Bi, J. Cao, Y. Luo, H. Fan, and Z. Wang, "Investigation of the starting-up axial hydraulic force and structure characteristics of pump turbine in pump mode," *Journal of Marine Science and Engineering*, vol. 9, no. 2, p. 158, 2021.

[37] E. H. Dowell and K. C. Hall, "Modeling of fluid–structure interaction," *Annual Review of Fluid Mechanics*, vol. 33, pp. 445–490, 2001.

[38] Y. Bazilevs, K. Takizawa, and T. E. Tezduyar, *Computational Fluid–Structure Interaction*. John Wiley & Sons, 2013.

[39] S. Succi, *The Lattice Boltzmann Equation: For Complex States of Flowing Matter*. Oxford University Press, 2018.

[40] C. Thornton, *Granular Dynamics, Contact Mechanics and Particle System Simulations: A DEM study*. Springer International Publishing, 2015.

[41] Z. G. Feng and E. E. Michaelides, "The immersed boundary-lattice Boltzmann method for solving fluid-particles interaction problems," *Journal of Computational Physics*, vol. 195, no. 2, pp. 602–628, 2004.

[42] J. H. Ferziger, M. Perić, and R. L. Street, *Computational Methods for Fluid Dynamics*. Springer, 2019.

[43] I. Borazjani, L. Ge, and F. Sotiropoulos, "Curvilinear immersed boundary method for simulating fluid structure interaction with complex 3D rigid bodies," *Journal of Computational Physics*, vol. 227, pp. 7587–7620, 2008.

[44] S. Chen and G. D. Doolen, "Lattice Boltzmann method for fluid flows," *Annual review of fluid mechanics*, vol. 30, no. 1, pp. 329–364, 1998.

[45] X. D. Niu, C. Shu, Y. T. Chew, and Y. Peng, "A momentum exchange-based immersed boundary-lattice Boltzmann method for simulating incompressible viscous flows," *Physics Letters, Section A: General, Atomic and Solid State Physics*, vol. 354, no. 3, pp. 173–182, 2006.

[46] Y. Zhang, G. Pan, Y. Zhang, and S. Haeri, "A relaxed multi-direct-forcing immersed boundary-cascaded lattice Boltzmann method accelerated on GPU," *Computer Physics Communications*, vol. 248, p. 106980, 2020.

[47] W.-X. Huang and F.-B. Tian, "Recent trends and progress in the immersed boundary method," *Proceedings of the Institution of Mechanical Engineers, Part C: Journal of Mechanical Engineering Science*, vol. 233, pp. 7617–7636, 2019.

[48] T. Krüger, H. Kusumaatmaja, A. Kuzmin, O. Shardt, G. Silva, and E. Viggen, *The Lattice Boltzmann Method: Principles and Practice*. Springer International Publishing, 2017.

[49] C. Fang, *An Introduction to Fluid Mechanics*. Springer International Publishing, 2019.

[50] A. Bhagat, H. Gijare, and N. Dongari, "Modeling of Knudsen layer effects in the micro-scale backward-facing step in the slip flow regime," *Micromachines*, vol. 10, no. 2, p. 118, 2019.

[51] P. A. Chambre and S. A. Schaaf, *Flow of Rarefied Gases*. Princeton University Press, 1961.

[52] R. N. Moghaddam and M. Jamiolahmady, "Slip flow in porous media," *Fuel*, vol. 173, pp. 298–310, 2016.

[53] S. Roy, R. Raju, H. F. Chuang, B. A. Cruden, and M. Meyyappan, "Modeling gas flow through microchannels and nanopores," *Journal of applied physics*, vol. 93, no. 8, pp. 4870–4879, 2003.

[54] J. Galvin, C. Hrenya, and R. Wildman, "On the role of the Knudsen layer in rapid granular flows," *Journal of Fluid Mechanics*, vol. 585, pp. 73–92, 2007.

[55] G. A. Bird, *Molecular Gas Dynamics and the Direct Simulation of Gas Flows*. Clarendon Press, 1994.

[56] C. Guo, Zhaoli and Shu, *Lattice Boltzmann Method and its Applications in Engineering*. World Scientific, 2013.

[57] S. Chapman, T. G. Cowling, and M. T. Társulat, *The Mathematical Theory of Non-uniform Gases*. Cambridge University Press, 1953.

[58] T. Kajishima and K. Taira, *Computational Fluid Dynamics: Incompressible Turbulent Flows*. Springer International Publishing, 2017.

[59] R. B. Bird, W. E. Stewart, and E. N. Lightfoot, *Transport Phenomena*. John Wiley & Sons, 2002.

[60] F. Sharipov, *Rarefied Gas Dynamics: Fundamentals for Research and Practice*. John Wiley & Sons, 2016.

[61] T. Krüger, F. Varnik, and D. Raabe, "Efficient and accurate simulations of deformable particles immersed in a fluid using a combined immersed boundary lattice Boltzmann finite element method," *Computers & Mathematics with Applications*, vol. 61, no. 12, pp. 3485–3505, 2011.

[62] C. Cercignani, *The Boltzmann Equation and Its Applications*, vol. 67. Springer, 1988.

[63] C. Truesdell and R. G. Muncaster, *Fundamentals of Maxwell's Kinetic Theory of a Simple Monatomic Gas: Treated as a Branch of Rational Mechanics*. Academic Press, 1980.

[64] P. A. Cundall and O. D. L. Strack, "A discrete numerical model for granular assemblies," *Géotechnique*, vol. 29, no. 1, pp. 47–65, 1979.

[65] H. R. Norouzi, R. Zarghami, R. Sotudeh-Gharebagh, and N. Mostoufi, *Coupled CFD-DEM Modeling: Formulation, Implementation and Application to Multiphase Flows*. John Wiley & Sons, 2016.

[66] H. Herrmann and S. Luding, "Modeling granular media on the computer," *Continuum Mechanics and Thermodynamics*, vol. 10, no. 4, pp. 189–231, 1998.

[67] S. Luding, "Cohesive, frictional powders: contact models for tension," *Granular matter*, vol. 10, no. 4, pp. 235–246, 2008.

[68] S. Luding, "Introduction to discrete element methods," *European Journal of Environmental and Civil Engineering*, vol. 12, no. 7-8, pp. 785–826, 2008.

[69] S. Haeri, Y. Wang, O. Ghita, and J. Sun, "Discrete element simulation and experimental study of powder spreading process in additive manufacturing," *Powder Technology*, vol. 306, pp. 45–54, 2017.

[70] A. Di Renzo and F. P. Di Maio, "Comparison of contact-force models for the simulation of collisions in DEM-based granular flow codes," *Chemical Engineering Science*, vol. 59, no. 3, pp. 525–541, 2004.

[71] C. H. K. Williamson and R. Govardhan, "A brief review of recent results in vortex-induced vibrations," *Journal of Wind Engineering and Industrial Aerodynamics*, vol. 96, pp. 713–735, 2008.

[72] R. D. Gabbai and H. Benaroya, "An overview of modeling and experiments of vortex-induced vibration of circular cylinders," *Journal of Sound and Vibration*, vol. 282, pp. 575–616, 2005.

[73] H. G. Sung, H. Baek, S. Hong, and J. S. Choi, "Numerical study of vortex-induced vibration of pivoted cylinders," *Ocean Engineering*, vol. 93, pp. 98–106, 2015.

[74] S. Mittal, "The critical mass phenomenon in vortex-induced vibration at low Re," *Journal of Fluid Mechanics*, vol. 820, pp. 159–186, 2017.

[75] H. Dütsch, F. Durst, S. Becker, and H. Lienhart, "Low-Reynolds-number flow around an oscillating circular cylinder at low keulegan–carpenter numbers," *Journal of Fluid Mechanics*, vol. 360, pp. 249–271, 1998.

[76] C. Williamson and A. Roshko, "Vortex formation in the wake of an oscillating cylinder," *Journal of Fluids and Structures*, vol. 2, no. 4, pp. 355–381, 1988.

[77] A. Khalak and C. H. Williamson, "Motions, forces and mode transitions in vortex-induced vibrations at low mass-damping," *Journal of fluids and Structures*, vol. 13, no. 7-8, pp. 813–851, 1999.

[78] R. Govardhan and C. H. K. Williamson, "Modes of vortex formation and frequency response of a freely vibrating cylinder," *Journal of Fluid Mechanics*, vol. 420, pp. 85–130, 2000.

[79] T. L. Morse and C. H. Williamson, "The effect of Reynolds number on the critical mass phenomenon in vortex-induced vibration," *Physics of Fluids*, vol. 21, pp. 1–8, 2009.

[80] R. Govardhan and C. Williamson, "Resonance forever: existence of a critical mass and an infinite regime of resonance in vortex-induced vibration," *Journal of Fluid Mechanics*, vol. 473, pp. 147–166, 2002.

[81] S. P. Singh and S. Mittal, "Vortex-induced oscillations at low Reynolds numbers: Hysteresis and vortex-shedding modes," *Journal of Fluids and Structures*, vol. 20, pp. 1085–1104, 2005.

[82] S. Mittal and S. Singh, "Vortex-induced vibrations at subcritical Re," *Journal of Fluid Mechanics*, vol. 534, pp. 185–194, 2005.

[83] T. K. Prasanth and S. Mittal, "Vortex-induced vibrations of a circular cylinder at low Reynolds numbers," *Journal of Fluid Mechanics*, vol. 594, p. 463–491, 2008.

[84] D. Shiels, A. Leonard, and A. Roshko, "Flow-induced vibration of a circular cylinder at limiting structural parameters," *Journal of Fluids and Structures*, vol. 15, no. 1, pp. 3–21, 2001.

[85] K. Ryan, M. C. Thompson, and K. Hourigan, "Variation in the critical mass ratio of a freely oscillating cylinder as a function of Reynolds number," *Physics of Fluids*, vol. 17, pp. 1–4, 2005.

[86] M. P. Allen *et al.*, "Introduction to molecular dynamics simulation," *Computational soft matter: from synthetic polymers to proteins*, vol. 23, no. 1, pp. 1–28, 2004.

[87] T. Pöschel and T. Schwager, *Computational Granular Dynamics: Models and Algorithms*. Springer, 2005.

[88] M. P. Allen and D. J. Tildesley, *Computer Simulation of Liquids*. Oxford University Press, 2017.

[89] P. Hoogerbrugge and J. Koelman, "Simulating microscopic hydrodynamic phenomena with dissipative particle dynamics," *Europhysics Letters*, vol. 19, no. 3, p. 155, 1992.

[90] J. E. Broadwell, "Study of rarefied shear flow by the discrete velocity method," *Journal of Fluid Mechanics*, vol. 19, no. 3, pp. 401–414, 1964.

[91] K. Xu and J.-C. Huang, "A unified gas-kinetic scheme for continuum and rarefied flows," *Journal of Computational Physics*, vol. 229, no. 20, pp. 7747–7764, 2010.

[92] Z. Guo, K. Xu, and R. Wang, "Discrete unified gas kinetic scheme for all Knudsen number flows: Low-speed isothermal case," *Physical Review E*, vol. 88, no. 3, p. 033305, 2013.

[93] S. Succi, *The Lattice Boltzmann Equation for Fluid Dynamics and Beyond*. Oxford University Press, 2001.

[94] D. H. Rothman and S. Zaleski, *Lattice-Gas Cellular Automata: Simple Models of Complex Hydrodynamics*. Cambridge University Press, 1997.

[95] D. A. Wolf-Gladrow, *Lattice-Gas Cellular Automata and Lattice Boltzmann Models: An Introduction*. Springer, 2004.

[96] H. K. Versteeg and W. Malalasekera, *An Introduction to Computational Fluid Dynamics: The Finite Volume Method*. Pearson Education, 2007.

[97] J. Donea and A. Huerta, *Finite Element Methods for Flow Problems*. John Wiley & Sons, 2003.

[98] D. Anderson, J. C. Tannehill, and R. H. Pletcher, *Computational Fluid Mechanics and Heat Transfer*. American Mathematical Society, 1986.

[99] T. Chung, *Computational Fluid Dynamics*. Cambridge University Press, 2002.

[100] A. T. Patera, "A spectral element method for fluid dynamics: laminar flow in a channel expansion," *Journal of computational Physics*, vol. 54, no. 3, pp. 468–488, 1984.

[101] J. Yang, S. Preidikman, and E. Balaras, "A strongly coupled, embedded-boundary method for fluid–structure interactions of elastically mounted rigid bodies," *Journal of Fluids and Structures*, vol. 24, pp. 167–182, 2008.

[102] W. Kim, I. Lee, and H. Choi, "A weak-coupling immersed boundary method for fluid–structure interaction with low density ratio of solid to fluid," *Journal of Computational Physics*, vol. 359, pp. 296–311, 2018.

[103] B. Hübner, E. Walhorn, and D. Dinkler, "A monolithic approach to fluid–structure interaction using space–time finite elements," *Computer methods in applied mechanics and engineering*, vol. 193, no. 23-26, pp. 2087–2104, 2004.

[104] J. Degroote, K.-J. Bathe, and J. Vierendeels, "Performance of a new partitioned procedure versus a monolithic procedure in fluid–structure interaction," *Computers & Structures*, vol. 87, no. 11, pp. 793–801, 2009.

[105] P. Causin, J. F. Gerbeau, and F. Nobile, "Added-mass effect in the design of partitioned algorithms for fluid–structure problems," *Computer Methods in Applied Mechanics and Engineering*, vol. 194, pp. 4506–4527, 2005.

[106] C. Förster, W. A. Wall, and E. Ramm, "Artificial added mass instabilities in sequential staggered coupling of nonlinear structures and incompressible viscous flows," *Computer Methods in Applied Mechanics and Engineering*, vol. 196, no. 7, pp. 1278–1293, 2007.

[107] M. Uhlmann, "An immersed boundary method with direct forcing for the simulation of particulate flows," *Journal of Computational Physics*, vol. 209, no. 2, pp. 448–476, 2005.

[108] W. P. Breugem, "A second-order accurate immersed boundary method for fully resolved simulations of particle-laden flows," *Journal of Computational Physics*, vol. 231, no. 13, pp. 4469–4498, 2012.

[109] J. Yang and F. Stern, "A simple and efficient direct forcing immersed boundary framework for fluid-structure interactions," *Journal of Computational Physics*, vol. 231, pp. 5029–5061, 2012.

[110] U. Lacis, K. Taira, and S. Bagheri, "A stable fluid–structure-interaction solver for low-density rigid bodies using the immersed boundary projection method," *Journal of Computational Physics*, vol. 305, pp. 300–318, 2016.

[111] T. Kempe and J. Fröhlich, "An improved immersed boundary method with direct forcing for the simulation of particle laden flows," *Journal of Computational Physics*, vol. 231, pp. 3663–3684, 2012.

[112] C. Wang and J. D. Eldredge, "Strongly coupled dynamics of fluids and rigid-body systems with the immersed boundary projection method," *Journal of Computational Physics*, vol. 295, pp. 87–113, 2015.

[113] A. Goza and T. Colonius, "A strongly-coupled immersed-boundary formulation for thin elastic structures," *Journal of Computational Physics*, vol. 336, pp. 401–411, 2017.

[114] H. G. Matthies, R. Niekamp, and J. Steindorf, "Algorithms for strong coupling procedures," *Computer Methods in Applied Mechanics and Engineering*, vol. 195, no. 17, pp. 2028–2049, 2006.

[115] G. Tryggvason, R. Scardovelli, and S. Zaleski, *Direct Numerical Simulations of Gas–Liquid Multiphase Flows*. Cambridge University Press, 2011.

[116] A. Prosperetti and G. Tryggvason, *Computational Methods for Multiphase Flow*. Cambridge University Press, 2007.

[117] C. W. Hirt and B. D. Nichols, "Volume of fluid VOF method for the dynamics of free boundaries," *Journal of Computational Physics*, vol. 39, no. 1, pp. 201–225, 1981.

[118] S. Osher and J. A. Sethian, "Fronts propagating with curvature-dependent speed: Algorithms based on Hamilton-Jacobi formulations," *Journal of Computational Physics*, vol. 79, no. 1, pp. 12–49, 1988.

[119] M. Sussman, P. Smereka, and S. Osher, "A level set approach for computing solutions to incompressible two-phase flow," *Journal of Computational Physics*, vol. 114, no. 1, pp. 146–159, 1994.

[120] G. Tryggvason, B. Bunner, A. Esmaeeli, D. Juric, N. Al-Rawahi, W. Tauber, J. Han, S. Nas, and Y.-J. Jan, "A front-tracking method for the computations of multiphase flow," *Journal of Computational Physics*, vol. 169, no. 2, pp. 708–759, 2001.

[121] J. Hardy, Y. Pomeau, and O. de Pazzis, "Time evolution of a two-dimensional model system. I. Invariant states and time correlation functions," *Journal of Mathematical Physics*, vol. 14, no. 12, pp. 1746–1759, 1973.

[122] G. R. McNamara and G. Zanetti, "Use of the Boltzmann equation to simulate lattice-gas automata," *Physical Review Letters*, vol. 61, pp. 2332–2335, 1988.

[123] X. He and L.-S. Luo, "Theory of the lattice Boltzmann method: From the Boltzmann equation to the lattice Boltzmann equation," *Physical Review E*, vol. 56, pp. 6811–6817, 1997.

[124] Y.-H. Qian, D. d'Humières, and P. Lallemand, "Lattice BGK models for Navier-Stokes equation," *Europhysics Letters*, vol. 17, no. 6, p. 479, 1992.

[125] L.-S. Luo, W. Liao, X. Chen, Y. Peng, W. Zhang, *et al.*, "Numerics of the lattice Boltzmann method: Effects of collision models on the lattice Boltzmann simulations," *Physical Review E*, vol. 83, no. 5, p. 056710, 2011.

[126] C. Pan, L.-S. Luo, and C. T. Miller, "An evaluation of lattice Boltzmann schemes for porous medium flow simulation," *Computers & Fluids*, vol. 35, no. 8-9, pp. 898–909, 2006.

[127] P. Bhatnagar, E. Gross, and M. Krook, "A model for collision processes in gases. I. Small amplitude processes in charged and neutral one-component systems," *Physical Review*, vol. 94, no. 3, pp. 511–525, 1954.

[128] X. He, Q. Zou, L.-S. Luo, and M. Dembo, "Analytic solutions of simple flows and analysis of nonslip boundary conditions for the lattice Boltzmann BGK model," *Journal of Statistical Physics*, vol. 87, no. 1, pp. 115–136, 1997.

[129] D. d'Humières, I. Ginzburg, M. Krafczyk, P. Lallemand, and L.-S. Luo, "Multiple–relaxation–time lattice Boltzmann models in three dimensions," *Philosophical Transactions of the Royal Society of London. Series A: Mathematical, Physical and Engineering Sciences*, vol. 360, no. 1792, pp. 437–451, 2002.

[130] D. d'Humières, *Generalized Lattice-Boltzmann Equations*. American Institute of Aeronautics and Astronautics, 1992.

[131] P. Lallemand and L.-S. Luo, "Theory of the lattice Boltzmann method: Dispersion, dissipation, isotropy, Galilean invariance, and stability," *Physical review E*, vol. 61, no. 6, p. 6546, 2000.

[132] I. Ginzburg, F. Verhaeghe, and D. d'Humières, "Two-relaxation-time lattice Boltzmann scheme: About parametrization, velocity, pressure and mixed boundary conditions," *Communications in Computational Physics*, vol. 3, no. 2, pp. 427–478, 2008.

[133] D. d'Humières and I. Ginzburg, "Viscosity independent numerical errors for lattice Boltzmann models: From recurrence equations to "magic" collision numbers," *Computers & Mathematics with Applications*, vol. 58, no. 5, pp. 823–840, 2009.

[134] M. Geier, A. Greiner, and J. G. Korvink, "Cascaded digital lattice Boltzmann automata for high Reynolds number flow," *Physical Review E*, vol. 73, no. 6, p. 066705, 2006.

[135] A. De Rosis and E. Lévêque, "Central-moment lattice Boltzmann schemes with fixed and moving immersed boundaries," *Computers & Mathematics with Applications*, vol. 72, no. 6, pp. 1616–1628, 2016.

[136] D. Lycett-Brown and K. H. Luo, "Multiphase cascaded lattice Boltzmann method," *Computers & Mathematics with Applications*, vol. 67, no. 2, pp. 350–362, 2014.

[137] L. Fei and K. H. Luo, "Consistent forcing scheme in the cascaded lattice Boltzmann method," *Physical Review E*, vol. 96, p. 053307, 2017.

[138] Y. Ning, K. N. Premnath, and D. V. Patil, "Numerical study of the properties of the central moment lattice Boltzmann method," *International Journal for Numerical Methods in Fluids*, vol. 82, no. 2, pp. 59–90, 2016.

[139] K. N. Premnath and S. Banerjee, "Incorporating forcing terms in cascaded lattice Boltzmann approach by method of central moments," *Physical Review E*, vol. 80, no. 3, p. 036702, 2009.

[140] C. Coreixas, B. Chopard, and J. Latt, "Comprehensive comparison of collision models in the lattice Boltzmann framework: Theoretical investigations," *Physical Review E*, vol. 100, no. 3, p. 33305, 2019.

[141] R. S. Maier, R. S. Bernard, and D. W. Grunau, "Boundary conditions for the lattice Boltzmann method," *Physics of Fluids*, vol. 8, no. 7, pp. 1788–1801, 1996.

[142] D. P. Ziegler, "Boundary conditions for lattice Boltzmann simulations," *Journal of Statistical Physics*, vol. 71, no. 5, pp. 1171–1177, 1993.

[143] A. J. Ladd, "Numerical simulations of particulate suspensions via a discretized Boltzmann equation.Part 1. Theoretical foundation," *Journal of Fluid Mechanics*, vol. 271, pp. 285–309, 1994.

[144] J. Meng, X.-J. Gu, and D. R. Emerson, "Analysis of non-physical slip velocity in lattice Boltzmann simulations using the bounce-back scheme," *Journal of Computational Science*, vol. 28, pp. 476–482, 2018.

[145] Q. Zou and X. He, "On pressure and velocity boundary conditions for the lattice Boltzmann BGK model," *Physics of Fluids*, vol. 9, no. 6, pp. 1591–1598, 1997.

[146] Z. Guo, C. Zheng, and B. Shi, "Discrete lattice effects on the forcing term in the lattice Boltzmann method," *Physical Review E*, vol. 65, no. 4, p. 046308, 2002.

[147] L. Fei, K. H. Luo, and Q. Li, "Three-dimensional cascaded lattice Boltzmann method: Improved implementation and consistent forcing scheme," *Physical Review E*, vol. 97, p. 053309, 2018.

[148] C. Peng, O. M. Ayala, and L. P. Wang, "A comparative study of immersed boundary method and interpolated bounce-back scheme for no-slip boundary treatment in the lattice Boltzmann method: Part I, laminar flows," *Computers & Fluids*, vol. 192, p. 104233, 2019.

[149] M. Bouzidi, M. Firdaouss, and P. Lallemand, "Momentum transfer of a Boltzmannlattice fluid with boundaries," *Physics of Fluids*, vol. 13, no. 11, pp. 3452–3459, 2001.

[150] D. Noble and J. Torczynski, "A lattice-Boltzmann method for partially saturated computational cells," *International Journal of Modern Physics C*, vol. 9, no. 08, pp. 1189–1201, 1998.

[151] O. E. Strack and B. K. Cook, "Three-dimensional immersed boundary conditions for moving solids in the lattice-Boltzmann method," *International Journal for Numerical Methods in Fluids*, vol. 55, no. 2, pp. 103–125, 2007.

[152] C. Tsigginos, J. Meng, X. J. Gu, and D. R. Emerson, "Lattice Boltzmann modeling of fluid-particle interaction based on a two-phase mixture representation," *Physical Review E*, vol. 100, no. 6, p. 063311, 2019.

[153] C. S. Peskin, "Flow patterns around heart valves: A numerical method," *Journal of Computational Physics*, vol. 10, no. 2, pp. 252–271, 1972.

[154] C. S. Peskin, "The immersed boundary method," *Acta Numerica*, vol. 11, pp. 479–517, 2002.

[155] C. S. Peskin, "Numerical analysis of blood flow in the heart," *Journal of Computational Physics*, vol. 25, no. 3, pp. 220–252, 1977.

[156] S. K. Kang and Y. A. Hassan, "A comparative study of direct-forcing immersed boundary-lattice Boltzmann methods for stationary complex boundaries," *International Journal for Numerical Methods in Fluids*, vol. 66, no. 9, pp. 1132–1158, 2011.

[157] K. Suzuki and T. Inamuro, "Effect of internal mass in the simulation of a moving body by the immersed boundary method," *Computers & Fluids*, vol. 49, no. 1, pp. 173–187, 2011.

[158] X. Wang and L. T. Zhang, "Interpolation functions in the immersed boundary and finite element methods," *Computational Mechanics*, vol. 45, no. 4, pp. 321–334, 2010.

[159] Y. Zhang, Y. Zhang, G. Pan, and S. Haeri, "Numerical study of the particle sedimentation in a viscous fluid using a coupled DEM-IB-CLBM approach," *Journal of Computational Physics*, vol. 368, pp. 1–20, 2018.

[160] M.-C. Lai and C. S. Peskin, "An immersed boundary method with formal second-order accuracy and reduced numerical viscosity," *Journal of Computational Physics*, vol. 160, no. 2, pp. 705–719, 2000.

[161] Z. G. Feng and E. E. Michaelides, "Robust treatment of no-slip boundary condition and velocity updating for the lattice-Boltzmann simulation of particulate flows," *Computers & Fluids*, vol. 38, no. 2, pp. 370–381, 2009.

[162] E. Fadlun, R. Verzicco, P. Orlandi, and J. Mohd-Yusof, "Combined immersed-boundary finite-difference methods for three-dimensional complex flow simulations," *Journal of Computational Physics*, vol. 161, no. 1, pp. 35–60, 2000.

[163] Z. Wang, J. Fan, and K. Luo, "Combined multi-direct forcing and immersed boundary method for simulating flows with moving particles," *International Journal of Multiphase Flow*, vol. 34, no. 3, pp. 283–302, 2008.

[164] J. Wu and C. Shu, "Implicit velocity correction-based immersed boundary-lattice Boltzmann method and its applications," *Journal of Computational Physics*, vol. 228, no. 6, pp. 1963–1979, 2009.

[165] A. ten Cate, C. H. Nieuwstad, J. J. Derksen, and H. E. V. den Akker, "Particle imaging velocimetry experiments and lattice-Botlzmann simulations on a single sphere settling under gravity," *Physics of Fluids*, vol. 14, no. 11, pp. 4012–4025, 2002.

[166] S. Tschisgale, T. Kempe, and J. Fröhlich, "A general implicit direct forcing immersed boundary method for rigid particles," *Computers & Fluids*, vol. 170, pp. 285–298, 2018.

[167] Y. Zhang, S. Haeri, G. Pan, and Y. Zhang, "Strongly coupled peridynamic and lattice Boltzmann models using immersed boundary method for flow-induced structural deformation and fracture," *Journal of Computational Physics*, vol. 435, p. 110267, 2021.

[168] Y. Tsuji, T. Kawaguchi, and T. Tanaka, "Discrete particle simulation of two-dimensional fluidized bed," *Powder technology*, vol. 77, no. 1, pp. 79–87, 1993.

[169] K. Kafui, C. Thornton, and M. Adams, "Discrete particle-continuum fluid modelling of gas–solid fluidised beds," *Chemical Engineering Science*, vol. 57, no. 13, pp. 2395–2410, 2002.

[170] U. Ghia, K. N. Ghia, and C. Shin, "High-Re solutions for incompressible flow using the Navier-Stokes equations and a multigrid method," *Journal of Computational Physics*, vol. 48, no. 3, pp. 387–411, 1982.

[171] S. Hou, Q. Zou, S. Chen, G. Doolen, and A. C. Cogley, "Simulation of cavity flow by the lattice Boltzmann method," *Journal of Computational Physics*, vol. 118, no. 2, pp. 329–347, 1995.

[172] C. Li and J. Maa, "Multi-relaxation-time lattice Boltzmann simulations of lid driven flows using graphics processing unit," *Applied Mathematics and Mechanics*, vol. 38, no. 5, pp. 707–722, 2017.

[173] E. Aslan, I. Taymaz, and A. Benim, "Investigation of the lattice Boltzmann SRT and MRT stability for lid driven cavity flow," *International Journal of Materials, Mechanics and Manufacturing*, vol. 2, no. 4, pp. 317–324, 2014.

[174] D. R. Noble, S. Chen, J. G. Georgiadis, and R. O. Buckius, "A consistent hydrodynamic boundary condition for the lattice Boltzmann method," *Physics of Fluids*, vol. 7, no. 1, pp. 203–209, 1995.

[175] I. Ginzburg and D. d'Humières, "Multireflection boundary conditions for lattice Boltzmann models," *Physical Review E*, vol. 68, no. 6, p. 066614, 2003.

[176] I. Ginzburg, D. d'Humières, and A. Kuzmin, "Optimal stability of advection-diffusion lattice Boltzmann models with two relaxation times for positive/negative equilibrium," *Journal of Statistical Physics*, vol. 139, no. 6, pp. 1090–1143, 2010.

[177] A. Kuzmin, A. Mohamad, and S. Succi, "Multi-relaxation time lattice Boltzmann model for multiphase flows," *International Journal of Modern Physics C*, vol. 19, no. 06, pp. 875–902, 2008.

[178] M. A. Seaton, R. L. Anderson, S. Metz, and W. Smith, "DL_MESO: highly scalable mesoscale simulations," *Molecular Simulation*, vol. 39, no. 10, pp. 796–821, 2013.

[179] J.-S. Wu and Y.-L. Shao, "Simulation of lid-driven cavity flows by parallel lattice Boltzmann method using multi-relaxation-time scheme," *International Journal for Numerical Methods in Fluids*, vol. 46, no. 9, pp. 921–937, 2004.

[180] A. Abbati, Y. Zhang, W. Dempster, and Y. Zhang, "The immersed boundary method for confined flows: Numerical diffusion and simulation accuracy of a boundary retraction scheme," *Computers & Fluids*, vol. 249, p. 105690, 2022.

[181] Q. Zhou and L. S. Fan, "A second-order accurate immersed boundary-lattice Boltzmann method for particle-laden flows," *Journal of Computational Physics*, vol. 268, pp. 269–301, 2014.

[182] C. Peng and L. P. Wang, "Force-amplified, single-sided diffused-interface immersed boundary kernel for correct local velocity gradient computation and accurate no-slip boundary enforcement," *Physical Review E*, vol. 101, no. 5, p. 053305, 2020.

[183] Z. Yu and X. Shao, "A direct-forcing fictitious domain method for particulate flows," *Journal of Computational Physics*, vol. 227, no. 1, pp. 292–314, 2007.

[184] T. T. Bringley and C. S. , "Validation of a simple method for representing spheres and slender bodies in an immersed boundary method for Stokes flow on an unbounded domain," *Journal of Computational Physics*, vol. 227, no. 11, pp. 5397–5425, 2008.

[185] J. M. Stockie, "Modelling and simulation of porous immersed boundaries," *Computers & Structures*, vol. 87, no. 11-12, pp. 701–709, 2009.

[186] M. Maxey, "Simulation methods for particulate flows and concentrated suspensions," *Annual Review of Fluid Mechanics*, vol. 49, pp. 171–193, 2017.

[187] L. Chen, Y. Yu, and G. Hou, "Sharp-interface immersed boundary lattice Boltzmann method with reduced spurious-pressure oscillations for moving boundaries," *Physical Review E*, vol. 87, no. 5, p. 053306, 2013.

[188] D. J. Tritton, "Experiments on the flow past a circular cylinder at low Reynolds numbers," *Journal of Fluid Mechanics*, vol. 6, no. 4, pp. 547–567, 1959.

[189] A. M. Ardekani and R. H. Rangel, "Numerical investigation of particle-particle and particle-wall collisions in a viscous fluid," *Journal of Fluid Mechanics*, vol. 596, pp. 437–466, 2008.

[190] R. Cox, "The motion of suspended particles almost in contact," *International Journal of Multiphase Flow*, vol. 1, no. 2, pp. 343–371, 1974.

[191] A. J. C. Ladd and R. Verberg, "Lattice-Boltzmann simulations of particle-fluid suspensions," *Journal of Statistical Physics*, vol. 104, pp. 1191–1251, 2001.

[192] N.-Q. Nguyen and A. J. C. Ladd, "Lubrication corrections for lattice-Boltzmann simulations of particle suspensions," *Phys. Rev. E*, vol. 66, p. 046708, 2002.

[193] E.-J. Ding and C. K. Aidun, "Extension of the lattice-Boltzmann method for direct simulation of suspended particles near contact," *Journal of Statistical Physics*, vol. 112, pp. 685–708, 2003.

[194] A. B. Richou, A. Ambari, and J. K. Naciri, "Drag force on a circular cylinder midway between two parallel plates at very low Reynolds numbers. Part 1: Poiseuille flow (numerical)," *Chemical Engineering Science*, vol. 59, no. 15, pp. 3215–3222, 2004.

[195] A. S. Dvinsky and A. S. Popel, "Motion of a rigid cylinder between parallel plates in Stokes flow. Part 2: Poiseuille and Couette flow," *Computers & Fluids*, vol. 15, no. 4, pp. 405–419, 1987.

[196] B. Semin, J. P. Hullin, and H. Auradou, "Influence of flow confinement on the drag force on a static cylinder," *Physics of Fluids*, vol. 21, no. 10, p. 103604, 2009.

[197] Y. Han and P. A. Cundall, "Resolution sensitivity of momentum-exchange and immersed boundary methods for solid-fluid interaction in the lattice Boltzmann method," *International Journal for Numerical Methods in Fluids*, vol. 67, no. 3, pp. 314–327, 2011.

[198] A. S. Dvinsky and A. S. Popel, "Motion of a rigid cylinder between parallel plates in Stokes flow. Part 1: Motion in a quiescent fluid and sedimentation," *Computers & Fluids*, vol. 15, no. 4, pp. 391–404, 1987.

[199] G. Pianet and E. Arquis, "Simulation of particles in fluid: a two-dimensional benchmark for a cylinder settling in a wall-bounded box," *European Journal of Mechanics*, vol. 27, no. 3, pp. 309–321, 2008.

[200] S. Champmartin and A. Ambari, "Kinematics of a symmetrically confined cylindrical particle in a "Stokes-type" regime," *Physics of Fluids*, vol. 19, no. 7, p. 073303, 2007.

[201] A. R. Curtis and G. R. Marr, "The viscous drag on cylinders falling symmetrically between parallel walls," *Journal of Physics D: Applied Physics*, vol. 11, no. 8, pp. 1173–1178, 1978.

[202] K. O. Jayaweera and B. J. Mason, "The behaviour of freely falling cylinders and cones in a viscous fluid," *Journal of Fluid Mechanics*, vol. 22, no. 4, pp. 709–720, 1965.

[203] S. Ghosh and J. M. Stockie, "Numerical simulations of particle sedimentation using the immersed boundary method," *Communications in Computational Physics*, vol. 18, no. 2, pp. 380–416, 2015.

[204] A. Ben Richou, A. Ambari, M. Lebey, and J. K. Naciri, "Drag force on a circular cylinder midway between two parallel plates at Re$\ll$1. Part 2: Moving uniformly (numerical and experimental)," *Chemical Engineering Science*, vol. 60, no. 10, pp. 2535–2543, 2005.

[205] N. Bampalas and J. M. Graham, "Flow-induced forces arising during the impact of two circular cylinders," *Journal of Fluid Mechanics*, vol. 616, pp. 205–234, 2008.

[206] A. F. Fortes, D. D. Joseph, and T. S. Lundgren, "Nonlinear mechanics of fluidization of beds of spherical particles," *Journal of Fluid Mechanics*, vol. 177, pp. 467–483, 1987.

[207] C. K. Aidun and E. J. Ding, "Dynamics of particle sedimentation in a vertical channel: Period-doubling bifurcation and chaotic state," *Physics of Fluids*, vol. 15, no. 6, pp. 1612–1621, 2003.

[208] L. Wang, Z. L. Guo, and J. C. Mi, "Drafting, kissing and tumbling process of two particles with different sizes," *Computers & Fluids*, vol. 96, pp. 20–34, 2014.

[209] P. Zhang, S. A. Galindo-Torres, H. Tang, G. Jin, A. Scheuermann, and L. Li, "An efficient discrete element lattice Boltzmann model for simulation of particle-fluid, particle-particle interactions," *Computers & Fluids*, vol. 147, pp. 63–71, 2017.

[210] H. Zhang, Y. Tan, S. Shu, X. Niu, F. X. Trias, D. Yang, H. Li, and Y. Sheng, "Numerical investigation on the role of discrete element method in combined LBM-IBM-DEM modeling," *Computers & Fluids*, vol. 94, pp. 37–48, 2014.

[211] D. Qi, "Lattice-Boltzmann simulations of particles in non-zero-Reynolds-number flows," *Journal of Fluid Mechanics*, vol. 385, pp. 41–62, 1999.

[212] D. Wan and S. Turek, "An efficient multigrid-FEM method for the simulation of solid–liquid two phase flows," *Journal of Computational and Applied Mathematics*, vol. 203, pp. 561–580, 2007.

[213] D. Wan and S. Turek, "Direct numerical simulation of particulate flow via multigrid FEM techniques and the fictitious boundary method," *International Journal for Numerical Methods in Fluids*, vol. 51, pp. 531–566, 2006.

[214] R. Glowinski, T. W. Pan, T. I. Hesla, D. D. Joseph, and J. Périaux, "A fictitious domain approach to the direct numerical simulation of incompressible viscous flow past moving rigid bodies: Application to particulate flow," *Journal of Computational Physics*, vol. 169, no. 2, pp. 363–426, 2001.

[215] Y. Di, L. Zhao, and J. Mao, "A resolved CFD-DEM method based on the IBM for sedimentation of dense fluid-particle flows," *Computers & Fluids*, vol. 226, p. 104968, 2021.

[216] S. Tao, Q. He, J. Chen, B. Chen, G. Yang, and Z. Wu, "A non-iterative immersed boundary-lattice Boltzmann method with boundary condition enforced for fluid–solid flows," *Applied Mathematical Modelling*, vol. 76, pp. 362–379, 2019.

[217] B. Wen, H. Li, C. Zhang, and H. Fang, "Lattice-type-dependent momentum-exchange method for moving boundaries," *Physical Review E*, vol. 85, p. 16704, 2012.

[218] C. K. Aidun and Y. Lu, "Lattice Boltzmann simulation of solid particles suspended in fluid," *Journal of Statistical Physics*, vol. 81, no. 1, pp. 49–61, 1995.

[219] H. Li, X. Lu, H. Fang, and Y. Qian, "Force evaluations in lattice Boltzmann simulations with moving boundaries in two dimensions," *Physical Review E*, vol. 70, p. 9, 2004.

[220] J. Feng, H. H. Hu, and D. D. Joseph, "Direct simulation of initial value problems for the motion of solid bodies in a Newtonian fluid. Part 1. Sedimentation," *Journal of Fluid Mechanics*, vol. 261, pp. 95–134, 1994.

[221] X. Yang, X. Zhang, Z. Li, and G. W. He, "A smoothing technique for discrete delta functions with application to immersed boundary method in moving boundary simulations," *Journal of Computational Physics*, vol. 228, pp. 7821–7836, 2009.

[222] M. J. Chern, Y. H. Kuan, G. Nugroho, G. T. Lu, and T. L. Horng, "Direct-forcing immersed boundary modeling of vortex-induced vibration of a circular cylinder," *Journal of Wind Engineering and Industrial Aerodynamics*, vol. 134, pp. 109–121, 2014.

[223] M. D. Griffith and J. S. Leontini, "Sharp interface immersed boundary methods and their application to vortex-induced vibration of a cylinder," *Journal of Fluids and Structures*, vol. 72, pp. 38–58, 2017.

[224] M. Braza, P. Chassaing, and H. H. Minh, "Numerical study and physical analysis of the pressure and velocity fields in the near wake of a circular cylinder," *Journal of Fluid Mechanics*, vol. 165, pp. 79–130, 1986.

[225] S. Mittal and S. Singh, "Vortex-induced vibrations at subcritical Re," *Journal of Fluid Mechanics*, vol. 534, pp. 185–194, 2005.

[226] C. Liu, X. Zheng, and C. H. Sung, "Preconditioned multigrid methods for unsteady incompressible flows," *Journal of Computational Physics*, vol. 139, pp. 35–57, 1998.

[227] J. Kim, D. Kim, and H. Choi, "An immersed-boundary finite-volume method for simulations of flow in complex geometries," *Journal of Computational Physics*, vol. 171, no. 1, pp. 132–150, 2001.

[228] D. Le, B. Khoo, and K. Lim, "An implicit-forcing immersed boundary method for simulating viscous flows in irregular domains," *Computer Methods in Applied Mechanics and Engineering*, vol. 197, no. 25, pp. 2119–2130, 2008.

[229] C. H. Williamson, "Oblique and parallel modes of vortex shedding in the wake of a circular cylinder at low Reynolds numbers," *Journal of Fluid Mechanics*, vol. 206, pp. 579–627, 1989.

[230] A. Roshko, "On the wake and drag of bluff bodies," *Journal of the aeronautical sciences*, vol. 22, no. 2, pp. 124–132, 1955.

[231] B. M. Sumer and J. Fredsøe, *Hydrodynamics around Cylindrical Structures*. World Scientific, 2006.

[232] G. K. Batchelor, *An Introduction to Fluid Dynamics*. Cambridge University Press, 2000.

[233] A. G. Piersol, *Harris' Shock and Vibration Handbook*. McGraw-Hill, 2009.

[234] S. Karimnejad, A. Amiri Delouei, M. Nazari, M. Shahmardan, and A. Mohamad, "Sedimentation of elliptical particles using immersed boundary-lattice Boltzmann method: A complementary repulsive force model," *Journal of Molecular Liquids*, vol. 262, pp. 180–193, 2018.

[235] Z. Xia, K. W. Connington, S. Rapaka, P. Yue, J. J. Feng, and S. Chen, "Flow patterns in the sedimentation of an elliptical particle," *Journal of Fluid Mechanics*, vol. 625, pp. 249–272, 2009.

[236] S. Karimnejad, A. Amiri Delouei, M. Nazari, M. M. Shahmardan, M. M. Rashidi, and S. Wongwises, "Immersed boundary-thermal lattice Boltzmann method for the moving simulation of non-isothermal elliptical particles," *Journal of Thermal Analysis and Calorimetry*, vol. 138, no. 6, pp. 4003–4017, 2019.

[237] R. Bourguet and D. Lo Jacono, "Flow-induced vibrations of a rotating cylinder," *Journal of Fluid Mechanics*, vol. 740, pp. 342–380, 2014.

[238] M. M. Rajamuni, M. C. Thompson, and K. Hourigan, "Vortex-induced vibration of a transversely rotating sphere," *Journal of Fluid Mechanics*, vol. 847, pp. 786–820, 2018.

[239] P. Ern, F. Risso, D. Fabre, and J. Magnaudet, "Wake-induced oscillatory paths of bodies freely rising or falling in fluids," *Annual Review of Fluid Mechanics*, vol. 44, pp. 97–121, 2012.

[240] S. Lomholt, B. Stenum, and M. Maxey, "Experimental verification of the force coupling method for particulate flows," *International Journal of Multiphase Flow*, vol. 28, no. 2, pp. 225–246, 2002.

[241] J. Zhao, D. Lo Jacono, J. Sheridan, K. Hourigan, and M. C. Thompson, "Experimental investigation of in-line flow-induced vibration of a rotating circular cylinder," *Journal of Fluid Mechanics*, vol. 847, pp. 664–699, 2018.

[242] H. Ma and Y. Zhao, "An approach to distribute the marker points on non-spherical particle/boundary surface within the IBM-LBM framework," *Engineering Analysis with Boundary Elements*, vol. 108, pp. 254–266, 2019.